

GRAIN REFINEMENT OF Al-Si-Mg CAST ALLOYS WITH NIOBIUM –
BORON ADDITION

A THESIS SUBMITTED TO
THE GRADUATE SCHOOL OF NATURAL AND APPLIED SCIENCES
OF
MIDDLE EAST TECHNICAL UNIVERSITY

BY

ENVER BURAK ALDOĞAN

IN PARTIAL FULFILLMENT OF THE REQUIREMENTS
FOR
THE DEGREE OF MASTER OF SCIENCE
IN
METALLURGICAL AND MATERIALS ENGINEERING

FEBRUARY 2021

Approval of the thesis:

**GRAIN REFINEMENT OF Al-Si-Mg CAST ALLOYS WITH NIOBIUM –
BORON ADDITION**

submitted by **ENVER BURAK ALDOĞAN** in partial fulfillment of the requirements for the degree of **Master of Science in Metallurgical and Materials Engineering, Middle East Technical University** by,

Prof. Dr. Halil Kalıpçılar
Dean, Graduate School of **Natural and Applied Sciences** _____

Prof. Dr. C. Hakan Gür
Head of the Department, **Metallurgical and Materials Engineering** _____

Prof. Dr. Ali Kalkanlı
Supervisor, **Metallurgical and Materials Engineering, METU** _____

Examining Committee Members:

Prof. Dr. Bilgehan Ögel
Metallurgical and Materials Eng., METU _____

Prof. Dr. Ali Kalkanlı
Metallurgical and Materials Eng., METU _____

Prof. Dr. Arcan F. Dericioğlu
Metallurgical and Materials Eng., METU _____

Doç. Dr. Ayşe Kalemtaş
Metallurgical and Materials Eng., Bursa Teknik University _____

Prof. Dr. Özgül Keleş
Metallurgical and Materials Eng., Istanbul Technical University _____

Date: 15.02.2021

I hereby declare that all information in this document has been obtained and presented in accordance with academic rules and ethical conduct. I also declare that, as required by these rules and conduct, I have fully cited and referenced all material and results that are not original to this work.

Name, Last name : Enver Burak,

Aldođan

Signature :

ABSTRACT

GRAIN REFINEMENT OF Al-Si-Mg CAST ALLOYS WITH NIOBIUM – BORON ADDITION

Aldoğan, Enver Burak
Master of Science, Metallurgical and Materials Engineering
Supervisor: Prof. Dr. Ali Kalkanlı

February 2021, # 135

The aim of this thesis is to observe the grain refinement effect of aluminum (Al), niobium (Nb) and boron (B) alloy for silicon and magnesium-based aluminum cast alloys, especially A357. When the silicon content exceeds the 3 % w.t on the aluminum, silicon and magnesium-based alloy, effectiveness of Al-Ti-B grain refiner decreases due to formation of titanium silicide precipitates, called as poisoning effect. The surface of the grain refining constituents are coated with titanium silicide, and number of TiB_2 particles decrease. Since the lattice mismatch with aluminum matrix is higher for titanium silicide than Al_3Ti and TiB_2 , grain refinement efficiency decreases.

There are other studies to develop the grain refiners for aluminum cast alloys having silicon content higher than 3 %, which are the use of low content titanium instead of Al-5Ti-B, or Al-B in different boron amounts. However, since the commercial aluminum - silicon base alloys include titanium as an impurity, poisoning effect cannot be eliminated. That's why, recently niobium – boron-based grain refiners have been developed. The most important advantage is that niobium is much more stable at 750 - 800 °C than titanium which results in avoiding poisoning. In addition, having nearly same lattice parameters of Al_3Nb and NbB_2 with Al_3Ti and TiB_2 is also another advantage as a candidate for grain refiner.

In this thesis, Al_{2.79}Nb_{0.3}B alloy is experienced as a grain refiner for A357 alloy. The results show that eutectic structure is changed from acicular to fibrous and transitional lamellar structure. An increase in the amount of eutectic undercooling and decrease in eutectic temperatures supported the microstructural examinations. Moreover, it is observed that grain size is also decreased. However, its effect on grain size is seen as similar with commercially used Al₅TiB alloy. So, grain size was decreased by nearly the same amount.

Keywords: A357 alloy, Grain refinement, Sand casting, Niobium grain refinement, poisoning effect.

ÖZ

Al-Si-Mg DÖKÜM ALAŞIMLARININ NİYOPYUM – BORON ILAVESİ İLE TANE İNCELTİLMESİ

Aldoğan, Enver Burak
Yüksek Lisans, Metalurji ve Malzeme Mühendisliği
Tez Yöneticisi: Prof. Dr. Ali Kalkanlı

Şubat 2021, # 135

Bu tezin amacı, silis ve magnezyum içeren alüminyum döküm alaşımlarında, özellikle A357.0 alaşımı, alüminyum (Al), niyobyum (Nb) and boron (B) alaşımının tane inceltici etkisini gözlemlemektir. Alüminyum, silis ve magnezyum bazlı alaşımlarda, silis oranı ağırlık olarak %3'den fazla olduğu zaman, Al-Ti-B tane incelticisi titanyum silis bazlı çökelti oluşturduğu için etkisini yitirmeye başlar ve bu duruma zehirlenme etkisi denir. Tane inceltici etkiye sahip olan fazların yüzeyleri titanyum silis bazlı faz ile kaplanır ve TiB_2 parçacıklarının sayısı azalır. Titanyum – silis çökeltilerinin alüminyum matrisi ile kafes yapıları arasındaki fark Al_3Ti ve TiB_2 fazlarına göre daha fazla olduğu için tane inceltici etkisi azalır.

Silis oranı % 3'den fazla olan alüminyum döküm alaşımlarının tane inceltimi için başka çalışmalarda vardır. Bu çalışmalar, daha düşük titanyum ağırlık yüzdesine sahip Al-Ti-B alaşımı ve değişik boron oranlara sahip Al-B alaşımlarıdır. Ancak, ticari olarak kullanılan alüminyum ve silis bazlı döküm alaşımları titanyum elementini yabancı madde olarak içerdiği için, zehirlenme etkisi ortadan kalkmaz. Bu sebeplerden dolayı, niyobyum – boron alaşımları son zamanlarda geliştirilmeye başlanmıştır. Bu alaşımın en önemli avantajı 750 – 800 °C sıcaklıklarında titanyum bazlı alaşımdan daha kararlı olmasıdır. Buna ek olarak, Al_3Nb ve NbB_2 alaşımlarının

kafes yapıları Al_3Ti ve TiB_2 alaşımları ile çok yakın olması ise tane inceltici adayı olabilmesi için bir diğer avantajdır.

Bu tez çalışmasında $Al_{2.79}Nb_{0.3}B$ alaşımı, A357 alaşımı için tane inceltici olarak kullanılmıştır. Tez çalışmaları ötektik fazının morfolojik yapısının iğnemsî yapıdan fiber ve geçişli katmanlı yapıya dönüştüğünü göstermiştir. Ayrıca, ötektik dönüşümü sırasındaki yetersiz soğutmanın miktarındaki artış ve ötektik sıcaklıklarındaki düşük mikroyapı sonuçlarını desteklemiştir. Ek olarak, tane boyutunun azaldığı gözlemlenmiştir. Ancak, bunun etkisinin ticari olarak kullanılan Al_5TiB alaşımı ile neredeyse aynı olduğu görülmüştür. Diğer bir deyişle, tane boyutlarındaki düşüş neredeyse aynı olmuştur.

Anahtar Kelimeler: A357 alaşımı, Tane inceltici, Kuma döküm, Niyobyum tane incelticisi, zehirlenme etkisi.

To My Love,

Büşra

&

To My Mother,

Şahende

ACKNOWLEDGMENTS

Firstly and foremost, I would like to express my deep gratitude to my supervisor, Prof. Dr. Ali Kalkanlı for his continuous support, contribution and guidance since I became his student.

I am also grateful to the casting laboratory technicians, Ali Osman Atik and Salih Türe for their support through the experimental studies. I also have a great appreciation to my chief engineer, Emrah Yalınız for his teaching and guidance in both engineering and social life. I would like to express my special thanks for his endless contribution to my engineering carrier. I would also thank to Cemre Metin Poyraz for his great assistance in each step of experimental studies. During my absence in the university, he always supported to me. For scanning electron microscope analysis, I would like to thank again Cemre Metin Poyraz together with Orhan Berk Aytuna and Mustafa Anıl Yıldırım. Without Mustafa Anıl Yıldırım' assistance, high quality scanning electron microscope images could not be shared with the literature. Also, I would like to thank İbrahim Aydın for X-ray analysis and I would also thank to Sedat Ural for tensile testing.

I would like to express my great gratitude to my family for their endless love, and support through my master thesis period. And, I would like to thank my late father.

Finally, the greatest and deepest thanks go to my love, best friend and wife, Büşra. She always encouraged me to complete the master thesis. She always assisted to me in order to overcome difficulties which I faced with many times. I am very grateful to my love for her patience when I could not spend my time with her during my master thesis studies and for her endless love. Without her encouragement, this thesis could not be completed.

TABLE OF CONTENTS

ABSTRACT.....	v
ÖZ.....	vii
ACKNOWLEDGMENTS.....	x
TABLE OF CONTENTS.....	xi
LIST OF TABLES.....	xiv
LIST OF FIGURES.....	xv
LIST OF ABBREVIATIONS.....	xx
LIST OF SYMBOLS.....	xxi
CHAPTERS	
1 INTRODUCTION.....	1
2 LITERATURE REVIEW.....	5
2.1 Classification of Aluminum Alloys.....	5
2.1.1 Classification of Wrought Alloys.....	6
2.1.2 Classification of Cast Alloys.....	9
2.2 Effect of Alloying Elements on the Properties of Al-Si-Mg Alloys	10
2.2.1 Effect of Silicon.....	11
2.2.2 Effect of Iron.....	12
2.2.3 Effect of Magnesium.....	14
2.3 Solidification of Al-Si-Mg Alloys.....	15
2.4 Grain Refinement of Aluminum Cast Alloys.....	16
2.4.1 Nucleation Theory.....	16

2.4.2	Eutectic Modification	23
2.4.3	Grain Refinement and Fading	24
2.4.4	Al-Nb-B Based Grain Refiners	25
3	EXPERIMENTAL PROCEDURE	29
3.1	Raw Materials	29
3.1.1	A357.0 Base Material.....	29
3.1.2	Commercial Grain Refiner - AL5Ti1B	29
3.1.3	Commercial Grain Refiner – AL8B.....	30
3.1.4	Al2.79Nb0.3B Master Alloy	30
3.2	Mould Preparation.....	31
3.2.1	Resin Bonded Sand Mould.....	31
3.2.2	Permanent Mold	32
3.3	Casting Process	32
3.3.1	Master Alloy Casting Process	34
3.3.2	A357.0 Alloy Casting Process	36
3.4	Chemical Analysis	37
3.5	Thermal Analysis	38
3.6	XRD Measurement.....	42
3.7	Radiographic Inspection.....	43
3.8	Microstructural Examination	44
3.8.1	Metallographic Specimen Preparation	44
3.8.2	Optical Microscope Examination.....	46
3.8.3	Scanning Electron Microscope Examination	47
3.9	Heat Treatment.....	48

3.10	Mechanical Test.....	49
4	EXPERIMENTAL RESULTS AND DISCUSSIONS	51
4.1	Chemical Analysis	51
4.1.1	Chemical Analysis of Al-Nb Master Alloy	51
4.1.2	Chemical Analysis of Master Alloy.....	52
4.1.3	Chemical Analysis of Alloy I, II, III and IV.....	53
4.2	Determination of Liquidus, Eutectic Temperatures and Undercooling	54
4.3	XRD Measurements.....	61
4.4	Microstructural Analysis	64
4.4.1	Optical and Electron Microscope Examinations	64
4.4.2	Grain Size Measurements	104
4.5	Radiographic Examination Results	107
4.6	Mechanical Test Results.....	109
5	CONCLUSION AND FUTURE WORKS	115
	REFERENCES	117
A.	Cooling Curves and First and Second Derivatives.....	121
B.	Optical Microscope Images	125
C.	Grain Size Measurement Images	133

LIST OF TABLES

TABLES

Table 3.1 Chemical Composition in AMS 4219 Material Specification (wt. %)	29
Table 3.2 Chemical Composition of Commercial Al5Ti1B (wt. %)	30
Table 3.3 Chemical Composition of Al8B (wt. %)	30
Table 3.4 Amount of Raw Materials for Master Alloy Preparation	34
Table 3.5 Targeted Weight Percentages of Master Alloy	35
Table 3.6 Summary of intentionally cast alloys	36
Table 3.7 Amounts of Chemicals Inside the Etchants	44
Table 4.1 Chemical Composition of Al4Nb (wt. %)	51
Table 4.2 ICP-OES test results of Master Alloy	52
Table 4.3 XRF and ICP-OES chemical analysis results of Master Alloy	52
Table 4.4 Targeted chemical compositions of each alloy types (wt. %)	53
Table 4.5 Optical Emission Spectroscopy results of Alloy I, II, III and IV (wt. %)	54
Table 4.6 Critical Solidification Temperatures of Alloy I, II, III and IV (°C)	60
Table 4.7 Tensile Test Results of Alloy I, II, III and IV	111

LIST OF FIGURES

FIGURES

Figure 1.1 Overview of Motorsich Transmission [26]	2
Figure 1.2 AW169 Helicopter [27]	3
Figure 2.1 Classification of Aluminum Alloys [1]	6
Figure 2.2 Al-Si Phase Diagram [5].....	11
Figure 2.3 Large Flake Eutectic Phase [4].....	12
Figure 2.4 Different Fe rich precipitates; a: β platelets; b: script like α ; c: π phase growing from β ; d: script like π phase [7].....	14
Figure 2.5 Phase transformations during solidification of Al-Si-Mg alloys [7]	15
Figure 2.6 Hall Patch equation.....	16
Figure 2.7 Thermal diagram showing undercooling for pure metals [6].....	17
Figure 2.8 Schematic representation of nucleus [8].....	18
Figure 2.9 Free energy change curve for a homogeneous nucleation of a spherical particle.....	20
Figure 2.10 Example of heterogeneous nucleation nucleus formation [8]	22
Figure 2.11 Eutectic structure morphologies. (1: Acicular; 2: Lamellar; 3: Transitional Lamellar; 4: Mostly modified structure) [24].....	23
Figure 2.12 Lattice Parameters Comparison of Aluminum, Titanium and Niobium [20].....	26
Figure 2.13 Growth Restriction Factor of Potential Grain Refiner Elements [16].	27
Figure 3.1 Al4Nb Master Alloy Blocks	31
Figure 3.2 Tensile Specimen Mould.....	31
Figure 3.3 Permanent Moulds used for Master Alloys	32
Figure 3.4 Ajax Magnethermic Induction Furnace.....	33
Figure 3.5 Induction Furnace “Prothoterm”	34
Figure 3.6 Master Alloy	35
Figure 3.7 WAS Foundry Master optical emission spectroscopy [10].....	37
Figure 3.8 Chemical Analysis Specimens of Alloy I, II, III and IV	38

Figure 3.9 K type cable thermocouple [10].....	39
Figure 3.10 K type metal thermocouple [10]	39
Figure 3.11 Ordel data logger temperature scanner connected to the computer [10]	40
Figure 3.12 Primary and first derivative cooling curves of the same thermal analysis experiment	41
Figure 3.13 Thermocouple location in the Quick cap	41
Figure 3.14 XRD chart obtained for master alloy produced [12].....	42
Figure 3.15 XRD instrument used for crystal structure analysis [10].....	43
Figure 3.16 Example of digital x-ray inspection results of Alloy II	43
Figure 3.17 Example of specimen extractions; a: Specimens as extracted from the mould, b: Cut into smaller sections, c: Mounting specimen extraction, d: Mounting specimen extraction	45
Figure 3.18 METACUT 251 grinding cutter (right) and the mounting bakelite device (left) [10].....	45
Figure 3.19 Rotating disc type a: Grinder, b: Polisher with 6 μ and 1 μ diamond solutions [10].....	46
Figure 3.20 Optical Microscopes; a: Huvitz optical microscope, b: SOIF XJP-6A optical microscope.....	47
Figure 3.21 NOVA NANO SEM 430 Scanning electron microscope setup.....	48
Figure 3.22 Electrical resistance furnace used for heat treatments	49
Figure 4.1 Cooling Curves of Alloy I, II, I II and IV	55
Figure 4.2 Temperature vs. time and first derivative curves	56
Figure 4.3 Second derivation of temperature vs. time graph	57
Figure 4.4 Primary alpha nucleation and growth zone of Alloy I, II, III and IV	57
Figure 4.5 Al-Si eutectic nucleation and growth zone of Alloy I, II, III and IV.....	59
Figure 4.6 Solidus temperature zone of Alloy I, II, III and IV.....	59
Figure 4.7 XRD Peaks of Alloy I, II, III and IV As-Cast Alloys.....	61
Figure 4.8 XRD Peaks of Alloy I, II, III and IV As-Heat Treated Alloys	62
Figure 4.9 XRD Peaks of Master Alloy	63

Figure 4.10 Optical Microstructure Images of Alloy I etched with Keller’s reagent (a:50x magnification; b:200x magnification)	65
Figure 4.11 Scanning electron microscope results of Alloy I.....	66
Figure 4.12 Optical microscope images of acicular eutectic morphology of Alloy I etched with Keller’s reagent (a: 200x magnification b: zoomed vie).....	67
Figure 4.13 Optical microscope images of transition lamellar/fibrous eutectic morphology after heat treatment of Alloy I etched with Keller’s reagent (a & b: 200x magnification; c: 500x magnification; d:1000x magnification)	70
Figure 4.14 Transition Lamellar/Fibrous eutectic morphology of as-cast Alloy III etched with Tucker’s reagent (a: 200x magnification; b: 500x magnification).....	71
Figure 4.15 Optical microscopes images of Alloy III after heat treatment etched with Keller’s reagent (a: Fine fibrous eutectics with 500x magnification; b: Large silicon and lamellar eutectics with 500x magnification)	72
Figure 4.16 Optical microscope images of Alloy III in as-cast and as-heat-treated conditions (a and c:200x and 500x, respectively, magnifications of as-cast Alloy III; b and d: 200x and 500x, respectively, magnifications of heat-treated Alloy III)	75
Figure 4.17 Scanning electron microscope images of as-cast Alloy III	77
Figure 4.18 Energy Dispersive Spectroscopy examination of as-cast Alloy III (a: SEM images of general area; b: EDS analysis results of general area; c: Mg ₂ Si included general area; d: Point EDS analysis of Mg ₂ Si)	79
Figure 4.19 Energy Dispersive Spectroscopy and High Density Back Scattered examination of as-cast Alloy III (a: SEM images for iron-contained eutectic Si; b: Point analysis of the phase iron-contained eutectic phase; c: High Density Back Scattered Images of iron contained eutectic phase.	81
Figure 4.20 Scanning electron microscope images of heat-treated Alloy III	82
Figure 4.21 Optical microscope images with 500x magnification of acicular/lamellar eutectic morphology of as-cast Alloy IV etched with Tucker’s reagent. (a: 500x magnification; b: Zoomed in acicular eutectic structure)	83

Figure 4.22 Optical microscope images for π phase. (a: 1000x magnification of heat-treated Alloy IV; b: script like π phase [7]).....	84
Figure 4.23 Optical microscope images. (a: As-Cast Alloy IV 200x magnification: Heat Treated Alloy IV 200x magnification)	85
Figure 4.24 Optical microscope images of as-cast Alloy II. (a: 500x magnification; b:1000x magnification)	86
Figure 4.25 Optical microscope images of heat-treated Alloy II. (a:200X; b:500X; c:1000X magnifications)	88
Figure 4.26 Optical microscope images of as-cast alloys at 200X magnification etched by Keller’s reagent. (a: Alloy I; b: Alloy II; c: Alloy III; d: Alloy IV magnifications).....	91
Figure 4.27 Optical microscope images of as-cast Alloy II for different cross-sections. (a:9 mm thickness – 200X magnification; b:9 mm thickness – 500X magnification; c:12 mm thickness – 200X magnification; d:12 mm thickness – 500X magnification; e:20 mm thickness – 200X magnification; f:20 mm thickness – 500X magnification; g:40 mm thickness – 200X magnification)	95
Figure 4.28 Optical microscope images of as-cast Alloy II having 40 mm cross section, 200X magnification.....	96
Figure 4.29 Scanning Electron Microscope images of as-cast Alloy II. (a:SEM images;b:EDS analysis of localized white precipitate)	97
Figure 4.30 Scanning Electron Microscope images of as-cast Alloy II.....	98
Figure 4.31 Scanning Electron Microscope images of as-cast Alloy II. (a SEM images; b: EDS analysis of selected area).....	99
Figure 4.32 Scanning Electron Microscope images of heat-treated Alloy II in different magnifications. (a:214X magnifications; b: 88X magnification; c:179X magnification; d:826X magnification)	101
Figure 4.33 Scanning Electron Microscope images of master alloy. (a:100X magnification; b:374X magnification; c:EDS analysis results)	103
Figure 4.34 Example of grain size measurement, a: Alloy II, b: Alloy III	105
Figure 4.35 Comparison of grain size of Alloy I, II, III and IV	106

Figure 4.36 Comparison of grain sizes measured in different cross sections of Alloy II.....	107
Figure 4.37 Radiographic examination results of Alloy I,II,III, and IV	108
Figure 4.38 Radiographic examination results of Alloy II	108
Figure 4.39 Tensile test results comparison for Alloy I, II, III and IV	109
Figure 4.40 Comparison of yield strength and grain size for Alloy I, II, III and IV	112
Figure 4.41 Comparison of tensile test values of Alloy II specimens	113

LIST OF ABBREVIATIONS

ABBREVIATIONS

ICP – OES	Inductively Coupled Plasma – Optical Emission Spectroscopy
AMS	Aerospace Material Specification
g	Gram
h	Hour
min	Minutes
XRF	X-Ray Fluorescence
OES	Optical Emission Spectroscopy
XRD	X-Ray Diffraction
kV	Kilovolt
SEM	Scanning Electron Microscope
EDS	Energy Dispersive Spectroscopy
Q	Growth Restriction Factor
Wt.%	Weight Percentage
T	Temperature
T _m	Melting Temperature
T _s	Solidus Temperature
T _n	Nucleation Temperature
T _g	Growth Temperature

LIST OF SYMBOLS

SYMBOLS

d	Average Grain Size
L_v	Latent Heat of Fusion per Unit Volume
ΔS	Change in Entropy
ΔH	Change in Enthalpy
ΔG_v	Net Bulk Free Energy

Elements

Al	Aluminum
Ag	Silver
B	Boron
Be	Beryllium
C	Carbon
Cr	Chromium
Co	Cobalt
Cu	Copper
Fe	Iron
Li	Lithium
Mg	Magnesium
Mn	Manganese
Nb	Niobium

Na	Sodium
Ni	Nickel
O	Oxygen
P	Phosphorus
Si	Silicon
Sn	Tin
Sr	Strontium
Ti	Titanium
Zn	Zinc

CHAPTER 1

INTRODUCTION

Aluminum alloys are widely used in industry. They possess broad range of field, from food industry to aerospace since they are versatile and economical. They can be manufactured for wrapping foil application requiring high ductility while they can be used for airframe of aircraft due to their higher specific strength, which means the having high strength to density ratio. High strength to density ratio makes aluminum alloys favorable in aerospace industry due to weight reduction consideration. Their usage is not only limited with airframe but also used in dynamic systems like gearboxes. Figure 1.1 is an example of Russian Mi-17 helicopter transmission system. As it is seen, casings are very difficult to machine out. That's why, casting is generally preferred as a manufacturing method. Also, Figure 1.2 indicates the AW169 helicopter, which is designed including highest technology. And, aluminum casting alloys, especially A357, is the most important candidate for material selection. In automotive industry, iron alloys can be designed but lightweight alloys are the only metals considered as candidate material for aerospace. Due to lack of corrosion resistance of magnesium alloys, aluminum alloys are widely used in gearbox casings. Engineers deals with alloying of magnesium alloys to enhance corrosion resistance and mechanical properties. However, manufacturing cost becomes higher when compared with aluminum alloys because casting of magnesium requires special protection methods, getting more cost. For the complex parts including helicopter gearboxes, sand casting is generally preferred due to allowance of variety in thickness.

Also, in order to increase the casting properties like feeding, silicon is a common element preferred for aluminum alloys. That's why, engineers use aluminum alloys

including silicon for castability. The most commonly used material is A357 alloy including aluminum, silicon and magnesium elements. Since it includes beryllium, percent elongation is a little bit higher than A356 alloy.



Figure 1.1 Overview of Motorsich Transmission [26]

Al₅Ti₃B is generally used for the grain refinement purpose. Also, aluminum strontium alloy is another alloying element to modify eutectic structure. However, eutectic modification causes some adverse effects on the casting properties like increase in porosity percentage. Recently, engineers research another grain refiner due to poisoning of Al-Si-Mg alloys. Since titanium element reacts with the silicon if the amount is higher than 3 wt.%, their effectiveness decreases. Formation of titanium silicide is coated to the surface of the Ti₂B nucleating agent, their effectiveness is decreased. They tried to replace with Al₃Ti₃B, Al₃B in order to decrease the titanium element inside. However, since commercially used aluminum alloys generally includes titanium as an impurity, formation of silicide cannot be avoided when the silicon concentration is greater than 3 wt.%. Recently, niobium alloy is found a candidate element when alloying with boron. Since their lattice

parameters are very similar with titanium, performed researches show that they decrease the grain size. There are limited researches about grain refinement of recently found alloy. Researches show that there is no certainly verified master alloy including Al-Nb-B. Variety of Nb and B contents are examined in order to observe the grain refinement properties. According to the researches, there shall be an optimum amount of Al_3Nb and NbB_2 in the master alloy. That's why, stoichiometry is an important parameter.



Figure 1.2 AW169 Helicopter [27]

CHAPTER 2

LITERATURE REVIEW

2.1 Classification of Aluminum Alloys

Aluminum is one of the most abundant material found as oxide in earthquake. Aluminum oxide forms nearly 7 % of earthquake materials. This makes aluminum cheaper and primary choice when necessary physical and mechanical requirements are fulfilled by correct manufacturing processes. Aluminum has a density of 2.7 g/cm³. It is the one third of the steel. When aluminum is used with alloying elements, its strength can meet the requirements for structural applications. Apart from its lightweight, it is very conductive. That's why, it is preferable when conductivity requirements are needed. However, it is highly reactant with oxygen, it readily oxides with air. Its appearance is colorless. A thin oxide layer avoids further oxidation. When oxide layer is damaged, it will instantly reappear. Alloying elements are used to enhance corrosion resistance for water, salt and other environments.

Aluminum alloys can be divided as 2 main categories, wrought alloys and cast alloys, according to their manufacturing methodology. 2 main group are classified according to their alloying elements and each series of alloy are called by specific names given by Aluminum Association. Apart from the manufacturing methodology classification, they can be divided as heat treatable and non- heat treatable. Heat treatment provides to enhance the mechanical properties of aluminum alloys. Solution treatment, quenching, precipitation hardening and aging are the heat treatment types. For non-heat treatable alloys, work hardening is performed to use the aluminum alloys in structural applications requiring higher mechanical properties. Following sections, aluminum alloys classifications are explained.

All the manufacturing process begin with minerals found in nature. Primary used mineral for aluminum manufacturing is bauxite. Bauxite includes 45 – 60 % aluminum oxide (alumina) which is the primary source for pure aluminum manufacturing. However, impurities are also found in bauxite like sand, iron and other metallic materials. Therefore, refining process called as Bayer process is performed before metallic aluminum manufacturing so aluminum oxide is separated from other impurities. Then, aluminum oxide is smelted in order to obtain metallic aluminum. Electric current is applied in smelting process with the help of carbon electrode rods and almost pure aluminum (99.8%) is obtained as a product. Then, it is transferred to holding furnace and cast into molds. Alloying additions are accomplished according to the type of the alloy. Afterwards, ingots are cut into desired lengths. Ingots are used for wrought and cast alloys [1].

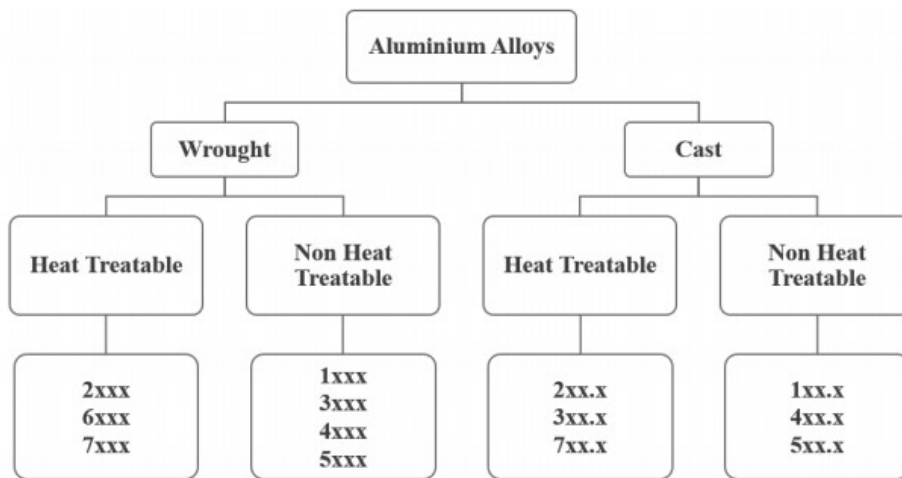


Figure 2.1 Classification of Aluminum Alloys [1]

2.1.1 Classification of Wrought Alloys

Ingots which are pure or alloyed with other elements are subsequently mechanically formed. Hot and cold rolling, extrusion, drawing, seamless deep drawing are the types of mechanical operations. They are selected according to the desired cross

section. As a result of the forming process, sheet, plate, foil, rod and bar etc. products are manufactured. According to the alloy type, products can be heat treated to enhance the mechanical properties of the part [2].

The designation of the wrought aluminum alloys is shown as follows [2];

1xxx: They include at least 99 wt. % of aluminum. They are used especially in electrical and chemical fields. They possess excellent corrosion resistance, high thermal and electrical conductivity and excellent workability but they have low mechanical properties. Iron and silicon are the major impurities.

2xxx: Copper is the primary alloying element, often magnesium alloys are found as a secondary major element. Their corrosion resistance is lower when compared with most of the aluminum alloys. They exhibit poor intergranular corrosion resistance under certain conditions. Therefore, their sheet forms are generally clad with high purity aluminum. They have high mechanical properties. They are commonly used in structural components like automotive, aircraft fuselage, truck suspension.

3xxx: Manganese is the primary used alloying element. They can be strengthened 20 % more than 1xxx alloys. Their general purpose is to be used in moderate strength required application together with good workability

4xxx: The major alloying element is silicon. They can be added in sufficient quantities (up to 12 wt. %). It provides to lower the melting range without causing any brittleness. Because they have lower melting point, they are used in welding application to join aluminum alloys together. They have low coefficient of thermal expansion and high wear resistance.

5xxx: The principal alloying element is magnesium. In some cases, they can also be alloyed with manganese in order to provide moderate to high strength mechanical properties. Magnesium is considerably more effective than manganese for enhancing the mechanical properties. They have good welding resistance and corrosion resistance in marine atmosphere.

6xxx: Primary alloying elements are silicon and magnesium. Their mechanical properties are lower than the alloys 2xxx and 7xxx. They have good formability, weldability, machinability, and corrosion resistance.

7xxx: Major alloying element is zinc in amounts of 1 to 8 wt. %. They can also couple with magnesium alloys in some cases. They have moderate to high strength. They are used in highly stressed parts, e.g. airframe structures. As the strength of the material increases, resistance to stress corrosion decreases. That's why, most of the alloy are used in overaged condition.

8xxx: This alloy type covers wide range of chemical composition. Al-Fe-Ce (e.g. 8019) or Al-Fe-V-Si (e.g. 8009) are the examples of 8xxx alloys. They have different microstructure providing different application areas. Also, lithium elements are included in 8xxx alloy type. Lithium containing aluminum alloys (e.g. 8090) have higher specific strength and stiffness which makes them useful for aerospace applications.

Above, all the wrought alloys classifications are summarized according to their chemical compositions. Chemical composition results difference in microstructure, e.g. type of second phases. The formation of the second phases is related with heat treatment. Some of the alloy types response the heat treatment by forming precipitations. These alloys are called as heat- treatable while others which do not response are not-heat treatable alloys. Among aluminum wrought alloys, 2xxx, 6xxx, 7xxx and some of the 8xxx alloys are heat treatable while others are classified as non- heat treatable. Heat treatable alloys gain their mechanical properties by heat treatment while others which do not response heat treatment enhance mechanical properties by strain hardening.

2.1.2 Classification of Cast Alloys

Casting alloys are also classified according to their chemistry. They are strengthened by the same mechanism except strain hardening. The most important difference is that silicon amount is higher than wrought alloys. It changes 4 to 12 wt. % (eutectic point). Silicon increases the fluidity so more intricate shape, thin wall components can be cast with higher surface roughness and lower defects inside. Below, classification of cast alloys are explained [2];

2xx.x: The primary alloying element is copper. The amount of copper is in the range of 4 to 6 wt. %. Also, magnesium can exist in some instances. Apart from the magnesium, Mn, Cr and Ag can be included. These series have the highest strength and hardness among all casting alloys at elevated temperatures. However, general corrosion resistance is lower than other series so surface protection is required.

3xx.x: This series of alloys constitutes the highest volume usage among other cast series. They have primarily included silicon. Additionally, copper, magnesium or both of them can be found in specific cases. Generally, they fall into three groups, Al-Si-Mg, Al-Si-Cu or Al-Si-Cu-Mg. Amount of silicon and copper varies between 5 to 22 wt. %, and 0 to 4.5 wt. %, respectively. Magnesium content changes between 0.3 and 0.6 wt. % for the high strength applications, but up to 1 wt. % can be found for piston applications. On the other hand, magnesium content is required maximum 0.1 wt. % for die casting applications.

Copper and magnesium increase the strength and hardness during solution heat treatment. That's why, alloys including copper and magnesium together possess highest strength at elevated temperature.

Higher silicon content provides the alloy to have lower thermal expansion coefficient. That's why, they are preferred in engine applications. When the silicon content exceed the eutectic point and they are distributed fine and well so wear resistance is increased.

4xx.x: Only alloying element is silicon. Silicon content varies between 5 to 12 wt. %. They are used when moderate strength, high ductility and impact resistance are required.

5xx.x: Only alloying element is magnesium. They are used when moderate strength and toughness are required. They have high corrosion resistance in seawater and marine atmosphere. They are used in architectural and other decorative or building application since when they are anodized to get attractive appearance. These group of alloys also have good machinability.

7xx.x: Primary alloying elements are zinc and magnesium. Their corrosion resistance is good and they have good finishing characteristics. They are preferred due to their finishing characteristic and corrosion resistance.

8xx.x: Primary alloying element is Sn. They constitute of nearly 6 wt. % of Sn and also small amount of nickel and copper to improve their strength. They are generally used for bearing applications, e.g. crankcase bearing for diesel engines.

2.2 Effect of Alloying Elements on the Properties of Al-Si-Mg Alloys

Al-Si-Mg alloys are widely used in automotive and aerospace industry due to their excellent castability, good corrosion resistance and higher specific strengths. The lower silicon density having 2.3 g/cm^3 makes Al-Si-Mg alloys lighter than other alloys. They are commonly used in automotive airframe structure instead of heavier alloys in order to reduce fuel consumption and CO_2 emission. Addition of silicon to aluminum increases the fluidity so low shrinkage and hot cracking defects are expected. They gain improved mechanical properties by achieving heat treatment. Magnesium is added in the amount of 0.3 to 0.7 wt. % in order to form intermetallic with silicon. Mg_2Si precipitates are formed in aluminum matrix so yield strength is increased. Other than Mg_2Si compounds, iron-based impurities which are deleterious can be precipitated like α (Fe_2SiAl_8), β (FeSiAl_5) and π ($\text{FeMg}_3\text{Si}_6\text{Al}_8$). However, excess of magnesium is not desired in the alloy since it forms brittle precipitates with

iron. That's why, iron containing Al-Si-Mg alloys are limited in terms of magnesium concentration.

2.2.1 Effect of Silicon

Silicon is one of the least expensive material in all over the world. That's why its usage in alloy makes it preferable. Apart from its economic advantage, it increases castability, specific strength, corrosion resistance while decreases the thermal expansion coefficient. Because the silicon having strongest atomic band forces, it increases the wear resistance of the alloy [3].

Aluminum and silicon forms invariant eutectic reaction and nearly at 577 °C which are shown in Figure 2.2. During solidification, primary aluminum dendrites start to form and then eutectic transformation happens. Microstructural analyses reveal that primary aluminum dendrites and eutectic silicon particles are formed. Figure 2.3 shows that large flake like eutectic silicon particles in the as-cast condition for the alloy having low iron content in the Al – Si alloy [4]. This large flake structure is detrimental for mechanical properties. It causes sudden fracture. Modification with Na, Sr, Be are performed in order to obtain fine dispersed eutectic phases.

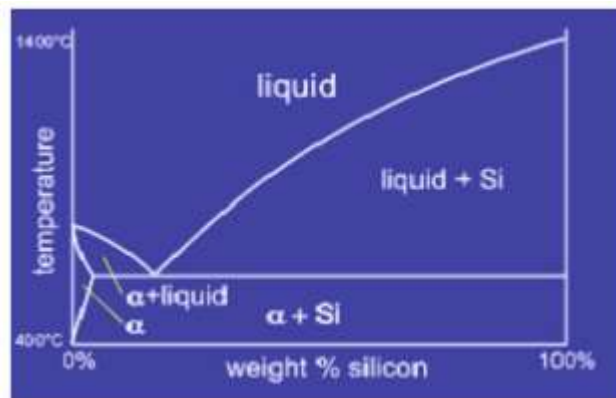


Figure 2.2 Al-Si Phase Diagram [5]

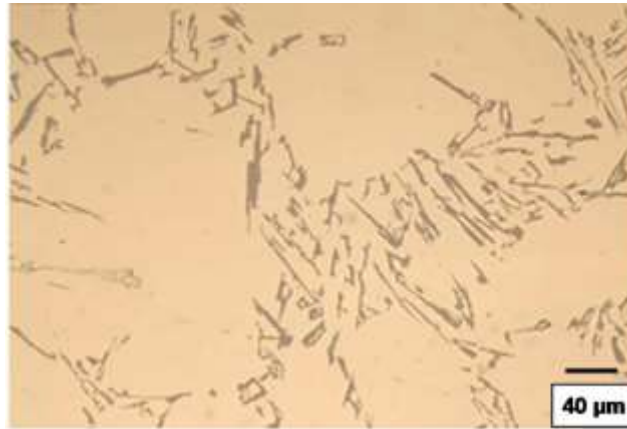


Figure 2.3 Large Flake Eutectic Phase [4]

2.2.2 Effect of Iron

Iron may come from different sources. Most of the iron comes from the primary aluminum making (Bayer Process) [7]. States that Fe including 0.03 – 0.15 % wt. comes from during primary aluminum making process. Other sources are the tools and furnace equipment used during subsequent casting process. Casting parameters like holding temperature and time affect the amount of iron in aluminum due to the contact time between the ferrous tooling and aluminum melt. At the end of the secondary casting process, iron levels in melt reach up to 0.25- 0.08 wt. % according to the [7]. Also, each re-melt cycle is detrimental due to the exposure to the unprotected ferrous tools and equipment. Also, impure alloying elements can be the source of iron in aluminum. Iron is highly soluble in the melt aluminum but solubility is very limited in the solid state. That's why, they tend to form intermetallic precipitates together with other alloying elements and aluminum. These intermetallic precipitates are detrimental for sand casting process although it is required in high pressure die casting applications to avoid die soldering. However, weight percentage, size, shape and chemical composition of intermetallic phases shall be controlled for sand casting, which can be adjusted to the chemical compositions of the raw materials. As the amount of iron in aluminum melt decreases, cost of the processing is increased, while mechanical properties is improved.

When the silicon presents in the melt, dominant phases are α (Fe_2SiAl_8) and β (FeSiAl_5). Also, when Mn exists in addition to the Si, $\text{Al}_{15}(\text{Fe},\text{Mn})_3\text{Si}_2$ can be formed. This phase is bafflingly known as α phase. They can be distinguished with optical microscope. They have different shape and color. During microstructural examination both α phase form in script like morphology. However, Mn included phase can be seen in more block form and be more compacted according to the [7]. β phase has platelet morphology in three dimensions but it can be observed as needle in two dimensions. When Mg is present with Si, π ($\text{FeMg}_3\text{Si}_6\text{Al}_8$) phase can form. Their morphology is script like morphology and they are generally, not always, closely connected with β phase [7]. Figure 2.4 shows the differences in morphology of iron rich intermetallic phases. The morphology is very important since mechanical properties and castabilities are affected [7].

Apart from the chemical concentration of the melt, cooling rate is another important factor for the formation of intermetallic phases. As the cooling rate decreases and number of iron atoms in the melt increases, larger particles are favored for the formation, and time for growth of intermetallic phases increases resulting larger particle formation. In addition to the cooling rate, as the Fe and Mn concentration increases, larger β platelets and α script like phases are seen in the microstructure since nucleation temperature increases which provide more unconstrained growth.

Taylor, John (2004) states that ductility is decreased due to micro-crack initiations resulted from iron intermetallic and fracture through them, and amount of porosity increases as iron content increases, which are the crack initiation sites. It is stated that β phase is more detrimental than α phase. That's why, neutralization with other chemical elements like Mn, Cr, Ni, Co, Be, etc. are studied in order to decrease the amount of β phase.

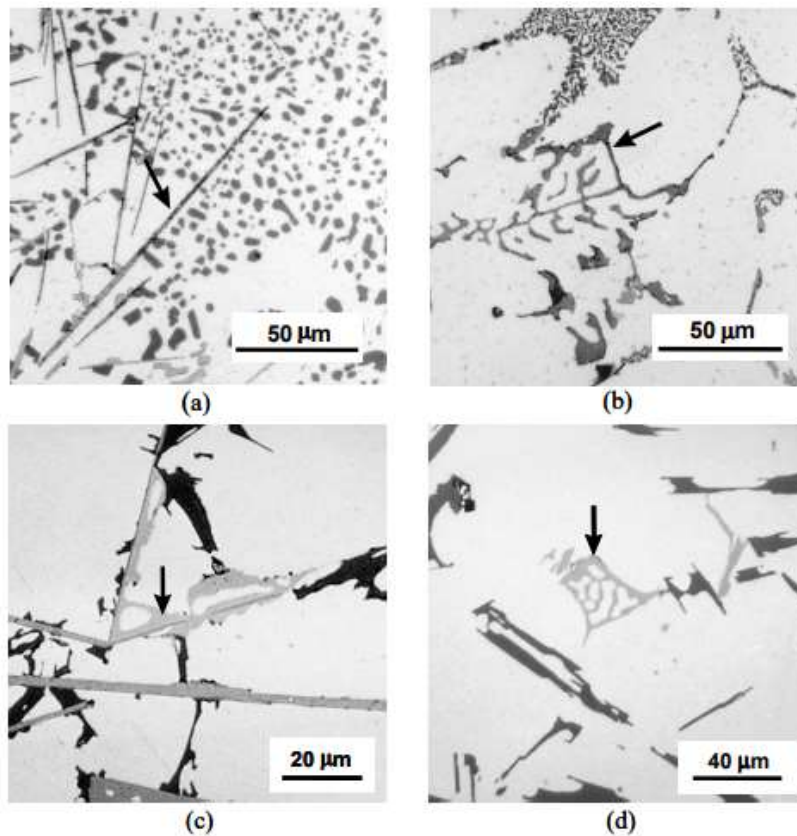


Figure 2.4 Different Fe rich precipitates; a: β platelets; b: script like α ; c: π phase growing from β ; d: script like π phase [7]

Furthermore, iron has effect on castability. There are lots of studies performed in order for clarification. Some of the ideas are that iron increases the porosity level due to large β precipitates. They avoid inter - dendritic feeding and resulting porosity formation. Also, iron causes the poisoning of eutectic cells nucleation sites and results formation of large eutectic cells. Therefore, shrinkage porosity increases since both large β platelets and eutectic cells avoids inter - dendritic feeding.

2.2.3 Effect of Magnesium

Magnesium increases the yield strength of the Al-Si alloy by heat treatment. Solutioning and aging treatments provide the formation of Mg_2Si particles. As the magnesium amount increases, yield strength increases. However, excess of the

magnesium results in the formation of detrimental iron rich intermetallic like π phase ($\text{FeMg}_3\text{Si}_5\text{Al}_9$). Its effect is also more pronounced when eutectic modification element, Sr, is used. Lloyd and Samuel J., (2016) states that yield strength is increased as Mg content increases. However, there is seen slight decrement in ductility. Nevertheless, it states that effect of Mg on ductility is more pronounced effect modified alloys due to the formation of large π phases.

2.3 Solidification of Al-Si-Mg Alloys

As indicated in Figure 2.2, aluminum has no solubility in silicon so only pure silicon is seen instead of β phase. In aluminum – silicon alloys, firstly nucleation and growth of primary aluminum dendrites are seen in between liquids and eutectic temperature, called as mushy zone.

Then, eutectic phase transformation occurs in which eutectic Al-Si phases nucleates and grows, then β phase nucleates together with Al-Si eutectic. Then, β phase partly transforms to the π phase. Finally, Mg_2Si precipitates nucleate with Al-Si eutectic and π phase [7].

Reaction No. defined in [6]	Reaction	Suggested start Temperature ($^{\circ}\text{C}$) [6].	Tentative assignment to DSC peak
1	Liq. \rightarrow Al dendrites	611–615	1
2	Liq. \rightarrow Al + Si	577	2
3a	Liq. \rightarrow Al + Si + Al_5FeSi	575	—
3b	Liq. + $\text{Al}_5\text{FeSi} \rightarrow$ Al + Si + $\text{Al}_8\text{FeMg}_3\text{Si}_6$	567	—
4	Liq. \rightarrow Al + Si + Mg_2Si	555	3a
5	Liq. \rightarrow Al + Si + Mg_2Si + $\text{Al}_8\text{FeMg}_3\text{Si}_6$	550–554	3b

Figure 2.5 Phase transformations during solidification of Al-Si-Mg alloys [7]

2.4 Grain Refinement of Aluminum Cast Alloys

Grain refinement is a well-known practice applied for most of the Al cast alloys. It has significant effect on mechanical properties. The reason of the improvement in mechanical properties can be listed as follows [21];

- Homogeneous distribution of second phases,
- Homogeneous and small size of porosity formation,
- Increasing feeding properties,
- Decrease in surface defects

Especially, apart from the advantages listed above, decrease in grain size has a major effect for yield strength increment. It is strongly explained by Hall Patch equation [6]. The formula is expressed in Figure 2.6.

$$\sigma_y = \sigma_0 + \frac{k_y}{\sqrt{d}}$$

Figure 2.6 Hall Patch equation

The mechanism under the grain refinement are based on nucleation and growth phenomena. They are explained in the following chapters.

2.4.1 Nucleation Theory

During solidification of a liquid alloy, there is a temperature in which the nuclei particles form and grow. Nuclei particles include solid atoms created during the solidification. Number of nuclei are called as nucleus. Growth of nucleus provides the formation of grains. The number of grains is directly related with number of nucleus. In order for growth mechanism, size of primarily formed nucleus is an

important parameter. There are two type of nucleation mechanism, homogenous and heterogeneous nucleation.

2.4.1.1 Homogeneous Nucleation

Homogeneous nucleation happens in the absence of any irregularities or other sources acting as a nucleation site. Nuclei formation starts at a temperature, T , below equilibrium melting temperature, T_m . This is explained by a phenomenon, undercooling. Undercooling is a driving force for the nucleation. Some extent of undercooling must be present for nucleation. Figure 2.7 explains the meaning of under cooling in a diagrammatic way.

Undercooling (or) Supercooling in pure metals

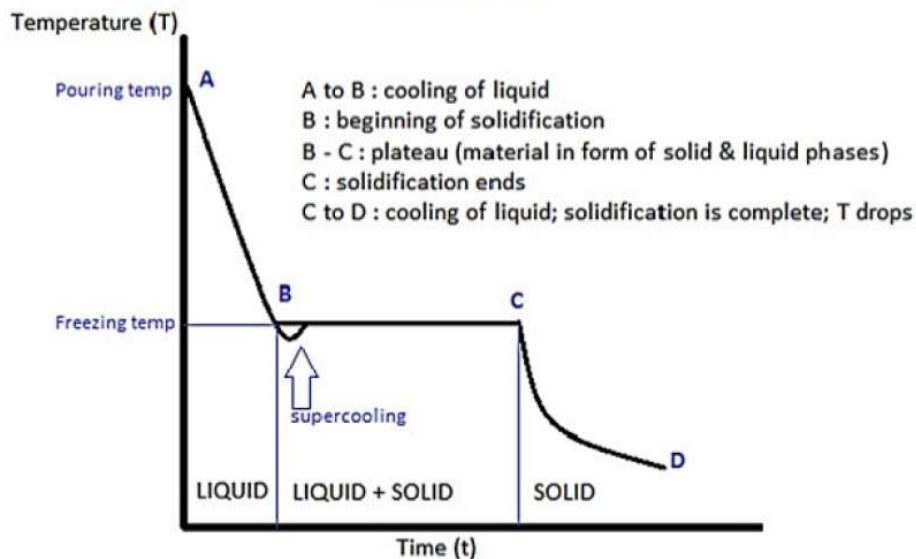


Figure 2.7 Thermal diagram showing undercooling for pure metals [6].

For homogeneous nucleation, the amount of undercooling is very high, which is not possible in most of the engineering practices.

During the solidification, shape of the nucleus is assumed as spherical as indicated in Figure 2.8.

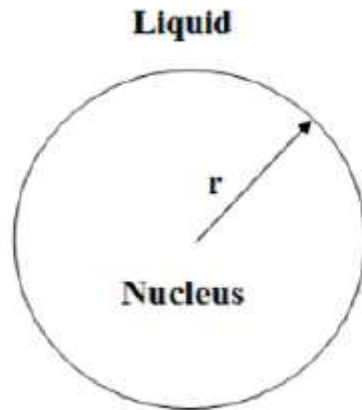


Figure 2.8 Schematic representation of nucleus [8]

Nucleation requires free energy change. In order for nucleus formation, some extent of free energy change shall be present. The energy needed for phase transformation is called as ΔG_v , net free energy necessary for phase transformation from liquid to solid, and γ_{sl} , the interfacial tension between solid and liquid interface [8].

$$\Delta G_v = \Delta H - T\Delta S \quad (2-1)$$

Where,

ΔH : The change in enthalpy= Latent heat of fusion per unit volume, L_v

ΔS : The change in entropy = $\frac{L_v}{T_m}$

T_m : Melting point of liquid

Equation (2-1) can be written as follows;

$$\Delta G_v = L_v - T \frac{L_v}{T_m} \quad (2-2)$$

Transformation of liquid to solid can be spontaneously occurred when equation (2-2) is smaller than zero. Formation of nucleus is seen in the case of $T < T_m$.

In addition, when the total volume of sphere is considered, net free energy necessary for entire sphere is;

$$\Delta G = \Delta T \frac{Lv}{Tm} * \frac{4}{3} \pi r^3 \quad (2-3)$$

Where,

r: Radius of the sphere (See Figure 2.8)

$$\Delta T = \frac{Tm - T}{Tm} \quad (2-4)$$

The net free energy per volume with a given undercooling, equation (2-4), can be written as follows;

$$\Delta Gv = \Delta T \frac{Lv}{Tm} \quad (2-5)$$

Equation (2-5) is the energy required for the nucleus formation. However, it has also another term, surface energy (ΔG_s), expressed in equation (2-6). It is positive sign. It is the energy for the creation of new surface during nucleus formation.

$$\Delta G_s = 4\pi r^2 * \gamma_{sl} \quad (2-6)$$

When the both surface energy term and net free energy term per volume are considered, total energy required for the formation of spherical particle can be expressed as equation (2-7).

$$\Delta Gr = -\Delta Gv * \frac{4}{3} \pi r^3 + 4\pi r^2 * \gamma_{sl} \quad (2-7)$$

During nucleation theory, there is an important parameter expressed as r^* which is called critical nucleus radius. Some of the atoms start to solidify near to the T_m when required undercooling is fulfilled. However, the change in the total free energy for a

sphere, must be negative in sign in order that nucleus formation and growth can be initiated. Figure 2.9 explains the total free energy terms including total free energy per volume and surface energy. At the beginning of nucleus formation, the total free energy is positive since the formation of created new surfaces is greater than that of the free energy per volume term. That is, surface energy related term dominates the equation up to the $r < r^*$, r^* is the critical radius for the sphere particle formation. That's why, formation of a nucleus is thermodynamically impossible due to non-spontaneous reaction. Solidifying atoms dissolve in the melt. Nevertheless, the change in total free energy becomes negative, which is thermodynamically stable reaction together with formation of a newly solid atoms, that is r is greater than r^* . At this stage, free energy per volume term dominates the total free energy equation.

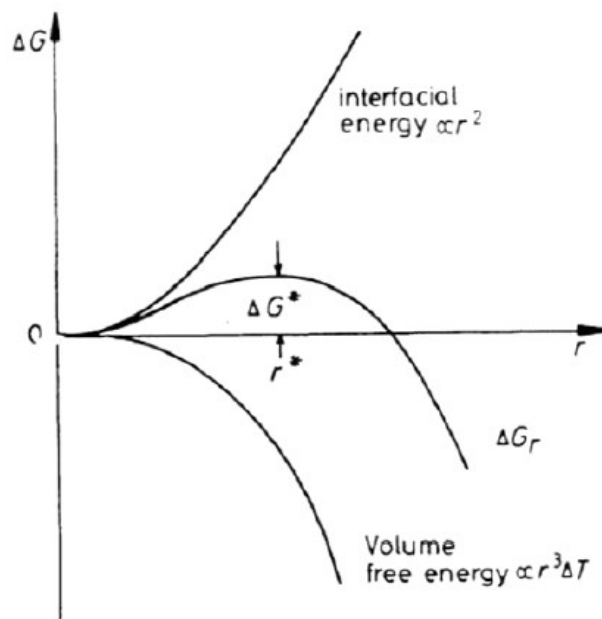


Figure 2.9 Free energy change curve for a homogeneous nucleation of a spherical particle.

Critical radius can be calculated by taking the slope at the energy is equal to the maximum energy shown in Figure 2.9.

$$r^* = \frac{2\gamma_{sl}}{\Delta G_v} \quad (2-8)$$

By substituting the equation (2-5 - 2-7) to the equation (2-8) results the expression in equation (2-9).

$$r^* = \frac{2\gamma_{sl} * T_m}{Lv} * \frac{1}{\Delta T} \quad (2-9)$$

Equation (2-9) states that increase in undercooling results decreament in critical radius and ΔG^* , or lowering interfacial surface tension provides the same result.

When we substitute the equation (2-9) to (2-7), expression in equation (2-10) can be obtained.

$$\Delta G^*_{homogeneous} = \frac{16\pi\gamma_{sl}^3}{3\Delta G_v^2} \quad (2-10)$$

2.4.1.2 Heterogeneous Nucleation

Any impurities, mold wall, oxides, grain refiners or any other nucleation sites are the source of heterogeneous nucleation. Most of the solidification processes occur via heterogeneous nucleation. Since the required amount of undercooling is very high for homogeneous nucleation, it is rarely occurred. The mechanism playing a role for heterogeneous nucleation could be explained by the decrease in interfacial surface energy. The resulting effect is the decrease in free energy seen in equation (2-7). The nucleus formation is different than homogeneous nucleation [8].

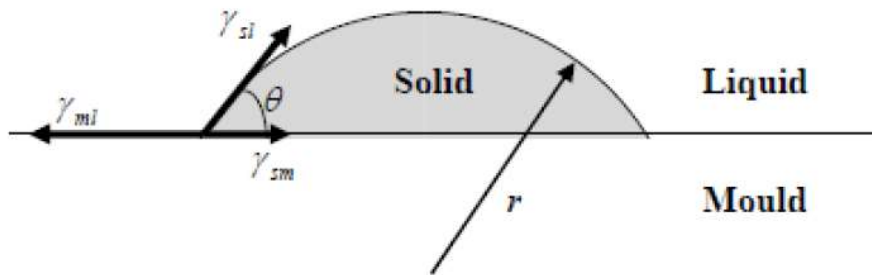


Figure 2.10 Example of heterogeneous nucleation nucleus formation [8]

The number of atoms requiring for the nucleus formation is lower than homogeneous nucleation. Since the interfacial surface energy is decreased, critical radius size is lowered, see equation (2-9). Interfacial energy between the solid and mold can be expressed as follows;

$$\gamma_{ml} = \gamma_{sm} + \gamma_{sl} * \cos(\theta) \quad (2-11)$$

Where,

γ_{ml} : Interfacial surface energy between mold and liquid

γ_{sm} : Interfacial surface energy between solid and mold

γ_{sl} : Interfacial surface energy between solid and liquid

θ : Wetting Angle

$$\Delta G^*_{heterogeneous} = \Delta G^*_{homogeneous} * f(\theta) \quad (2-12)$$

It can be clearly seen that free energy for heterogeneous nucleation is always equal or smaller than homogeneous nucleation since $f(\theta)$ is smaller than 1. The value of undercooling is generally in the order of 1 – 2 K for most of the aluminum alloys [9].

2.4.2 Eutectic Modification

According to the Sigworth, un-refined eutectic morphology becomes acicular form. However, modification elements like Na, Sr, P and heat treatment, especially solutioning, provides to change in the morphology from acicular to fibrous. During transition, below sequence is observed according to the degree of the modification.

1. Acicular form
2. Lamellar structure
3. Transitional lamellar structure
4. Mostly modified structure
5. Fully modified structure
6. Super modified structure

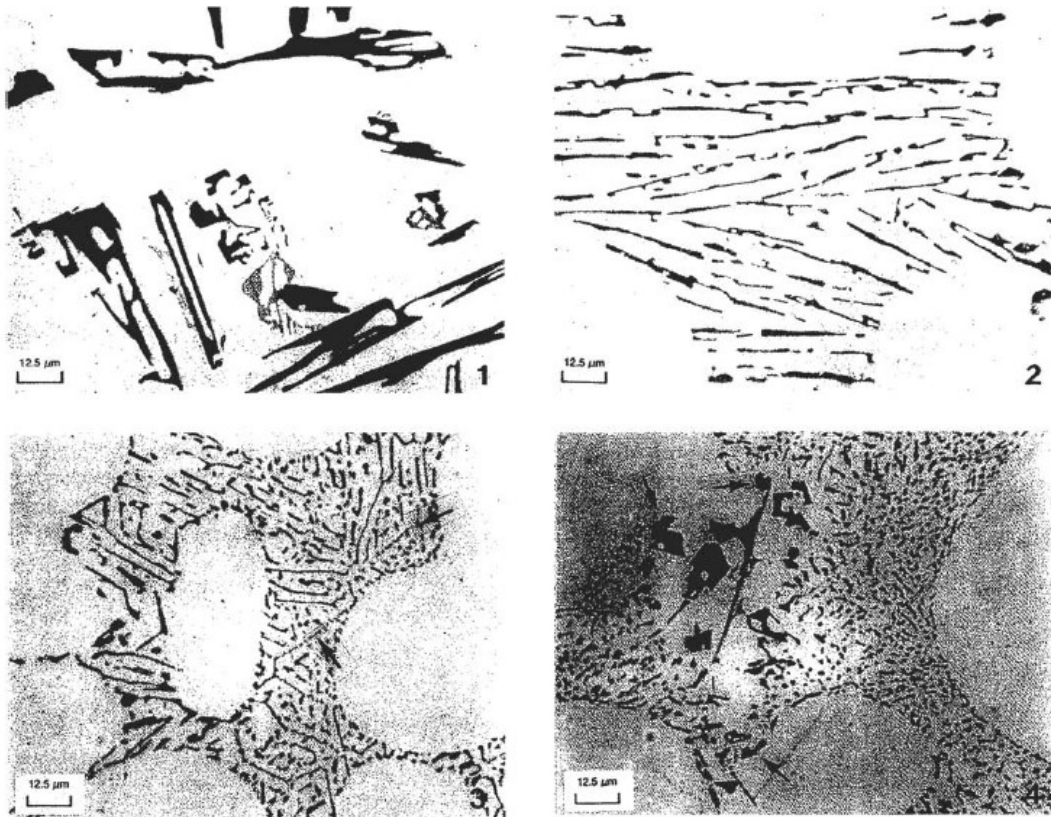


Figure 2.11 Eutectic structure morphologies. (1: Acicular; 2: Lamellar; 3: Transitional Lamellar; 4: Mostly modified structure) [24]

Figure 2.11 examples the eutectic structures from 1 to 4. For the remaining eutectic structures, it is difficult to differentiate via optical microscope [24]. From 1 to 6, amount of strontium addition is increased. In the absence of strontium, acicular eutectic formation is seen in which the growth of silicon nucleus is greater than primary dendrites. As small addition of strontium is added to the melt, lamellar structure is observed in which they become finer. As the amount of strontium is increased, eutectics become more finer and starts to break down, called as transitional lamellar structure. When the amount of strontium is increased, transformation of silicon from acicular/lamellar to the fully modified fibrous structure is completed. During this stage, some larger silicon may even be present. When the all silicon becomes fibrous, it is called as fully modified. Finally, as a rarely occurring, very fine eutectic silicon which is difficult to see by optical microscope is observed [24].

2.4.3 Grain Refinement and Fading

In engineering applications, heterogeneous nucleation happens on a solid substrate sites, such as mould walls, solid precipitate etc., and reduction in free energy depends on θ , contact angle. However, measurement of contact angle does not have any easy measurement method. According to the [15], there is a relationship between the contact angle and intrinsic potency of the substrate, as seen in equation (2-13).

$$\text{Potency} \propto 1/\theta \quad (2-13)$$

Potency can be predicted as shown in equation (2-14) if ΔT is measured.

$$\text{Potency} \propto 1/\Delta T \quad (2-14)$$

Actually, potency of the substrate can be related with mismatch between the lattice of the substrate and nucleating agent. If the intentionally added nucleating agent has a similar lattice mismatch with the substrate, it is called as potent nucleating agent,

which are preferably selected as an inoculation agent for grain refinement. On the other hand, inoculant have also to be chemically stable during the casting process.

Inoculation of aluminum alloys is commonly preferred in order to meet the engineering demands. Grain refinement of aluminum alloys are most commonly carried out by Al-Ti-B master alloys. These master alloys include titanium-based substrates, i.e. TiB_2 and Al_3Ti , which are the nucleation sites for aluminum alloys. The mechanism under the grain size reduction are debatable according to the [16]. It could not be certainly understanding that whether TiB_2 and/or Al_3Ti coated TiB_2 provides the grain refinement.

The idea behind the grain refinement comes from the number of nucleate particles and solute concentration. Nucleate particles provide the formation of heterogenous sites for primary aluminum dendrites while solute particles affect the growth restriction factor in which decreases the growth rate of the primarily nucleated particles by increasing constitutional undercooling. Actually, there are two approach explaining the idea. First one predicts that thermal undercooling is responsible for the nucleation event while classical diffusion growth theory states that constitutional undercooling formed ahead of the dendrite diminishes the growth rate [16]. Easton & StJohn (2005) performed a study in order to examine the both solute affect and number of nucleation agent. They concluded that both parameters play a role for reduction in grain size. They also added that nucleation sites, i.e borides like TiB_2 , has more pronounced affect in low solute concentrations.

2.4.4 Al-Nb-B Based Grain Refiners

Most of the studies about grain refinement for aluminum alloys conclude that grain refinement of Al-Ti-B master alloys are efficient for low silicon concentration, i.e less than 3 wt. %. The reason is that titanium silicide is formed when the amount of silicon is increased in the aluminum alloy. The formation of titanium silicide decreases the number of TiB_2 particles. In the literature, there are lots of studies about

different grain refiners, Al₂TiB, Al₃Ti₃B, AlTiC, AlTiBC, Al₃B. However, since most of them include titanium inside, poisoning arises for the grain refinement of Al-Si-Mg cast alloys. Al₃B has very efficient if the cast material does not contain titanium element. Nevertheless, commercial aluminum alloys have titanium as an impurity. Even the amount is less than, 0.1 wt.%, effectiveness of grain refinement decreases. When the cast material is titanium free, Al₃B is very efficient grain refiner. However, even the amount of titanium is higher than 0.4 wt.%, poisoning is seen [18].

Recent works found that niobium master alloys could be used for the grain refiner agent for Al-Si-Mg cast alloys [20,21,22,23]. Nowak conducted huge amount of experimental studies about Nb-B master alloys for both pure aluminum and Al-Si eutectic alloys and made the comparison with other commercial grain refiners [23]. He explains that Al₃Nb and NbB₂ have similar lattice parameter with Al₃Ti and TiB₂. The reason why niobium-boron master alloys are candidate for the replacement with Al₅TiB can be listed as follows [20,21,22,23];

- Similar lattice parameter with titanium aluminide and titanium boride, which is seen in Figure 2.12 [20].
- Niobium is more stable than titanium providing the formation of niobium silicide at the temperature near to 790 °C [19].

However, growth restriction factor (Q) is much lower than titanium, shown in Figure 2.13.

Element	Phase	Melting point (°C)	Density (g/cm ³)	Lattice structure	Lattice parameter
Aluminium	Al	660	2.7	Face-centred cubic	a = 4.050 Å
Titanium	Ti	1668	4.51	Hexagonal	a = 2.950 Å, c = 4.683 Å
	Al ₃ Ti	1350	3.36	Tetragonal	a = 3.848 Å, c = 8.596 Å
	TiB ₂	3230	4.52	Hexagonal	a = 3.023 Å, c = 3.220 Å
	TiC	3160	4.93	Face-centred cubic	a = 4.330 Å
Niobium	Nb	2468	8.57	Body-centred cubic	a = 3.300 Å
	Al ₃ Nb	1680	4.54	Tetragonal	a = 3.848 Å, c = 8.615 Å
	NbB ₂	3036	6.98	Hexagonal	a = 3.102 Å, c = 3.285 Å
	NbC	3490	7.82	Face-centred cubic	a = 4.430 Å

Figure 2.12 Lattice Parameters Comparison of Aluminum, Titanium and Niobium [20]

Element	k_i	m_i	Maximum Concentration (Wt Pct)	$m(k - 1)$
Ti	7.8	33.3	0.15	~220
Ta	2.5	70	0.10	105
V	4.0	10.0	~0.1	30.0
Hf	2.4	8.0	~0.5	11.2
Mo	2.5	5.0	~0.1	7.5
Zr	2.5	4.5	0.11	6.8
Nb	1.5	13.3	~0.15	6.6
Si	0.11	-6.6	~12.6	5.9
Cr	2.0	3.5	~0.4	3.5
Ni	0.007	-3.3	~6	3.3
Mg	0.51	-6.2	~3.4	3.0
Fe	0.02	-3.0	~1.8	2.9
Cu	0.17	-3.4	33.2	2.8
Mn	0.94	-1.6	1.9	0.1

Figure 2.13 Growth Restriction Factor of Potential Grain Refiner Elements [16]

As explained previously, growth restriction factor is an intrinsic factor of each element and the empirical relation among the growth restriction factor and grain size is shown in equation (2-15).

$$d = a + \frac{b}{Q} \quad (2-15)$$

where a is an experimental constant which is depend on number of nucleating agents, and b is an intrinsic parameter, and Q is growth restriction factor. Equation (2-15) is explained in detail by Easton and Stjohn in their studies [16]. When growth restriction factors of both titanium and niobium is compared, it is seen that titanium has the largest value. However, researches started to develop niobium boron-based grain refiners for the usage of Al-Si cast alloys due to poisoning effect. Since the application area of Al-Si cast alloys have broad range, especially for aerospace and automotive industries, recent studies include niobium boron-based grain refiners. However, since it was recently found, the subject is open to examine in more detail. Still, there is not a common stoichiometric master alloy for Al-Nb-B. Most of the

studies conducted by Nowak and his team focused on Al₂Nb₂B master alloy by taking the pure powdered form of niobium as a starting material.

In this thesis, Al_{2.79}Nb_{0.3}B master alloy will be examined in A357 alloy [12]. The aim of this thesis is to achieve the decrement in grain size, and modification of eutectic phase. Then, the results will be compared with the commercial alloys.

CHAPTER 3

EXPERIMENTAL PROCEDURE

3.1 Raw Materials

A357.0 alloy was used as a base material. As the grain refiner alloys, commercial Al5TiB and Al8B alloys, and Al2.79Nb0.3B master alloys were prepared.

3.1.1 A357.0 Base Material

The chemical composition given in the material certification is written in Table 3.1. It is the base material used in the experiments in order to modify the grain structure.

Table 3.1 Chemical Composition in AMS 4219 Material Specification (wt. %)

Al	Si	Fe	Cu	Mn	Mg	Zn	Ti	Be
Bal.	6.5 – 7.5	Up to 0.20	Up to 0.20	Up to 0.10	0.40 – 0.70	Up to 0.10	0.04 – 0.20	0.04 – 0.07

3.1.2 Commercial Grain Refiner - AL5Ti1B

Thin rod formed commercial alloy was used. Table 3.2 indicates the chemical composition.

Table 3.2 Chemical Composition of Commercial Al5Ti1B (wt. %)

Al	Si	Fe	Ti	B	V	Total Others
93.73	0.06	0.1	5	1	0.1	0.1

3.1.3 Commercial Grain Refiner – AL8B

Commercially purchased master alloy were used. Table 3.3 indicates the ICP-OES results of the Al8B grain refiner alloy.

Table 3.3 Chemical Composition of Al8B (wt. %)

Al	B
92.0	8.0

3.1.4 Al2.79Nb0.3B Master Alloy

In order to obtain the master alloy in the desired chemical composition, Al4Nb master alloy, commercially pure Al (99.7%) and Al8B alloys were used. Intentionally cast alloy will be called as Master Alloy during this thesis.

3.1.4.1 Al4Nb Master Alloy

The alloy was taken from CBMM company. The targeted composition was near to 4 wt.%. ICP-OES and XRF analyses were performed to determine Niobium concentration, the photographs of the Al4Nb alloy is given in Figure 3.1.



Figure 3.1 Al4Nb Master Alloy Blocks

3.2 Mould Preparation

Three different moulds were prepared for the casting of base metal and master alloy.

3.2.1 Resin Bonded Sand Mould

Sand casting were preferred in order to represent the slow cooling rates. AFS 45-55 silica sand and Alkafen C-150 phenolic resin, provided by Cukurova company were used for the sand and resin mixture. After mixing resin and sand for 15 min, they were poured into the mould cavity. Then, CO₂ were passes through the sand – resin mixture rammed in the mould for hardening. It provides to obtain less moisture and reduces the hardening time such as 25 min. Therefore, it is enough to reach sufficient strength of the mould. Two types of mould were used. The first one is resin bonded sand mould shown in Figure 3.2. It was used to obtain tensile specimens.



Figure 3.2 Tensile Specimen Mould

The other mould which is called as “stair” was used to obtain different cross sectioned part for the observation of different solidification times. In this mold, 9 mm, 12 mm, 20 mm and 40 mm cross sectional specimens were cast.

Sand moulds were heated to 110 °C just before the casting in order to remove the moisture inside the sand and alkafen resin mixture. In some of the experiments, gating is separated by filling the position by sand in order to achieve different compositions in the same mold.

3.2.2 Permanent Mold

Pre-heated permanent metal mold was used for the preparation of master alloys. Molds were heated to the 210 °C before casting.



Figure 3.3 Permanent Moulds used for Master Alloys

3.3 Casting Process

For the melting of the raw materials, induction furnace was used. Brand name of the furnace is Inductotherm. Figure 3.4 illustrates the furnace equipment. In addition to Inductotherm furnace, Prothotherm resistant was also used to perform proper

alloying in the case of different grain refiners used in the same melt of A357.0 alloy. After the charge material prepared in Ajax Magnethermic induction furnace, melt was carried to the Prothoterm furnace by using ladle in the required quantity. After proper addition of grain refiners, melt was poured into the mold.



Figure 3.4 Ajax Magnethermic Induction Furnace



Figure 3.5 Induction Furnace “Prothoterm”

3.3.1 Master Alloy Casting Process

The necessary raw materials for the preparation of master alloy casting are listed in Table 3.4. The targeted compositions of the niobium and boron elements are given in Table 3.5.

Table 3.4 Amount of Raw Materials for Master Alloy Preparation

Raw Material	Amount (g)
Al4Nb	400
Pure Al	180
Al8B	22
Total Amount	602

Table 3.5 Targeted Weight Percentages of Master Alloy

Elements	Targeted Composition (wt. %)
Al	Bal.
Nb	2.79
B	0.3

Pure Aluminum alloy was melted in the induction furnace. The melt was hold at 790 °C for homogenization. Then, the temperature is increased to 850 °C. Al8B was added to the melt and it was left to allow the dissolution and homogenization of the aluminum boron alloy. The melt was hold at 850 °C for a 30 min. Then, Al4Nb alloy was added. The system was adjusted to be kept at same temperature for 2 h. Since the preparation was performed at a lab scale, fluctuations on the temperature were observed. During isothermal waiting, the melt was stirred every 15 min. in order not to allow settlement. Then, temperature was decreased to the 740 °C, and the melt was poured to pre-heated metal mould shown in Figure 3.3.



Figure 3.6 Master Alloy

The cast product shown in Figure 3.6 was called as “Master Alloy”.

3.3.2 A357.0 Alloy Casting Process

Firstly A357.0 alloy was melted in induction furnace. After the raw material is melted, temperature was elevated to the 790 °C. At this temperature, grain refiner was added according to the planned experiments. Both commercial Al5Ti1B, Al8B and master alloys were experienced. The contact time was selected as 30 min to avoid fading. Afterwards, alloy was cooled to 740 °C and it was poured to the pre-heated sand mould.

Table 3.6 Summary of intentionally cast alloys

Alloy Type	Chemical Composition	Casting Method	Aim of the alloy preparation
Master Alloy	Al2.79Nb0.3B	Metal Mould, Figure 3.3	To achieve 0.1 wt.% Nb on A357 alloy.
Alloy I	A357 alloy	Sand Tensile Specimen Mould and Sand “Stair” Mould, Figure 3.2	To compare the results with base material.
Alloy II	A357 alloy + 0.1 wt.% Nb	Sand Tensile Specimen Mould, Figure 3.2	To see grain refinement effect.
Alloy III	A357 alloy + 0.1 wt.% Ti	Sand Tensile Specimen Mould, Figure 3.2	To see grain refinement effect.
Alloy IV	A357 alloy + 0.026 wt.%B	Sand Tensile Specimen Mould, Figure 3.2	To see grain refinement effect.

Totally four different compositions were targeted. Alloy I was taken as a reference of A357.0 alloy. Then, Alloy II, III and IV were aimed to achieve 0.1% of Nb, 0.1% of Ti and 0.026% of B, respectively. The aim of the Alloy IV is to observe the effect of boron added in the equal amount with other alloy types without addition of any titanium. Titanium inside the A357 was the only source of titanium for Alloy IV. Table 3.6 summarize the alloy types cast during the experimental studies.

3.4 Chemical Analysis

After casting was completed, the specimens were prepared not only from the gating but also from the thermal analysis specimens, shown in section 3.5. Figure 3.8 shows the spectrometer analysis specimens extracted from the risers. Optical Emission Spectroscopy were utilized for chemical analysis of the alloys.



Figure 3.7 WAS Foundry Master optical emission spectroscopy [10]

In this thesis, WAS Foundry Master optical emission spectroscopy used for element analysis is shown in Figure 3.7.



Figure 3.8 Chemical Analysis Specimens of Alloy I, II, III and IV

Since the machine shown in Figure 3.7 does not have the energy levels of each element in the periodic table, niobium element was added to the system by the optical emission spectroscopy service company, REPAMET company. They calibrated the device by introducing the niobium element which are characterized by XRF method. The idea behind the XRF method is similar to OES method. The difference is that it is non-destructive method and smaller specimens can be analyzed in a precise manner. However, elements having smaller atomic weight like carbon, boron etc. cannot be analyzed with XRF [11]. That's why, another chemical analysis method, called as ICP – OES, was also used for the characterization of master alloys and base metal. This method also stands for the optical emission spectroscopy method. The only difference is the sample preparation. Liquid state of sample is needed for ICP-OES analysis thereof, chips were obtained from the specimens and they were taken into the solution.

3.5 Thermal Analysis

During the melting stage, holding at isothermal temperature and solidification, temperatures were observed by using K-type Nickel Chromium thermocouples.

Cable and metal thermocouples used during the experiments are shown in Figure 3.9 and Figure 3.10, respectively.

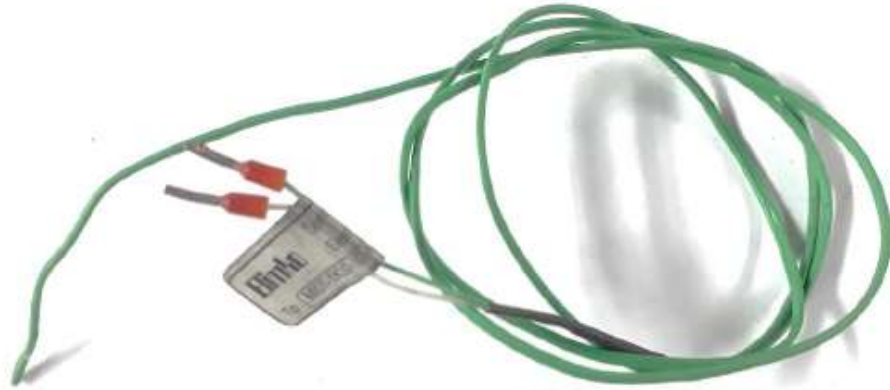


Figure 3.9 K type cable thermocouple [10]



Figure 3.10 K type metal thermocouple [10]



Figure 3.11 Ordel data logger temperature scanner connected to the computer [10]

Temperatures were recorded via thermocouple data-logger, whose brand name is Ordel 100 Universal Data Logger, shown in Figure 3.11. It collects the data every second, having a frequency 1 Hz. Collected data was easily transferred to the computer by using Dali data acquisition software. Software allows the transferring of the tabulated temperature values to the excel file. Then, temperature vs. time graph was easily obtained in the excel file. In addition, first and second derivatives of the graph were obtained by MATLAB program to determine the liquidus and solidus temperatures precisely. Moreover, amount of undercooling was graphically measured for liquidus and eutectic transformation. Example of cooling curve together with its first derivative is given in Figure 3.12

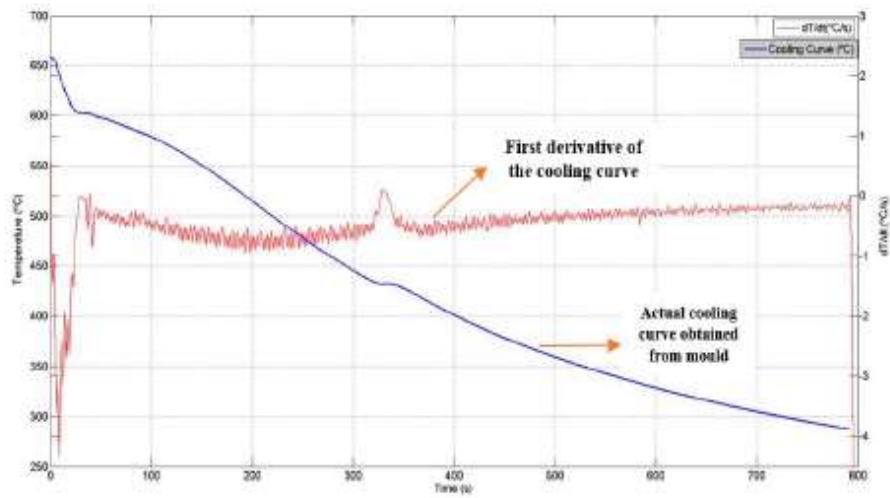


Figure 3.12 Primary and first derivative cooling curves of the same thermal analysis experiment

Cable thermocouple defined in Figure 3.9 was used for thermal analysis from the cast part. It was placed to the ingate of the mold. Apart from thermal analysis of actual part, specimens were prepared to examine the cooling curve in the quick cap, allowing slow cooling. The geometry and equipment of quick cap is shown in Figure 3.13.



Figure 3.13 Thermocouple location in the Quick cap

3.6 XRD Measurement

X-ray diffraction analysis was performed in order to determine crystal structures of the phases. Intensity vs. 2θ values were graphed via excel to determine the phases on the samples. Cast samples were prepared from the specimens shown in Figure 3.8 and schematic representation of the graph is given Figure 3.14.

- XRD analysis were performed using the following instrument parameters 0.65 °/min in between 20° and 70° [12].

Bruker brand named machine was used for the experiment. The machine setup is shown in Figure 3.15. Cu- K_{α} radiation used as a radiating element.

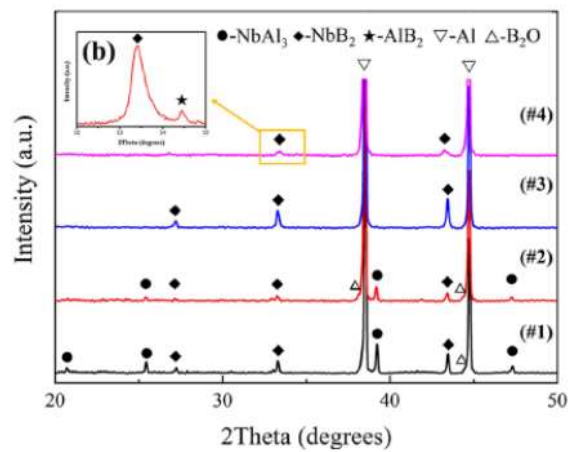


Figure 3.14 XRD chart obtained for master alloy produced [12]



Figure 3.15 XRD instrument used for crystal structure analysis [10]

3.7 Radiographic Inspection

Radiographic inspection was conducted in order to classify the internal defects in the castings to avoid unexpected failure during tensile testing. Digital X-ray was performed at METU Non-Destructive Testing Laboratories. The brand name of machine is ERESKO 42 MF4 200kV. Figure 3.16 shows the example of radiographic examination results.

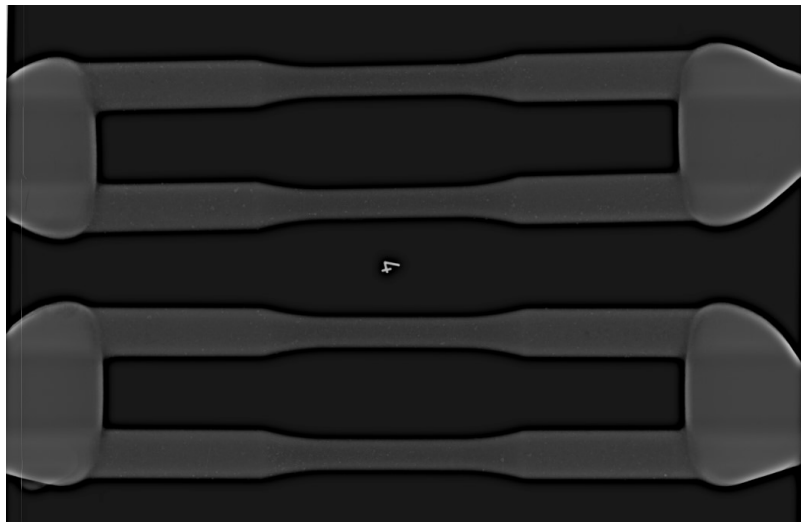


Figure 3.16 Example of digital x-ray inspection results of Alloy II

Radiographic examination results were evaluated in terms of gas porosity, micro shrinkage, internal voids and cracks, and foreign materials, (less dense and high dense).

3.8 Microstructural Examination

For the characterization of the microstructure, optical and scanning electron microscopes were used.

3.8.1 Metallographic Specimen Preparation

Standard specimen preparation steps were followed. Both as-cast and heat-treated specimens were analyzed. Before starting the metallographic specimen preparation, specimens were cut into smaller sections as shown in Figure 3.17.

After specimens were cut into a desired size, mounting device shown in Figure 3.18 had been used. It took approximately 15 min. to be prepared by the machine. Afterwards, mounted specimens were grinded by using 220 – 400 – 600 – 800 – 1200 grid emery papers by using rotating disc grinder, respectively. After grinding, specimens were polished with 6 μ and 1 μ diamond solutions, respectively.

After polished surface is obtained, specimens were etched in order to reveal eutectics, precipitates and grain boundaries. Keller, Kroll and Tuckers' agents were experienced to obtain grain structure clearly. Amounts of chemicals inside the etchants are given in Table 3.7.

Table 3.7 Amounts of Chemicals Inside the Etchants

	HF	HCl	HNO ₃	H ₂ O
Keller	1 ml	1.5 ml	2.5 ml	95 ml
Kroll	2 ml	-	6 ml	92 ml
Tuckers	15 ml	45 ml	15 ml	25 ml

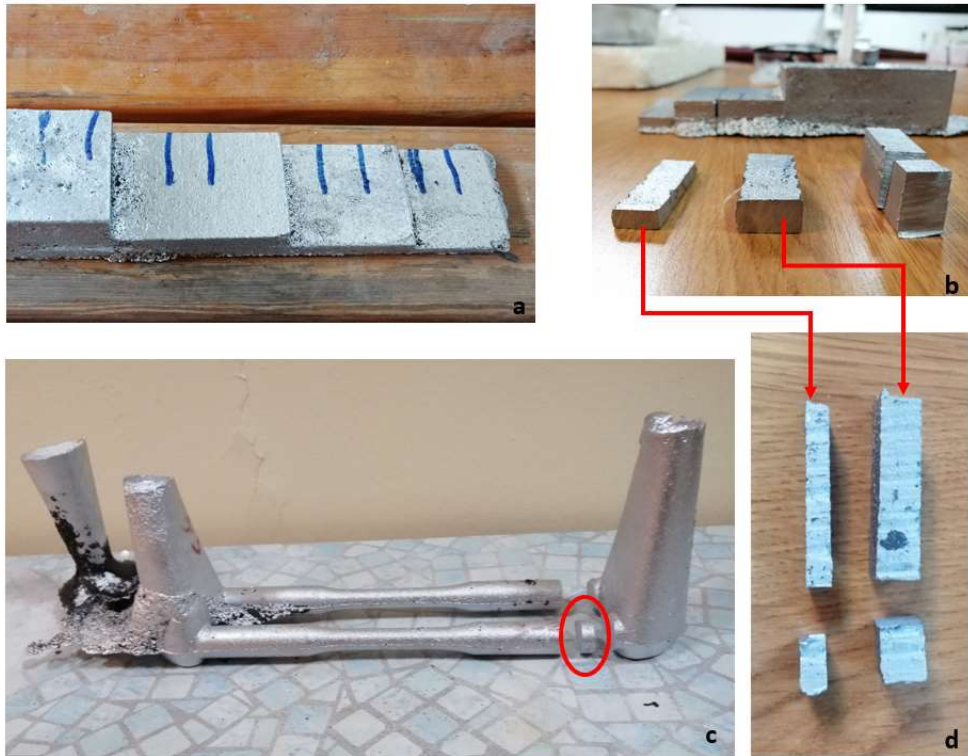


Figure 3.17 Example of specimen extractions; a: Specimens as extracted from the mould, b: Cut into smaller sections, c: Mounting specimen extraction, d: Mounting specimen extraction



Figure 3.18 METACUT 251 grinding cutter (right) and the mounting bakelite device (left) [10]



Figure 3.19 Rotating disc type a: Grinder, b: Polisher with 6 μ and 1 μ diamond solutions [10]

Specimens were exposed to 20 second for Keller and Kroll agents while 3 second was enough to etch the samples with Tuckers agent. Keller and Kroll etchants were used for the determination of grain size and microscopic examination. However, they were not enough for electron microscope examination since more severe etching was required. Therefore, tuckers etchant was preferred to reveal the grain size in more detail.

3.8.2 Optical Microscope Examination

After specimen preparation was completed, they were examined with optical microscopes. Two different microscopes were used for microstructural examination and grain size measurement. Their brand name is Huvitz and SOIF XJP-6A, shown in Figure 3.20.

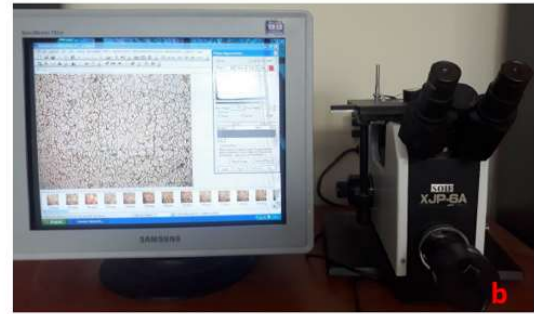
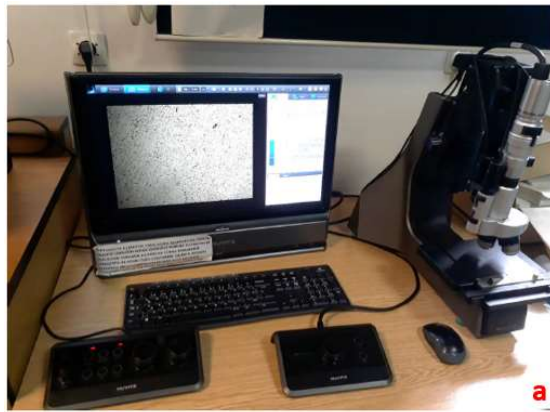


Figure 3.20 Optical Microscopes; a: Huvitz optical microscope, b: SOIF XJP-6A optical microscope

Micrographs were taken in different magnifications, in the range of 50x to 1000x. microstructural review were performed with the microscope shown in Figure 3.20, whose name is Huvitz. Moreover, grain size measurement with the SOIF XJP-6A microscope shown in Figure 3.20 was also conducted in order to compare the cast alloy samples with and without grain refiners. SOIF XJP-6A microscope connected to a computer equipped with De-Winter Material Plus image analysis software. This software works according to the ASTM E-112 grain size measurement specification.

3.8.3 Scanning Electron Microscope Examination

The specimens were analyzed to reveal precipitates and eutectics by using SEM under high magnification. On the other hand, EDS were conducted to detect the element concentrations for each phases or precipitates to compare with XRD results. Since the specimens were mounted with bakalite, which is non-conductive agent, specimens were coated with thin layer of conductive silver plating in order to avoid charging of the bakalite. Scanning electron microscope used for this thesis was NOVA NANO SEM 430, which is seen Figure 3.21. Other than the EDS detector of electron microscope, backscatter and secondary electron detectors were used for characterization.



Figure 3.21 NOVA NANO SEM 430 Scanning electron microscope setup

3.9 Heat Treatment

All cast specimens were heat treated to T6. Firstly, they had been exposed to solutioning in order to dissolve the chemical constituents inside the as-cast samples into the α phase given in Figure 2.2. Then, specimens were water quenched. After water quenching, they had been unstable microstructure, which are called as W condition. Immediately after quenching, water quenched specimens had been treated with artificial aging. The time between quenching and artificial aging was not exceeded to 45 min in order to prevent natural aging.

Before starting the heat treatment of tensile specimens, smaller cut sections were prepared as explained in Figure 3.8 and treated with heat treatment parameters shown below;

- Solutioning: 538 °C 10h
- Artificial Aging: 160 °C 12h



Figure 3.22 Electrical resistance furnace used for heat treatments

Figure 3.22 shows the specimen locations for heat treatment process trial. After hardness measurements of the specimens, heat treatment process parameters were decided to be used for tensile test specimens.

3.10 Mechanical Test

Tensile test was conducted in order to observe yield strength, ultimate tensile strength, and % elongations. Tensile test was conducted with 2 mm/min rate. Calipon type extensometer was used in order to measure % elongation. Instron 5985 electromechanical test machine was used in the tests.

CHAPTER 4

EXPERIMENTAL RESULTS AND DISCUSSIONS

In this chapter, test and inspection results performed during the experiments are explained in detail.

4.1 Chemical Analysis

Before experimental studies had been started, chemical analyses of raw materials were conducted.

4.1.1 Chemical Analysis of Al-Nb Master Alloy

Chemical analysis results of commercially purchased master alloy of Al4Nb were examined via ICP-OES and XRF testing methods. The testing results are given in Table 4.1. According to the (Nowak, 2011) pure niobium was used during Al-Nb-B master alloy preparation. Pure niobium is more preferable for achievement of homogeneous distribution. Since niobium amount in the master alloy is at most 5 wt. %, amount of master alloy was increased for the achievement of proper grain refinement.

Table 4.1 Chemical Composition of Al4Nb (wt. %)

Testing Method	Al	Nb
ICP-OES	Bal.	3.7 ± 0.1
XRF	Bal.	3.99

The differences in results are already expected by all the researches due to higher atomic weight of niobium element [20].

4.1.2 Chemical Analysis of Master Alloy

The Nb and B contents in the master alloy, which were measured via ICP-OES method, are given in Table 4.2.

Table 4.2 ICP-OES test results of Master Alloy

Al (wt. %)	Nb (wt. %)	B (wt. %)
Bal.	1.44	0.29

When the Nb content is compared with the targeted composition, shown in Table 3.5, it is clearly seen that niobium content is decreased to half of the targeted value. Moreover, XRF analysis was also conducted to examine the niobium content for master alloy. The weight percentage is also found as 2.40 wt. % via XRF analysis.

It can be easily seen that same specimen shows variety in niobium content. In order to observe the niobium distribution, specimens prepared from the different locations were tested via XRF and the concentration are given in Table 4.3 together with ICP-OES results.

Table 4.3 XRF and ICP-OES chemical analysis results of Master Alloy

Alloy	Measurement Method	Results
Master Alloy	XRF analysis	1.98 wt. %
	XRF analysis	2.40 wt. %
	ICP-OES analysis	1.44 wt. %

XRF analysis confirmed that niobium amount in the master alloy is comparatively lower than the expected. Both ICP-OES and XRF analysis reveal that there are non-homogeneities in the master alloy. It may be due to;

1. Higher atomic weight of niobium element resulting sedimentation
2. Lab scale alloying process resulting improper mixing and non-homogeneity.

4.1.3 Chemical Analysis of Alloy I, II, III and IV

After the master alloys were prepared, they were used for grain refinement of A357.0 alloy. They were chemically analyzed via optical emission spectroscopy. Chemical analysis results are given in Table 4.5. When chemical compositions of targeted grain refiner elements given in section 3.3.2 are compared with spectrometric analysis results, it is seen that targeted compositions are achieved. In addition, Table 4.4 indicates the targeted compositions of each alloy system.

Table 4.4 Targeted chemical compositions of each alloy types (wt. %)

	Al	Si	Mg	Fe	Ti	Nb	B	Other
Alloy I	91.00	8.05	0.53	0.08	0.13	0	0.01	Remainder
Alloy II	91.58	7.40	0.49	0.07	0.12	0.11	0.03	Remainder
Alloy III	91.02	7.99	0.53	0.08	0.16	0	0.03	Remainder
Alloy IV	91.00	8.02	0.53	0.08	0.13	0	0.04	Remainder

Since commercially used A357.0 alloy contains titanium as an impurity, amount of titanium presents for each alloy type. Alloy I represent the A357.0 alloy without any grain refiner addition, and alloy III and IV represents the grain refinement via Ti and B elements. Their chemical compositions are very similar. Another point which can be revealed from the chemical analysis is the difference in the silicon content. It is easily seen that amount of silicon is nearly same for Alloy I, III and IV while it is decreased by 0.5 wt. % for Alloy II. The reason may come from the addition of niobium and boron-based master alloy.

- Since the weight percentage of niobium is very low for intentionally developed master alloy compared with commercial Al5TiB, amount of

master alloy was increased to maintain 0.1 wt.% Nb content. It caused to decrease silicon concentration.

- Measurement error can be another reason explaining the difference. Preparation of chemical analysis specimen, calibration of spectrometric machine, amount of protective gaseous used during spark initiation could affect the chemical compositions.

Table 4.5 Optical Emission Spectroscopy results of Alloy I, II, III and IV (wt. %)

Wt.%	Al	Si	Mg	Fe	Ti	Nb	B	Other
Alloy I	90.9	8.09	0.57	0.10	0.14	0.01	0.01	Remainder
Alloy II	91.4	7.61	0.46	0.08	0.13	0.11	0.01	Remainder
Alloy III	90.9	8.15	0.52	0.08	0.18	0.03	0.02	Remainder
Alloy IV	90.9	8.09	0.54	0.09	0.15	0.02	0.02	Remainder

4.2 Determination of Liquidus, Eutectic Temperatures and Undercooling

Cooling curves for each alloy were examined via thermocouple and data logger shown in Figure 3.9 and Figure 3.11, respectively. Data recorded by the machine was moved to a computer as Excel file and, cooling curves were drawn by using MATLAB software. First and second derivatives were obtained in order to determine the critical solidification temperatures such as liquidus, solidus and undercooling etc.

Three critical temperature ranges were observed from the cooling curves, liquidus, eutectic and solidus. They are indicated in Figure 4.1 as region 1, 2 and 3. Each temperature range is examined in detail. More detailed views are given in Figure 4.4, Figure 4.5 and Figure 4.6, separately. Critical temperatures defined in Table 4.6 are

calculated by using the first and second derivative of temperature vs. time graphs for each alloy. During identification of primary alpha nucleation temperature, second derivative curves given in Figure 4.3 were used. Start of the sharp increase from “0” were taken in the second derivative curve as nucleation start temperature. Peak points of first and second derivatives are nearly similar, and they indicate the minimum temperature, defined as a temperature which is below the transformation temperature. Finally, the point in which second derivative becomes “0” were selected as growth temperature where the temperature of the system is increased in an amount of undercooling. Moreover, remaining peak points in the first derivative curves are selected to define eutectic and solidus temperatures. For eutectic temperature identification, starting point of the peak is taken as nucleation temperature while peak point and returned point of first derivative graphs are taken as minimum and growth temperatures.

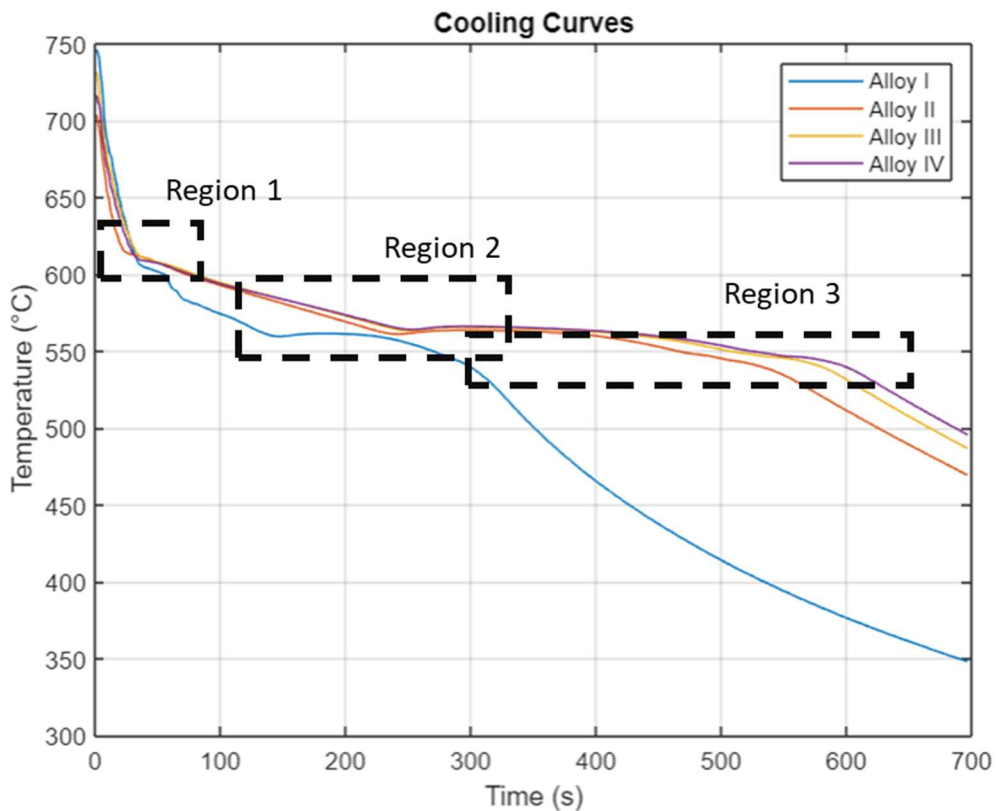


Figure 4.1 Cooling Curves of Alloy I, II, I II and IV

First region of Figure 4.1 includes primary aluminum dendrites nucleation and growth. For all of the experiments, it is expected to see undercooling, even in small amount. Especially, undercooling is expected to be decreased by the addition of grain refiners. The reason why undercooling is not detected for these alloys may be come from the frequency of the Data Logger shown in Figure 3.11. The machine frequency is 1 Hz. Amount of undercooling may not be visible with 1 Hz machine. Higher frequency may be needed in order for liquidus determination. For example, [14] conducted its experiment via 20 Hz data logger for critical temperature determinations. Cooling curves of each alloy type and their second derivatives are given in Appendix A.

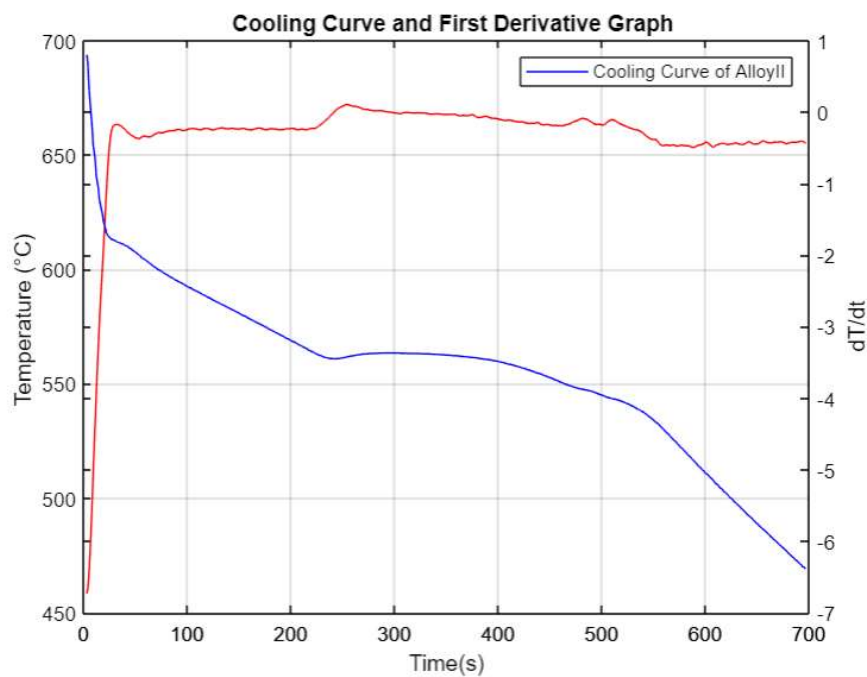


Figure 4.2 Temperature vs. time and first derivative curves

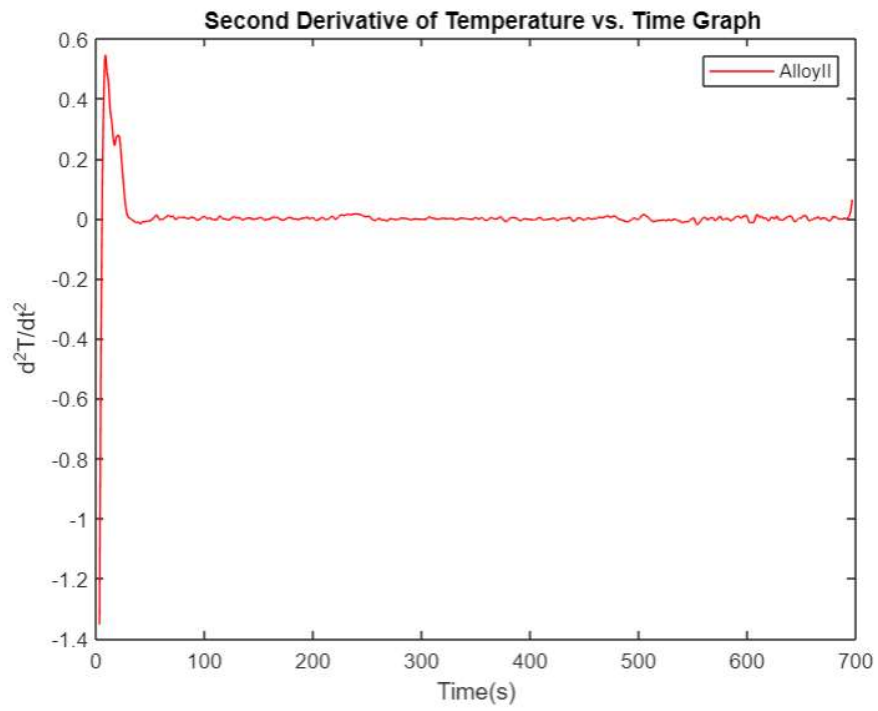


Figure 4.3 Second derivation of temperature vs. time graph

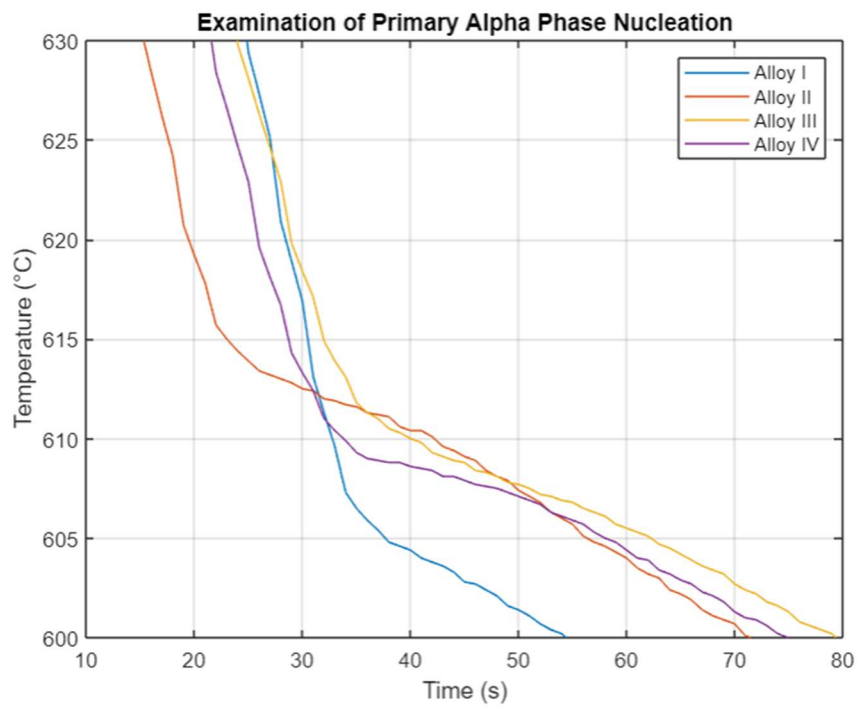


Figure 4.4 Primary alpha nucleation and growth zone of Alloy I, II, III and IV

When Figure 4.4 is reviewed, it is obviously seen that liquidus temperature is increased for grain refined alloys. The highest temperature belongs to Alloy II, grain refined with prepared master alloy, which is also indicated in Table 4.6. In addition, it can be concluded that dendrite formation starts earlier for the niobium inoculated alloy, called as Alloy II.

Region 2 defined in Figure 4.1 represents the nucleation and growth of eutectic phase. When eutectic nucleation start and growth temperatures are compared together with undercooling amount, it is seen that Alloy II has the largest undercooling and lowest phase transformation temperatures. It can be understood that nucleation temperature is depressed as seen in Table 4.6. The results can be supported by the research found in literature [28].

Moreover, Figure 4.1 also shows that thermal arrest is longer for the Alloy II and III, causing longer freezing time. This is also indicative of eutectic modification. Normally, binary aluminum and silicon reacts at 577 °C according to the Figure 2.5. However, it is also seen that even there is no grain refiner is added, especially for Alloy I, the eutectic temperature is depressed. This is also verified by the microstructural examination since the eutectic structure does not have fully acicular structure, as expected for binary Al-Si. It includes also lamellar structure in some locations.

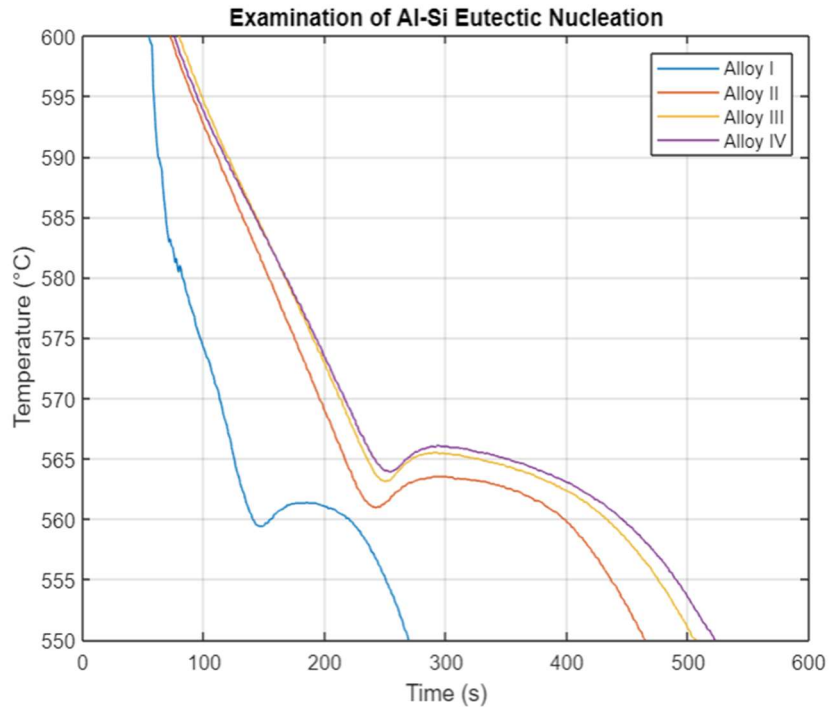


Figure 4.5 Al-Si eutectic nucleation and growth zone of Alloy I, II, III and IV

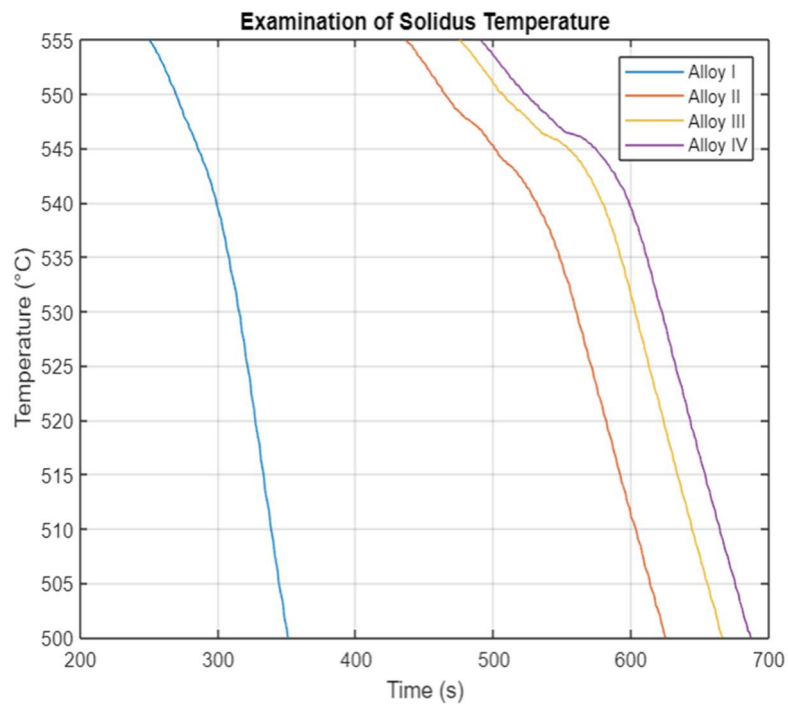


Figure 4.6 Solidus temperature zone of Alloy I, II, III and IV

Finally, when region 3 is examined. 3 peaks are seen. They are given in Appendix A, separately. They are identified as A, B and Ts. Temperatures are given in Table 4.6. The point A belongs the formation of Mg₂Si, and B point indicates the formation of π phase, as mentioned in Figure 2.5 [7]. Finally, latest peak point is an indication of solidus temperature where the solidification is completed.

Table 4.6 Critical Solidification Temperatures of Alloy I, II, III and IV (°C)

	Tn (l)	Tmin(l)	Tg (l)	ΔT (l)	Tn (e)	Tmin (e)	Tg (e)	ΔT (e)	Ts
Alloy I	607,3	NA	603.8	NA	566,5	559.4	561.4	2	A:548,7 B:536,7 Ts:532
Alloy II	617.8	NA	610.4	NA	562	560.9	563.5	2.6	A:547,3 B:543,5 Ts:531
Alloy III	613.9	NA	607.8	NA	563.8	563.1	565.5	2.4	A:546,1 B:543,8 Ts:528.5
Alloy IV	610.4	NA	605	NA	565,8	563.9	566.1	2.2	A:546,2 B:542,1 Ts:534.5

Tn: Nucleation Temperature where T (l) represents the formation of first aluminum dendrites, and T (e) represents the nucleation of first Al-Si eutectic precipitates.
Tmin: Minimum temperature required to provide undercooling below the transformation temperature. Tmin (l) represent the minimum temperature for primary aluminum dendrites, and Tmin (e) represent the minimum temperature for Al-Si eutectic.
Tg: Growth temperature where Tg (l) represent the growth of aluminum dendrites, and Tg (e) represents the growth of eutectic Al-Si.
 ΔT : Undercooling where ΔT (l) for aluminum dendrites, and ΔT (e) for Al-Si eutectic.
A: Mg₂Si phase transformation temperature
B: π phase transformation temperature
Ts: Solidus Temperature

According to the thermal examination results;

1. Liquidus temperatures are increased for Alloy II and III, which is expected for grain refinement [20].
2. Nucleation of primary dendrites starts earlier with the help of niobium – boron inoculation.
3. Liquidus undercooling is not detected due to lower frequency of data logger.
4. Eutectic undercooling is increased, and nucleation temperature is depressed, and freezing range is increased for Alloy II indicating eutectic modification.
5. π phase reaction temperature is the lowest for Alloy I.

4.3 XRD Measurements

Specimens prepared for XRD experiments were examined in order to describe the phases formed inside each alloy designation. Experimental parameters are given in section 3.6.

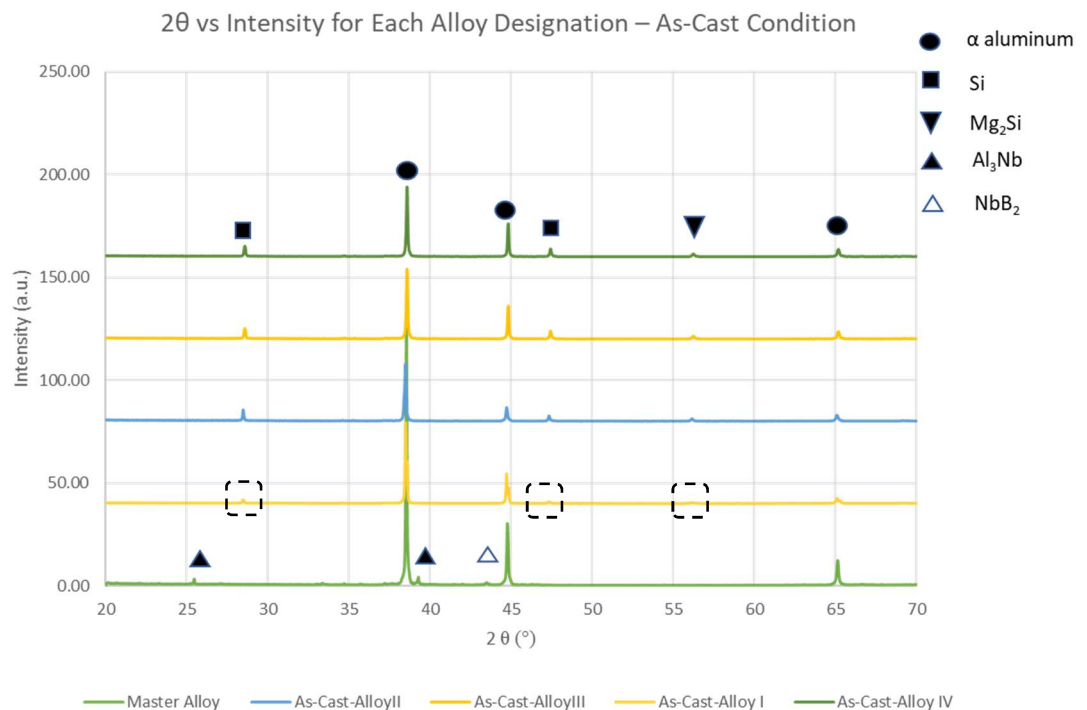


Figure 4.7 XRD Peaks of Alloy I, II, III and IV As-Cast Alloys

When Figure 4.7 is reviewed, for each of the alloy type, same peaks arise, which are primary aluminum, eutectic silicon, magnesium silicide. Since chemical compositions are nearly same for 4 alloy types, as given in section 4.1.3, it is expected. Below results can be induced;

- Alloy I have a very low intensity amount for the dashed rectangular specified regions. Since it has not been treated with grain refiner, more localized eutectics are seen. That's why, since xrd measurement is performed from the specimen, it may not represent the whole alloy. Another reason is that since magnesium and silicon elements dissolve in the matrix, they could not be detected via X-Raf diffraction. On the other hand, Figure 4.8 reveals the peaks which are not seen in the as- cast condition. Localized precipitates formed as a result of heat treatment, and eutectic silicon are expanded evenly. This yields to see the peaks which are already presented in the as-cast condition but they are localized.

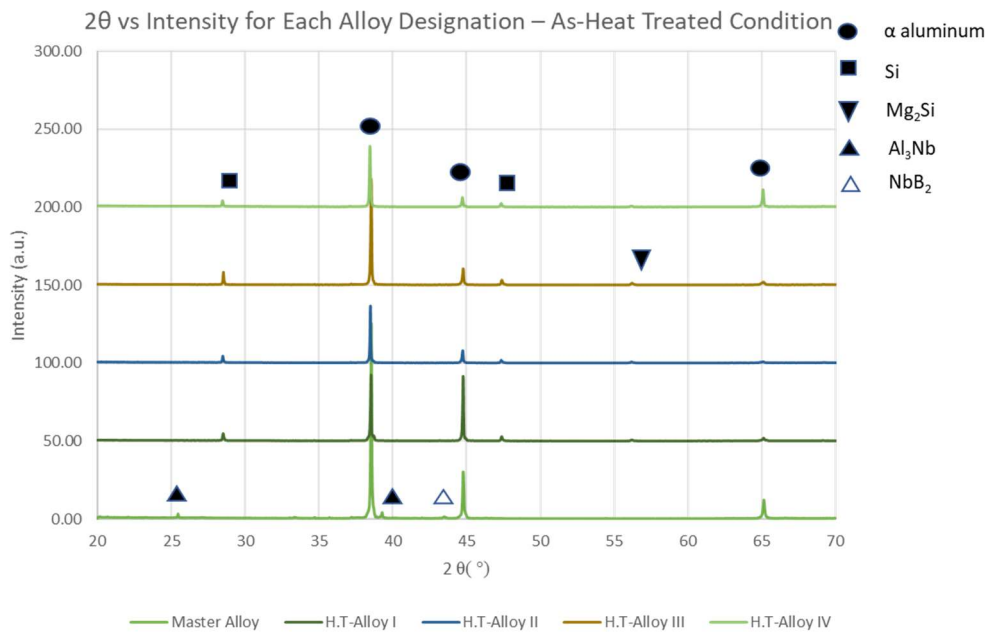


Figure 4.8 XRD Peaks of Alloy I, II, III and IV As-Heat Treated Alloys

Moreover, Figure 4.9 indicates the phases formed in the Al-Nb-B based master alloy. It is seen that already mentioned phases in section 2.4.4 has peaks in intensity vs. 2θ graph even the amount of intensity has smaller in the master alloy. It is seen that Al_3Nb and NbB_2 precipitates providing nucleation sites for A357.0 alloy is observed. However, these precipitates and also nucleation agents like Al_3Ti and TiB_2 included in A15TiB and A18B are not seen in Alloy I, II, III and IV. Since the amount of grain refiner elements is 0.1 wt. %, they cannot be detected via XRD measurement. The formation of these phases is investigated with optical and electron microscopes.

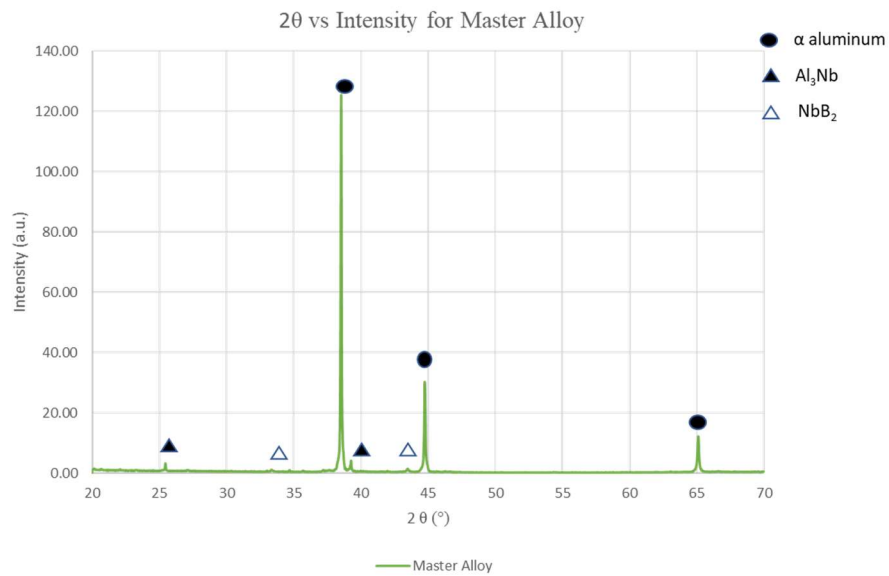


Figure 4.9 XRD Peaks of Master Alloy

4.4 Microstructural Analysis

This chapter explains the optical and electron microscope examination results. In this chapter, overview of general microstructure, distribution of secondary phases, morphology and size of the eutectics are presented in detailed.

4.4.1 Optical and Electron Microscope Examinations

Figure 4.10 shows the microstructure of Alloy I. It is shown that red circled areas are solidified under highly thermal gradient. Since no grain modification element is added to the alloy, it was solidified under thermal gradient, which caused elongated dendritic structure. However, since the alloy includes titanium as an impurity and other alloying elements according to the spectroscopic analysis shown in Table 4.5, constitutional undercooling caused by solute concentration inside provides equiaxed grains in some regions.

Red circled areas indicated as 'a' letter in Figure 4.10 shows the elongated dendritic structure while green one shows the equiaxed grains. Therefore, Alloy I include both equiaxed and dendritic structure. The microstructural examination results performed in deeper via scanning electron microscope is given in Figure 4.11. Both matrix, eutectic phase and Mg_2Si precipitates can be seen. Since the etchant used during electron microscope examination is Keller with 20 sec., the grain boundary structure with eutectic phase can be observed as transparent.

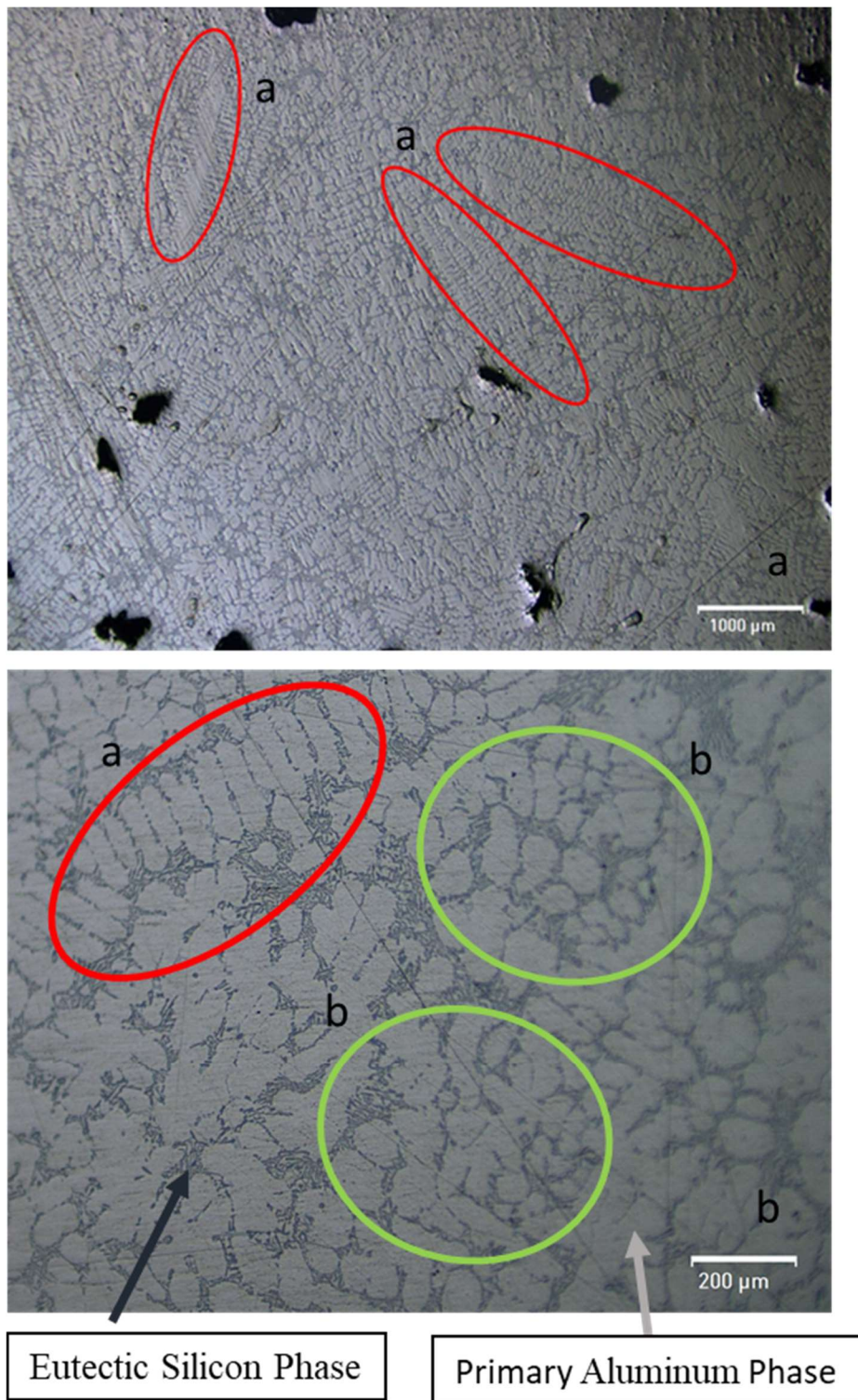


Figure 4.10 Optical Microstructure Images of Alloy I etched with Keller's reagent (a:50x magnification; b:200x magnification)

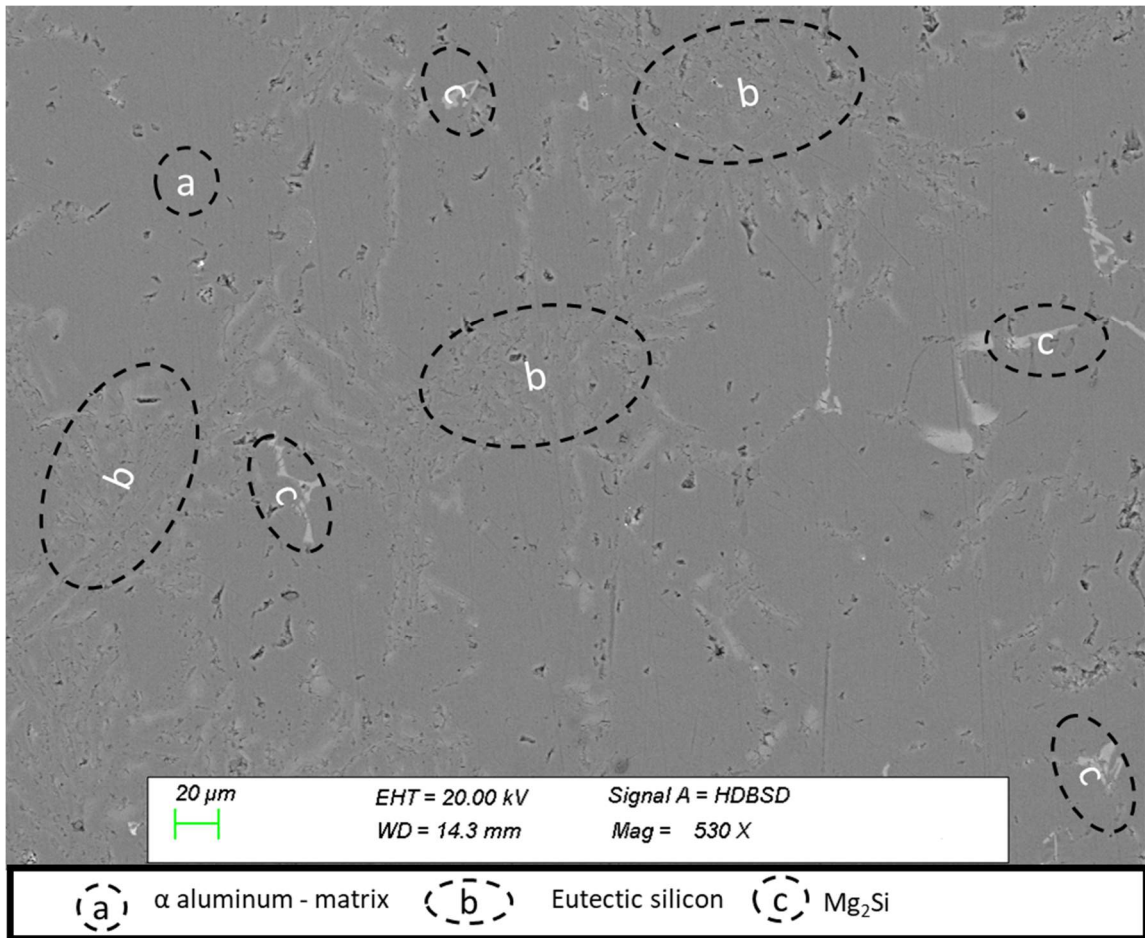


Figure 4.11 Scanning electron microscope results of Alloy I

In addition to the distribution of grain size, which will be examined in section 4.4.2, morphology of the eutectic is examined and the images are shown in Figure 4.12.

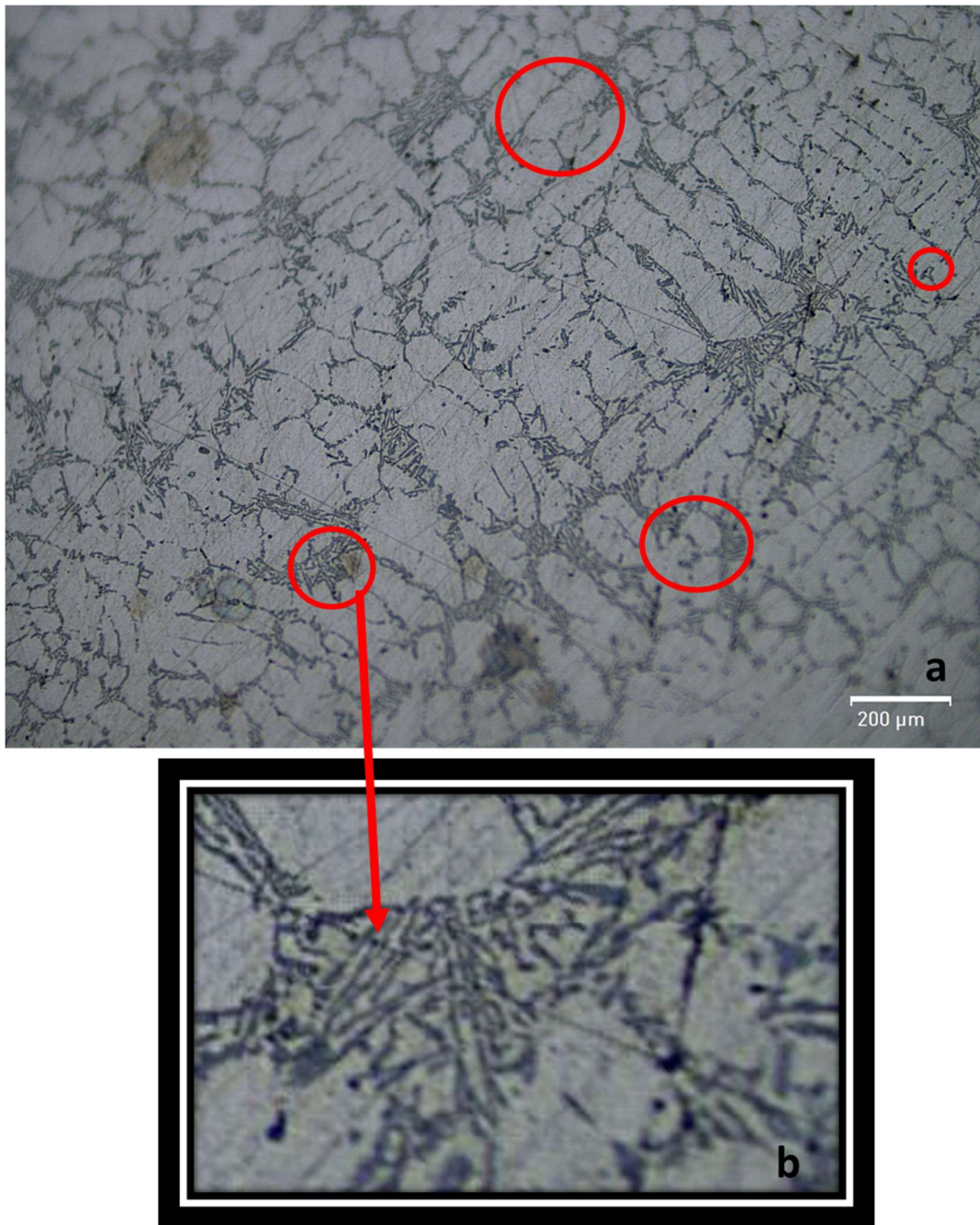


Figure 4.12 Optical microscope images of acicular eutectic morphology of Alloy I etched with Keller's reagent (a: 200x magnification b: zoomed view)

Figure 4.12 shows the acicular/lamellar eutectic structure. Red circled and identified as "a" letter area represent the eutectic silicon structure. Since Alloy I is un-refined and it is in as-cast condition, this structure is expected.

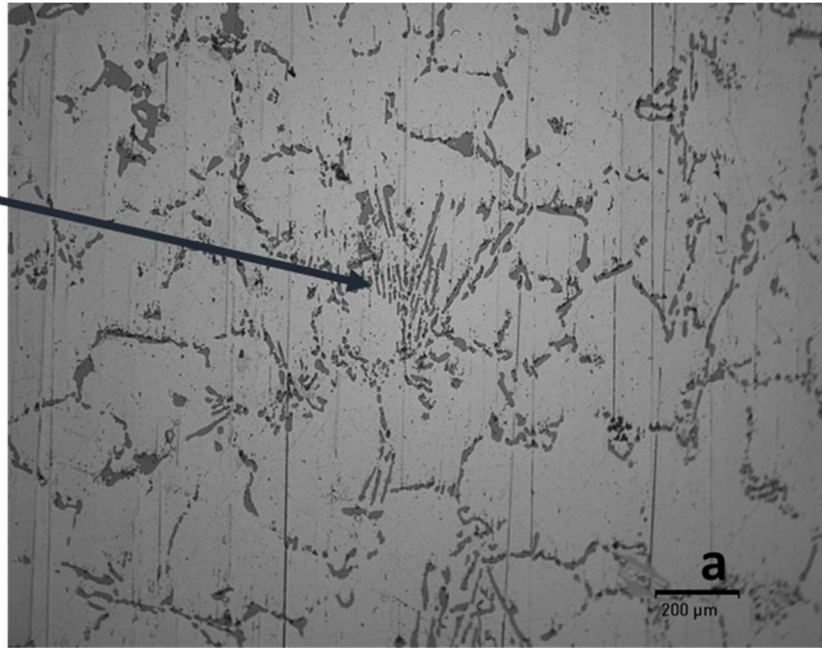
Acicular morphology of eutectic silicon can be changed even the alloy poured without any modification. solutioning treatment provide the change in morphology of eutectic silicon. Sigworth states that solutioning at 538 °C for 12 h can achieve modification [24]. Especially, 1 hour of solutioning is enough for Mg₂Si formation, remaining time is necessary for the spheroidization of eutectic silicon. Figure 4.13 shows the transition lamellar and fibrous eutectic morphology as a result of solutioning at 538 °C for 10 h and aging at 160 °C for 12h. Therefore, it can be concluded that modification can reduce the heat treatment time, which is very beneficial for industry. However, modification also has some negative effects, in terms of porosity formation.

When the microstructure of Alloy III is examined via both optical and electron microscope, same phases are seen with Alloy I. Especially, it is expected by examining XRD results in section 4.3. major phases like Mg₂Si, eutectic Si and aluminum matrix are both verified via optical and electron microscope. Only difference is seen in morphology of eutectic and grain size distribution.

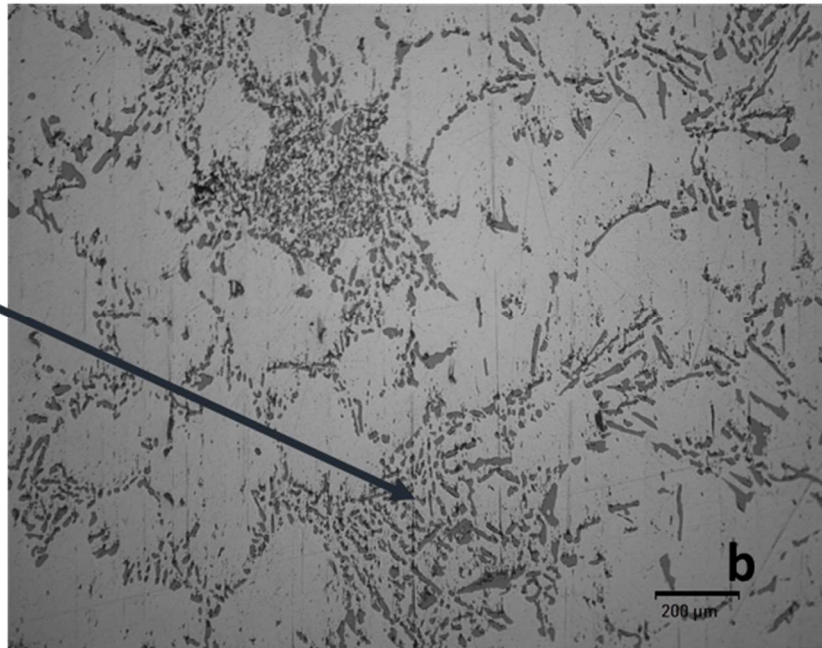
In this chapter, eutectic phase is examined in detail. Figure 4.14 shows that eutectic phase includes both fibrous and transition lamellar structure. It is seen that addition of Al₅TiB has some impact on eutectic morphology. Especially, since grain size is decreased by adding grain refiners, the growth rate of primary aluminum phase is decreased. Since the morphology of eutectic phase depends on the growth rate of silicon, it may be revealed that the modified regions are resulted from the reduction in the growth rate of primary aluminum. Microstructural examinations can be correlated with thermal analysis. Table 4.6 shows that eutectic undercooling is increased for Alloy III. However, still acicular and lamellar structure is seen even the amount of acicular eutectic silicon is lower than Alloy I.

Moreover, Figure 4.14 also reveals the reduction and more even distribution grains of Alloy III. Reduction in grain size and homogeneous distribution is expected for Al₅TiB addition since it is the commonly used grain refiner.

Lamellar
Structure



Transitional
Lamellar
Structure



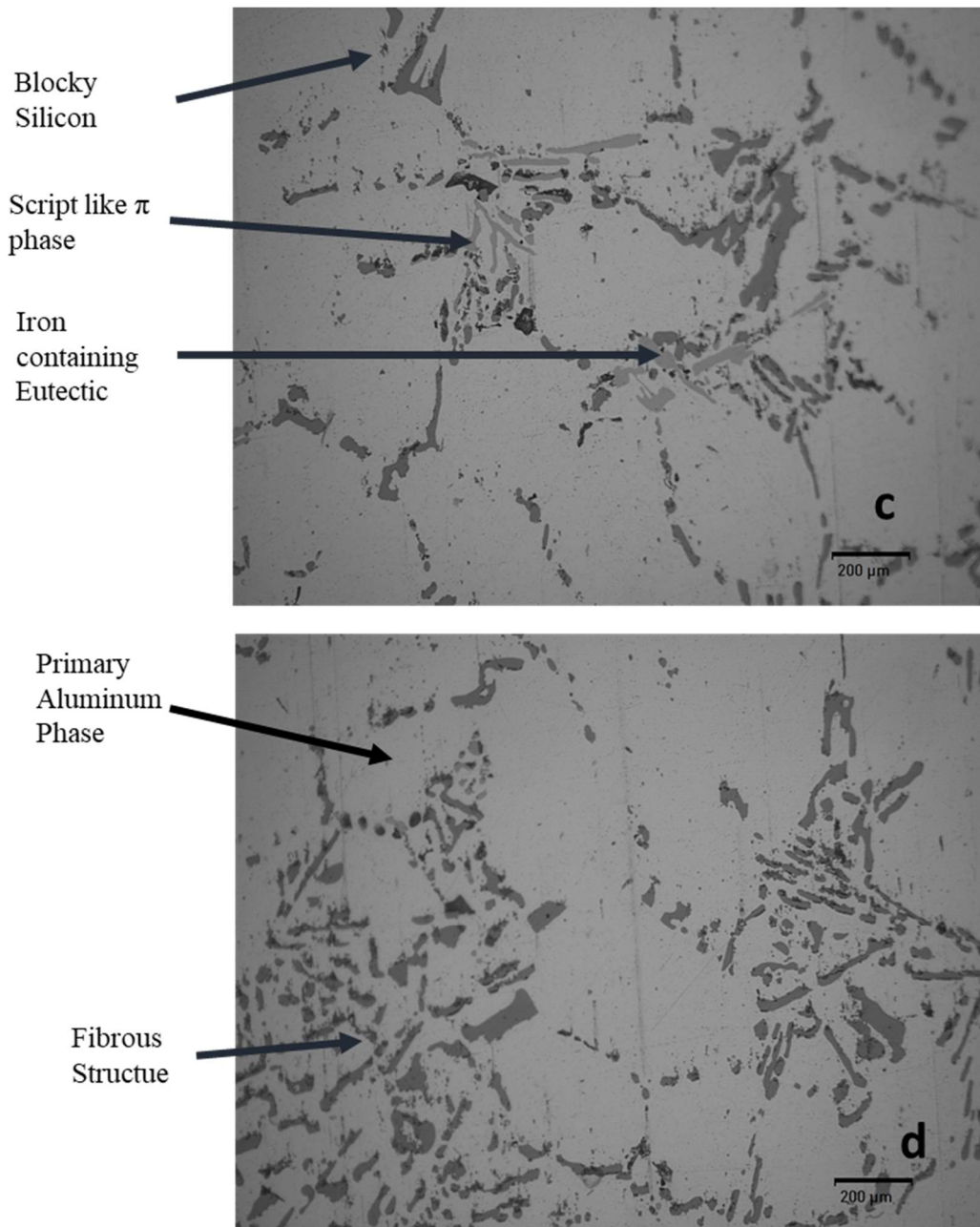


Figure 4.13 Optical microscope images of transition lamellar/fibrous eutectic morphology after heat treatment of Alloy I etched with Keller's reagent (a & b: 200x magnification; c: 500x magnification; d:1000x magnification)

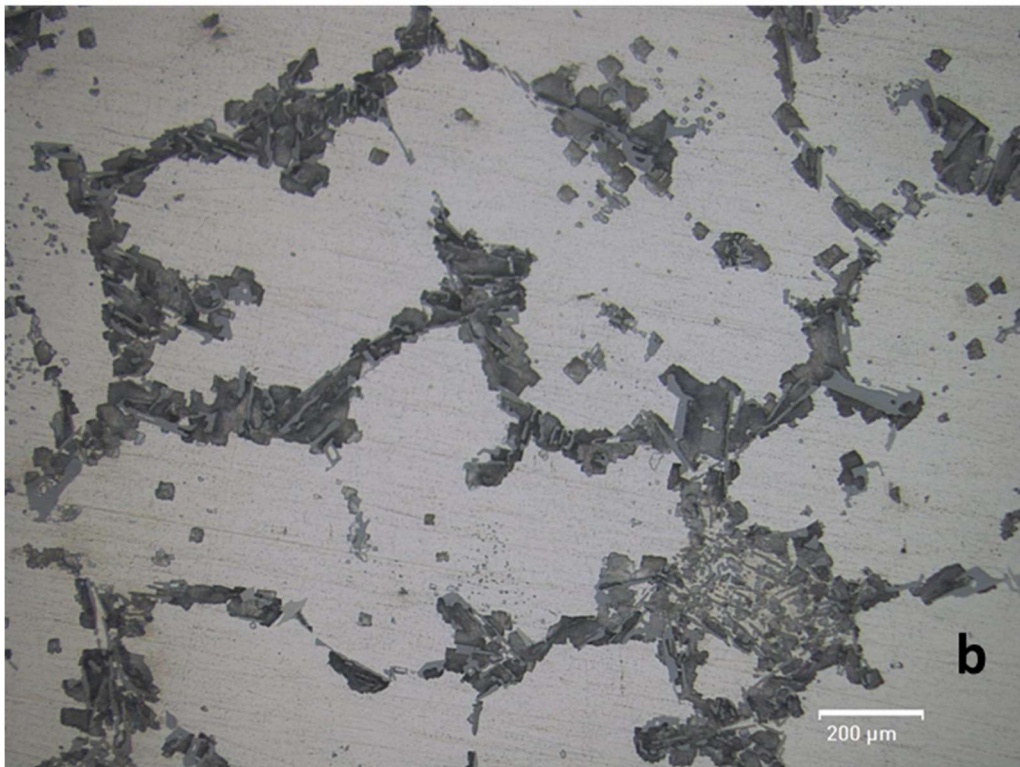
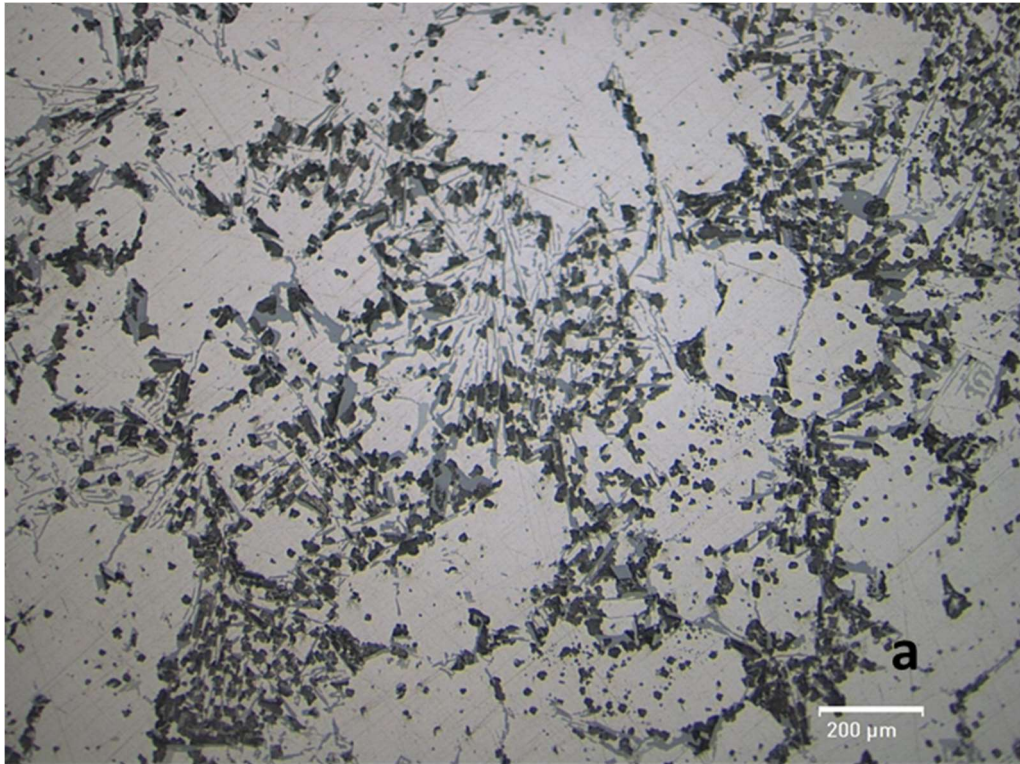


Figure 4.14 Transition Lamellar/Fibrous eutectic morphology of as-cast Alloy III etched with Tucker's reagent (a: 200x magnification; b: 500x magnification)

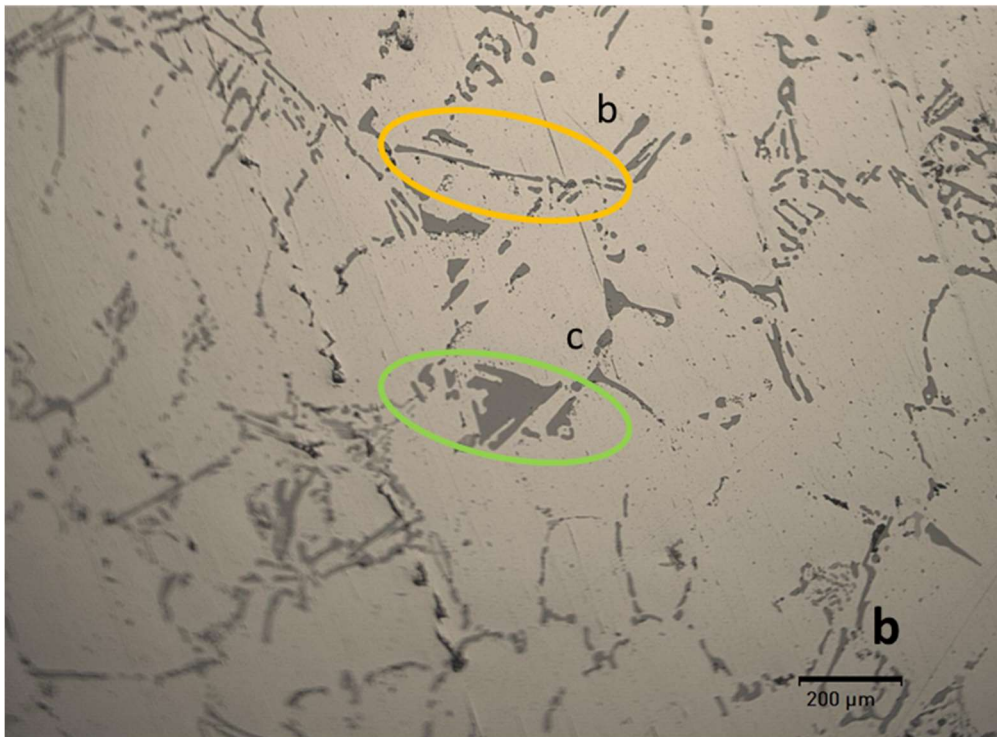
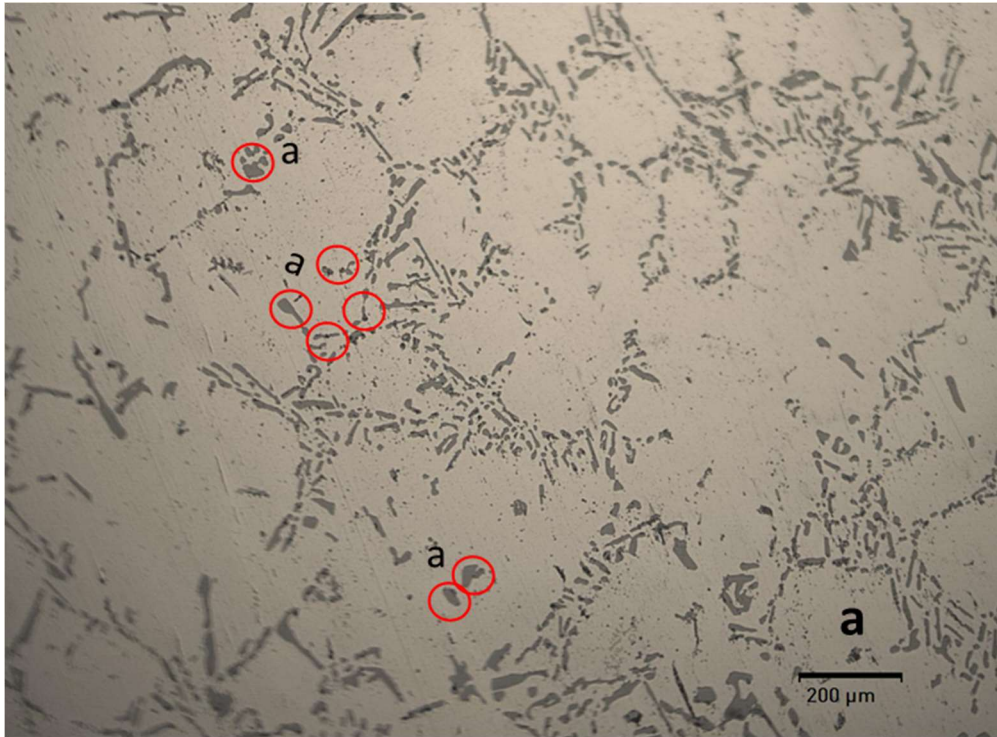
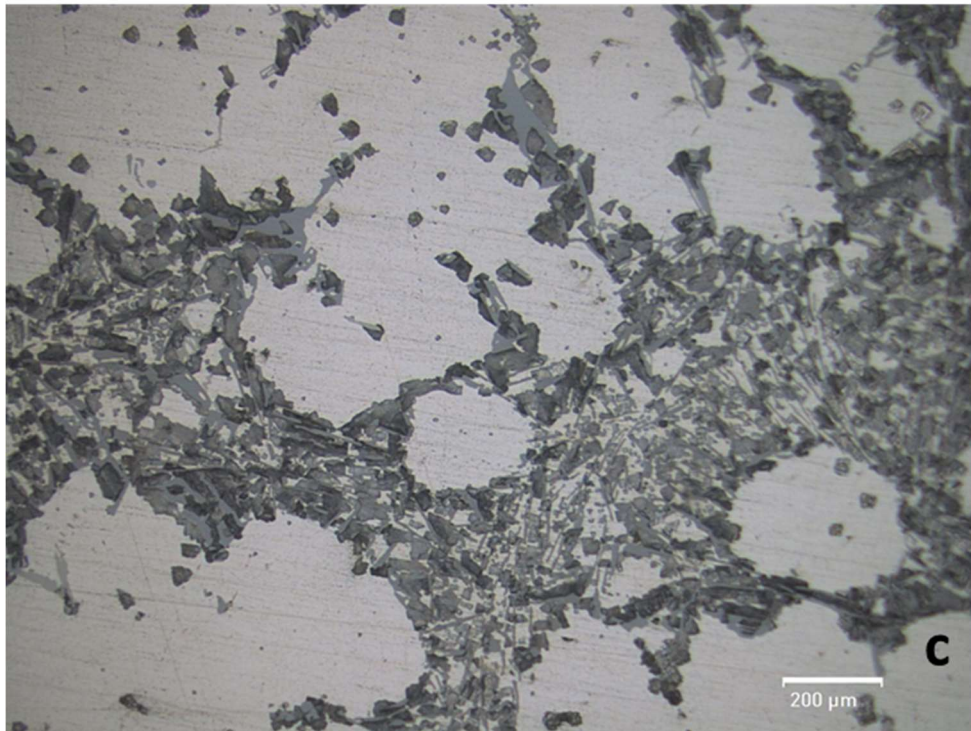
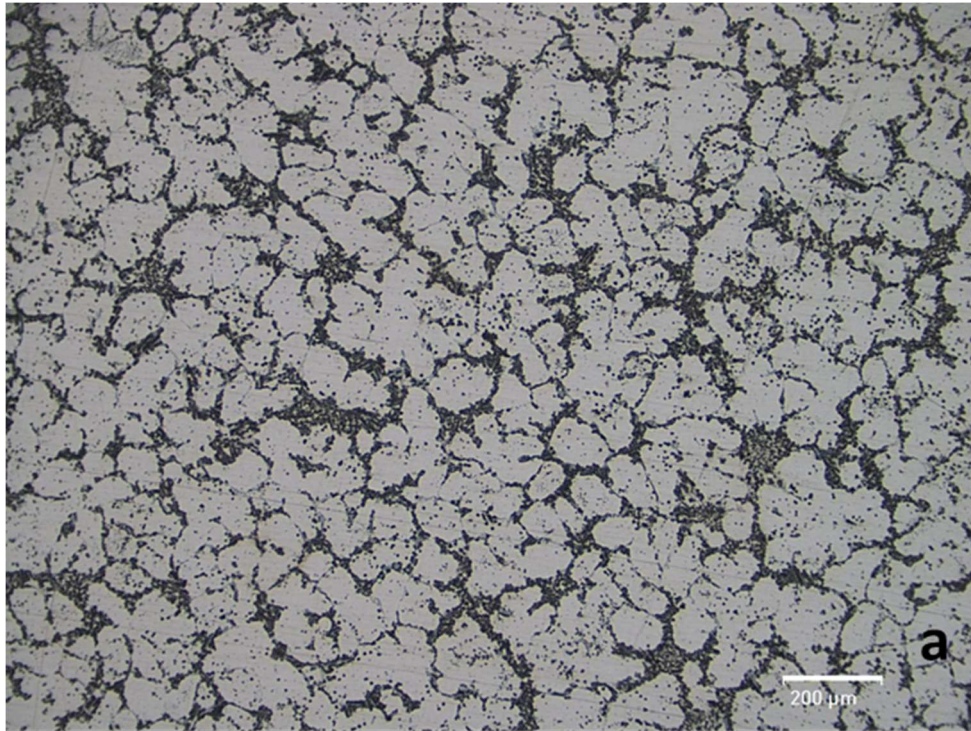


Figure 4.15 Optical microscopes images of Alloy III after heat treatment etched with Keller's reagent (a: Fine fibrous eutectics with 500x magnification; b: Large silicon and lamellar eutectics with 500x magnification)

Figure 4.15 exhibits evenly distributed eutectics with a more fibrous eutectic structure as a result of heat treatment. Red circles precipitates identified as “a” letter in Figure 4.15 indicates the fibrous eutectics while letter “b” represents lamellar structure, and green circled areas described as “c” letter show the blocky phase silicon.

It can be stated that solutioning treatment provides the precipitates non-uniformly distributed to be dissolved via matrix. So, more homogeneous grain structure is observed.

In addition, aging treatment followed by solutioning in a 45 min to avoid natural aging, is performed in a furnace to maintain T6 heat treatment condition. Figure 4.16 compares the optical microscope images of as-cast and heat-treated conditions of Alloy III. It revealed fine fibrous eutectic morphology. It can be stated that transitional lamellar structure transformed to the fibrous eutectic structure.



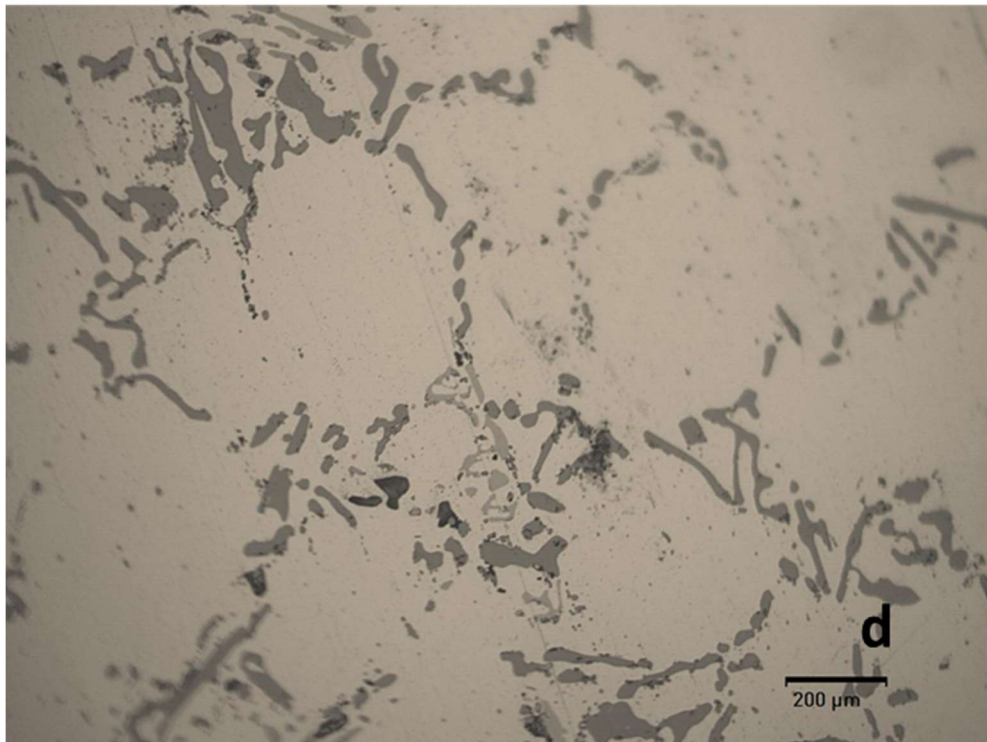
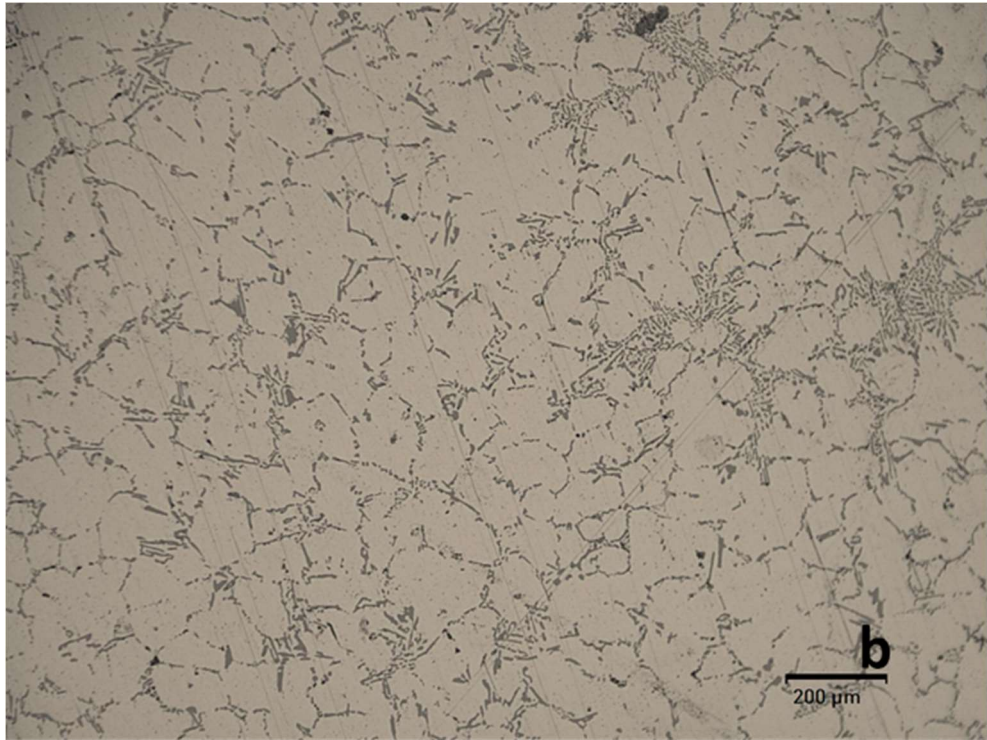


Figure 4.16 Optical microscope images of Alloy III in as-cast and as-heat-treated conditions (a and c:200x and 500x, respectively, magnifications of as-cast Alloy III; b and d: 200x and 500x, respectively, magnifications of heat-treated Alloy III)

Moreover, scanning electron microscope images are also observed to examine the eutectic morphology in more detail. Modified eutectics including fine and large silicon precipitates are shown in Figure 4.17.

Apart from the microstructural images, chemical analysis was also performed via electron microscope by using EDX detector. Observed peaks belonging to the elements inside the region shown in Figure 4.18-a are given in Figure 4.18-b. As it is expected, mainly aluminum peaks are seen together with, magnesium, silicon, titanium and silver. Al, Mg and Si elements are observed together with minor amount of Ti. The Ag peaks are caused from the specimen preparation. In order not to charge the bakalite, as explained in 3.8.3, silver is coated to the contact surfaces of the specimen with the machine setup.

Figure 4.18-c and d identify the point analysis for Mg_2Si phase formed on the eutectic structure. Again, mainly aluminum peaks together with, magnesium, silicon, titanium and silver are observed. The only difference is Fe and Ni elements. The source of them is the raw material, A357, they are included as impurity level. However, they may also come from the casting process, such as improper ladle, stirring and furnace equipment usage. Iron is the detrimental element for Al-Si castings, according to the researches explained in 2.2.2. They generally react with Al-Si elements and forms α and β phases. Iron contained eutectics generally seen in optical microscope as light grey while iron free eutectic Si appears as dark grey color as shown in Figure 4.13.

The reasons why iron peaks are observed in the Mg_2Si precipitate are that;

- Π phase including Mg-Si-Al-Fe. However, it is generally formed as script like.
- Iron may come from the remaining areas including iron contained eutectics.

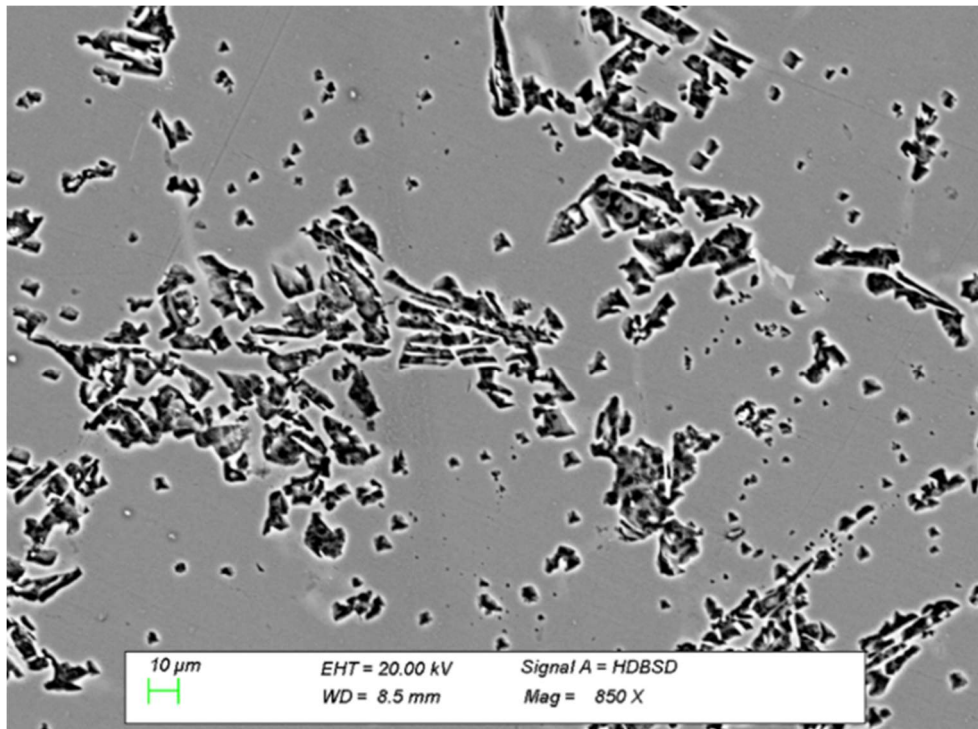
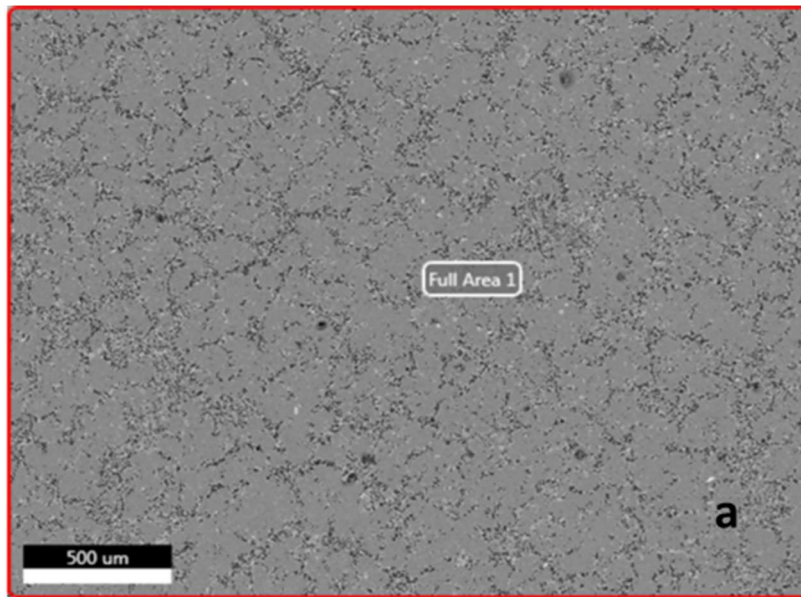
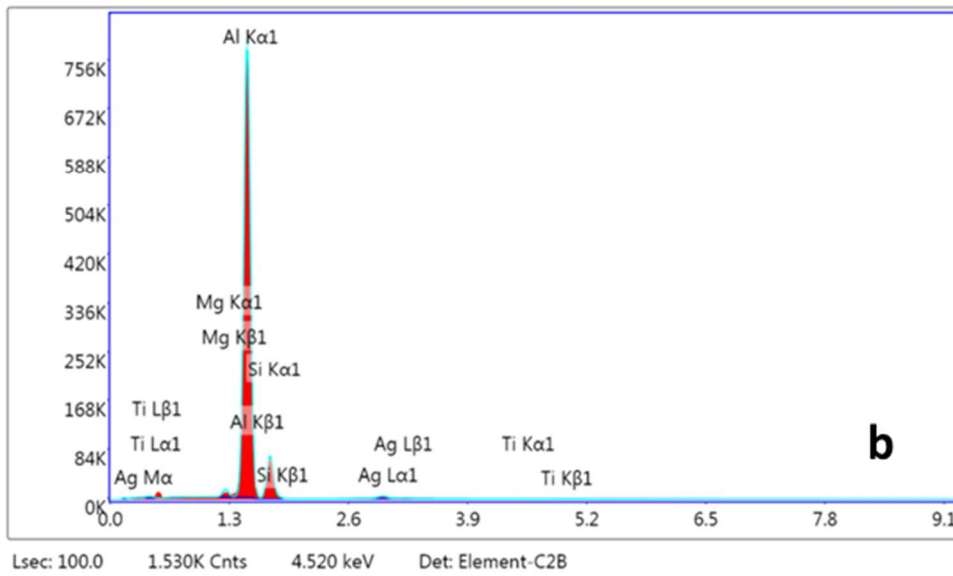
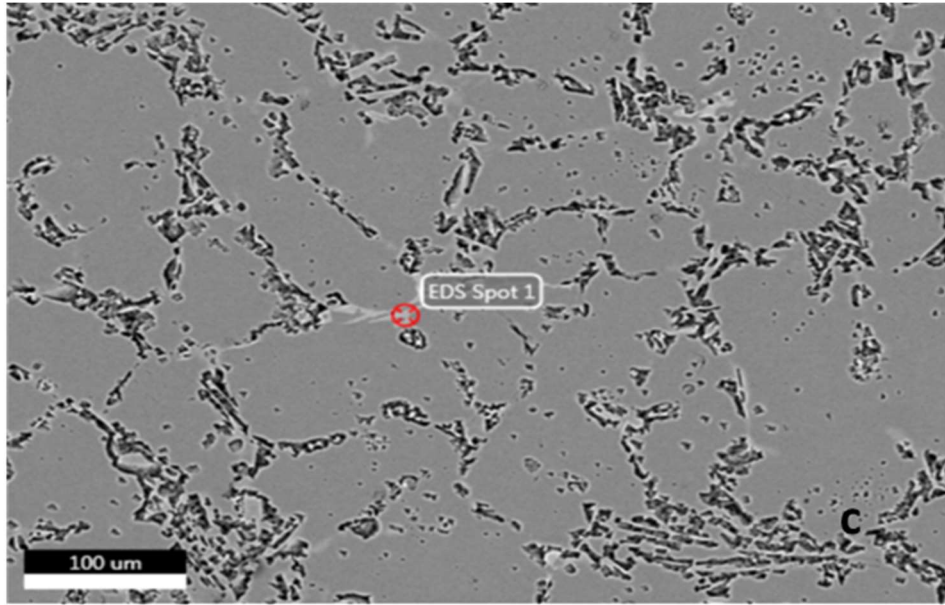


Figure 4.17 Scanning electron microscope images of as-cast Alloy III



Full Area 1 - Det 1





EDS Spot 1 - Det 1

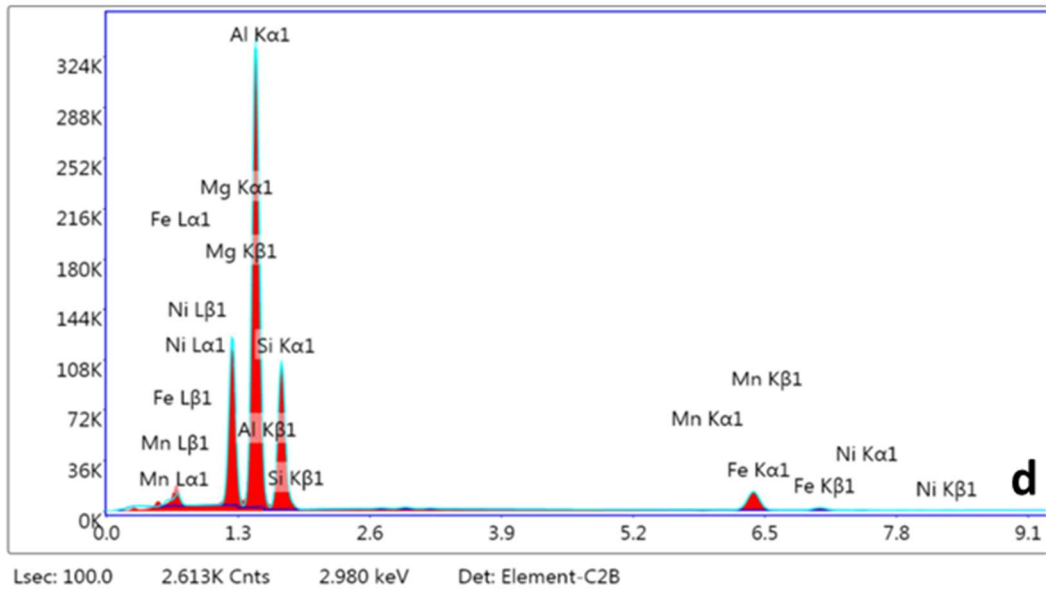
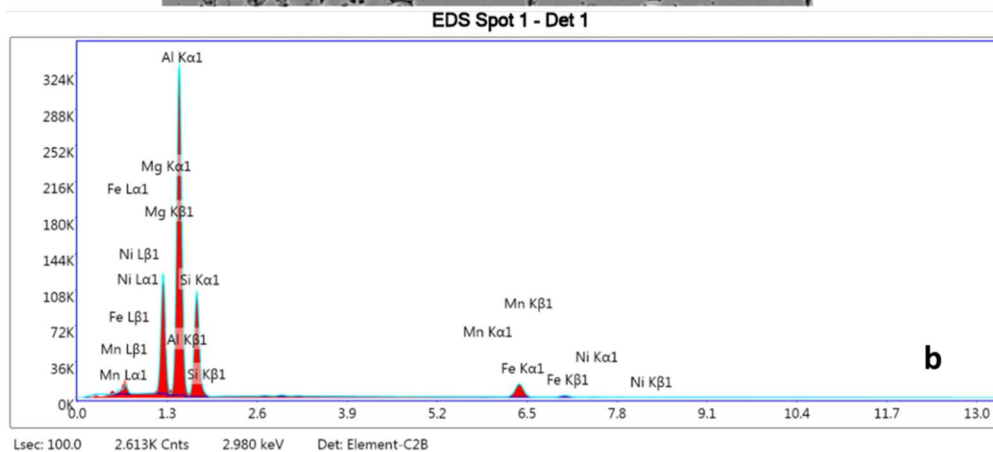
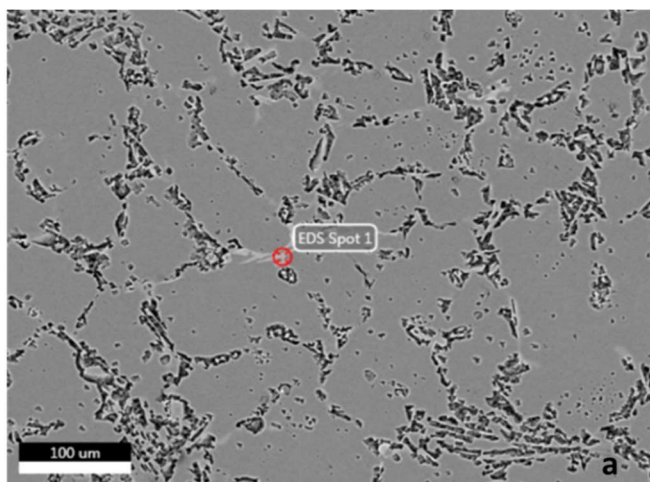


Figure 4.18 Energy Dispersive Spectroscopy examination of as-cast Alloy III (a: SEM images of general area; b: EDS analysis results of general area; c: Mg₂Si included general area; d: Point EDS analysis of Mg₂Si)

In order to examine the iron element precipitated together with Al – Si, back scattered detector of Scanning Electron Microscope was used. Since this detector allows to differentiate the atomic weights of each element resulting color difference, iron based eutectic phase can be differentiated in white regions. Figure 4.19 – c

identifies the white areas which are surrounded by dashed lines representing the iron based α and/or β phases. Figure 4.19 -b shows the elemental analysis of the point indicated in Figure 4.19-a. The analysis verifies that the precipitate includes Mg and Si elements.

Moreover, point analysis location and EDS results are given in Figure 4.19- a and Figure 4.19- b, respectively.



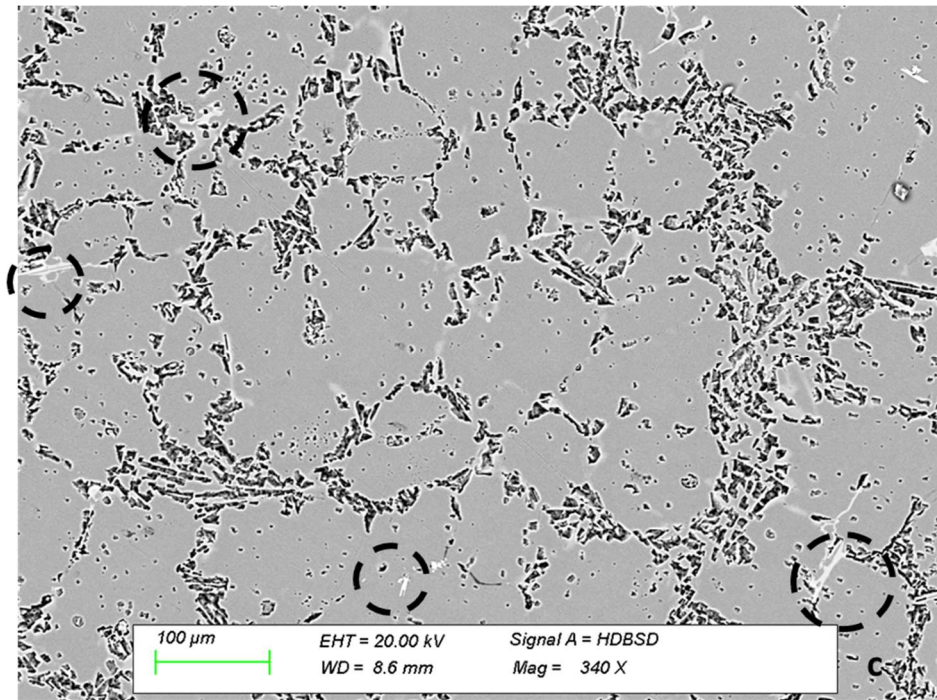


Figure 4.19 Energy Dispersive Spectroscopy and High Density Back Scattered examination of as-cast Alloy III (a: SEM images for iron-contained eutectic Si; b: Point analysis of the phase iron-contained eutectic phase; c: High Density Back Scattered Images of iron contained eutectic phase.

Final examination about Alloy III is related with Mg_2Si in Chinese script which forms during solidification. Apart from the fine spherical and rounded Mg_2Si precipitated after heat treatment, Mg_2Si in Chinese script morphology was observed in the microstructure after T6 heat treatment. Figure 4.20 shows the Mg_2Si in Chinese script form. They formed during solidification as explained in Table 4.6.

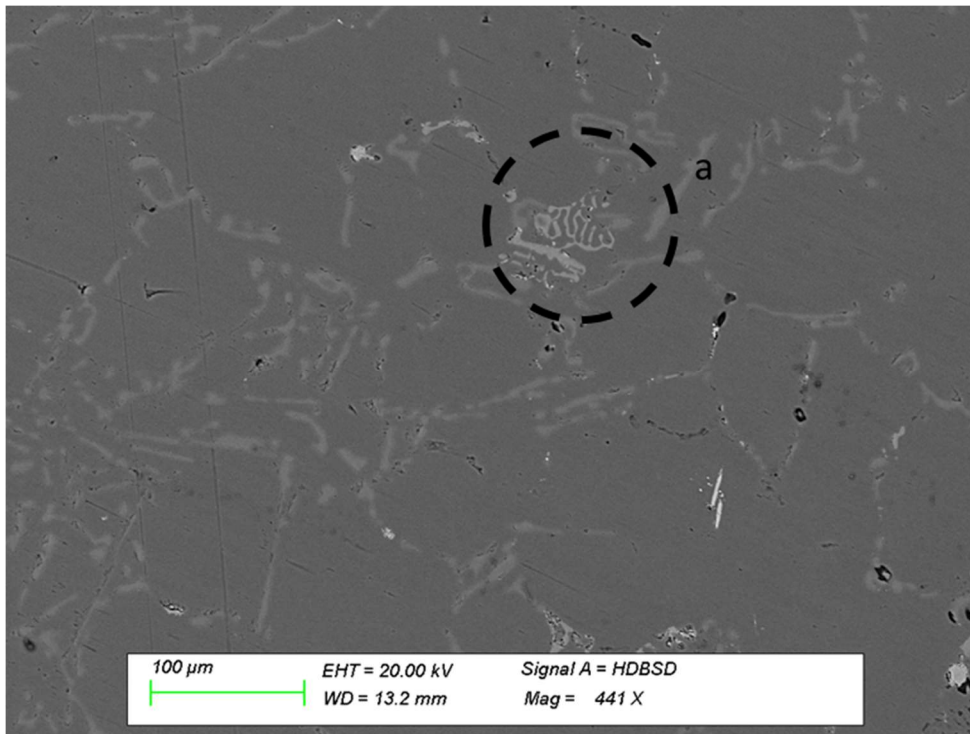


Figure 4.20 Scanning electron microscope images of heat-treated Alloy III

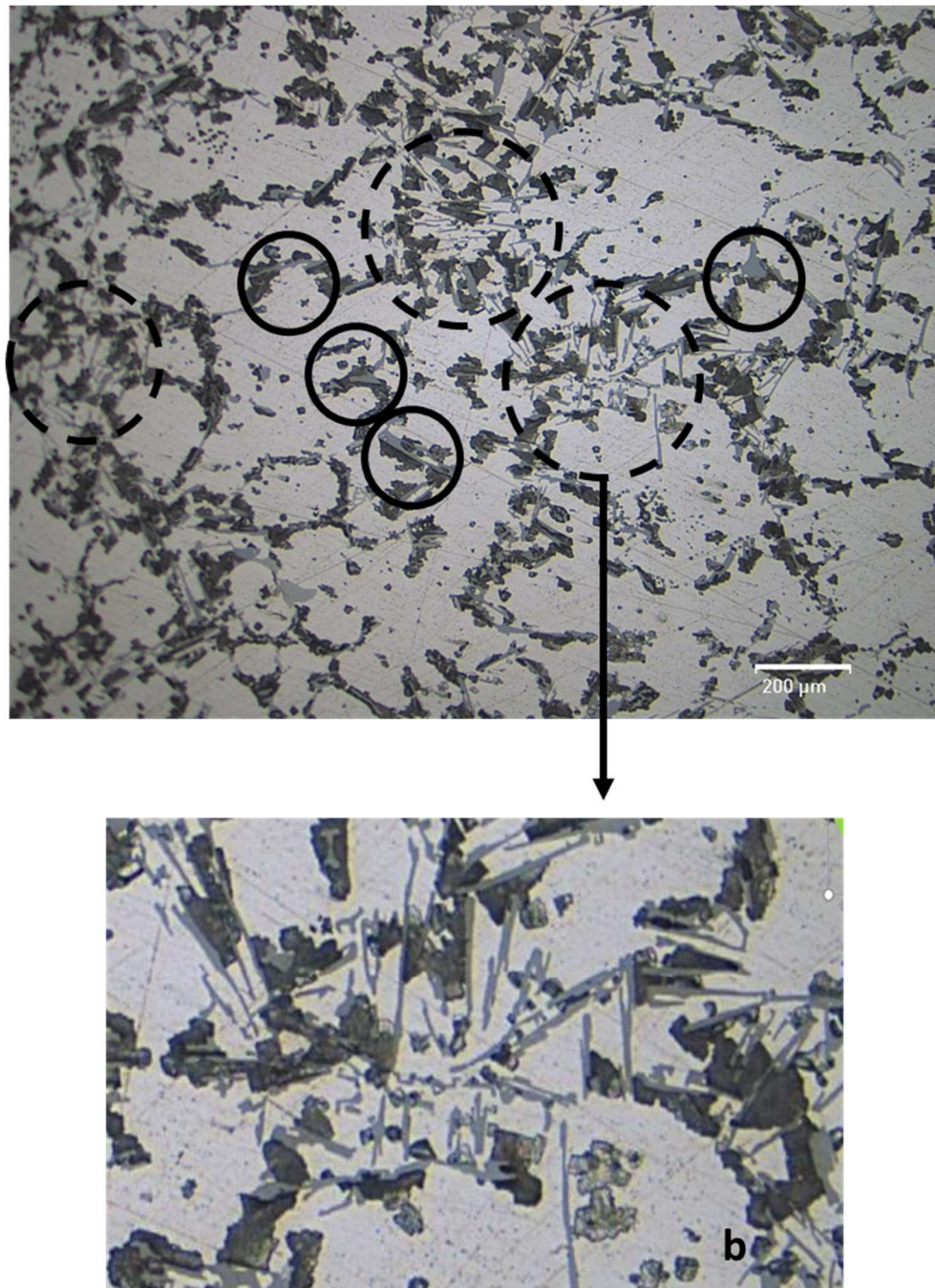


Figure 4.21 Optical microscope images with 500x magnification of acicular/lamellar eutectic morphology of as-cast Alloy IV etched with Tucker's reagent. (a: 500x magnification; b: Zoomed in acicular eutectic structure)

According to the Figure 4.21, acicular eutectic morphology is seen together with modified fibrous structure. It can be stated that iron rich eutectics, i.e. α and/or β , are

in the acicular form while dark grey eutectics belonging to eutectic Al-Si are in the fibrous structure. In the same figure, dashed surrounding areas show the iron contained eutectic silicon while circled areas indicate eutectic silicon. Figure 4.21 – b indicates the acicular eutectic structure defined in dashed line surrounding area with more magnification. Also, solid line circled areas belong to the blocky form of Mg_2Si .

Since iron is included as an impurity, it reacts with eutectic Al – Si and forms script like π phase, detrimental for mechanical properties. Figure 4.22 shows the π phase formed in heat treated Alloy IV and the image shown in Figure 4.22 – b is taken from Taylor's studies [7].

Moreover, solutioning heat treatment provided distribution of second phases evenly. Some of the eutectic structures changed from acicular to transitional lamellar as indicated in Figure 4.23. Fine eutectics are seen together with lamellar structure.

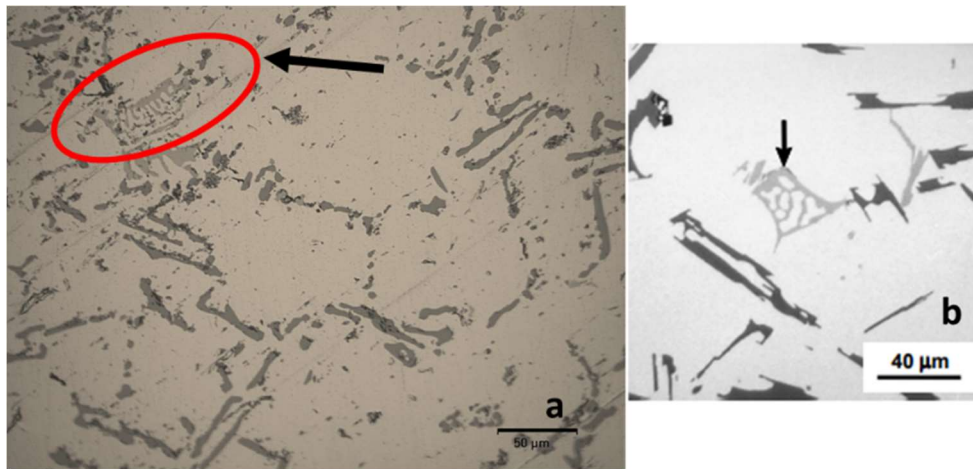


Figure 4.22 Optical microscope images for π phase. (a: 1000x magnification of heat-treated Alloy IV; b: script like π phase [7])

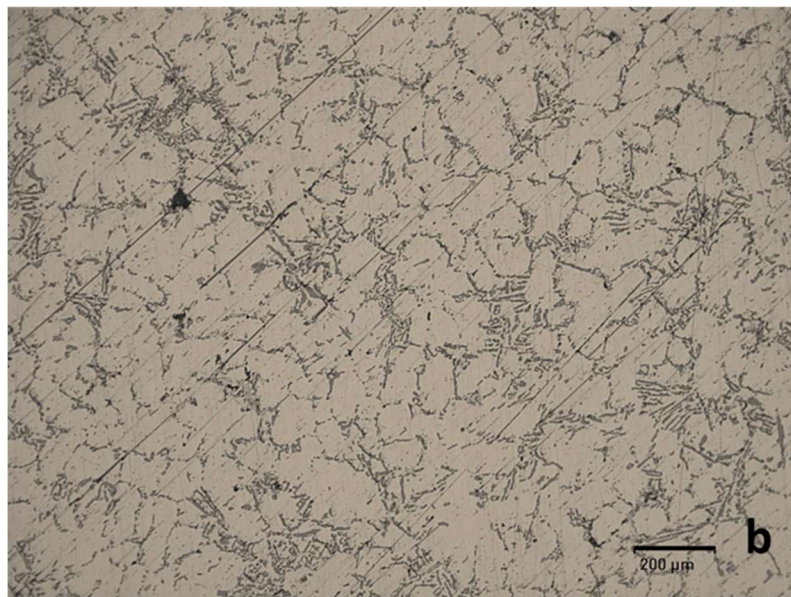
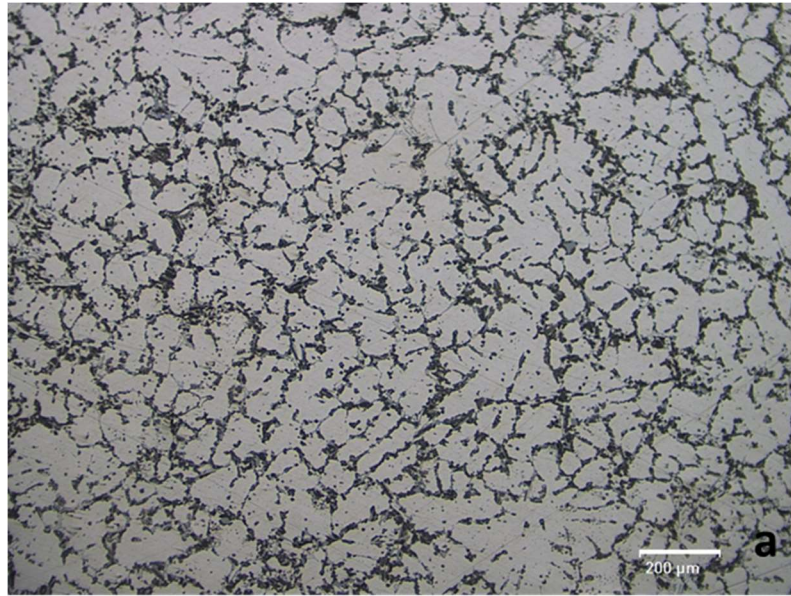


Figure 4.23 Optical microscope images. (a: As-Cast Alloy IV 200x magnification:
Heat Treated Alloy IV 200x magnification)

When Alloy II is examined, which was cast with Al-Nb-B addition, optical and electron microscope images are shown in following figures.

Figure 4.24 shows that number of modified eutectics including blocky silicon phase and fine eutectic silicon are very high when compared with previous alloys. Actually, (Nowak, 2011) stated in his doctoral thesis that is not only refinement of primary

aluminum phase, but also eutectic refinement is provided by Nb-B addition. This is actually supported in this thesis. Figure 4.24 explains the modification of eutectic phases.

(Sigworth, 2008) stated that breakage of eutectic phase is an indicative of eutectic modification.

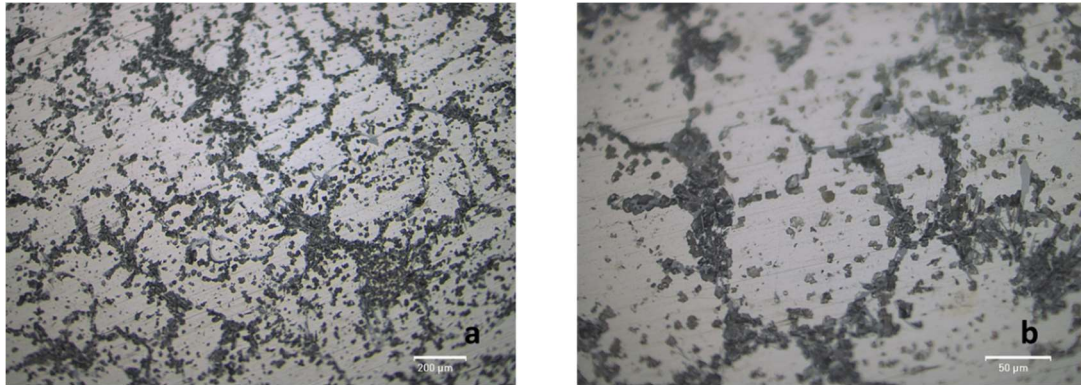
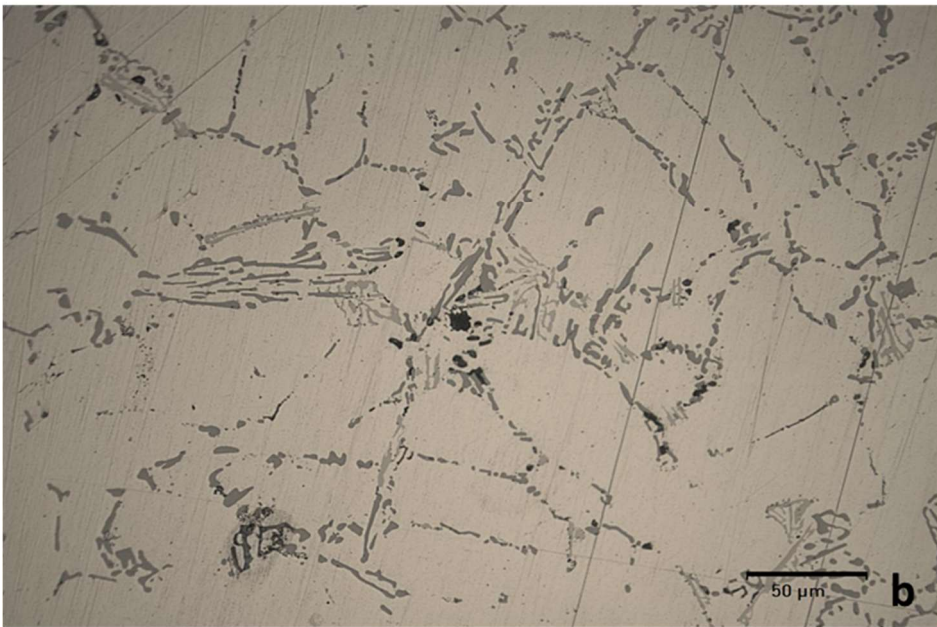
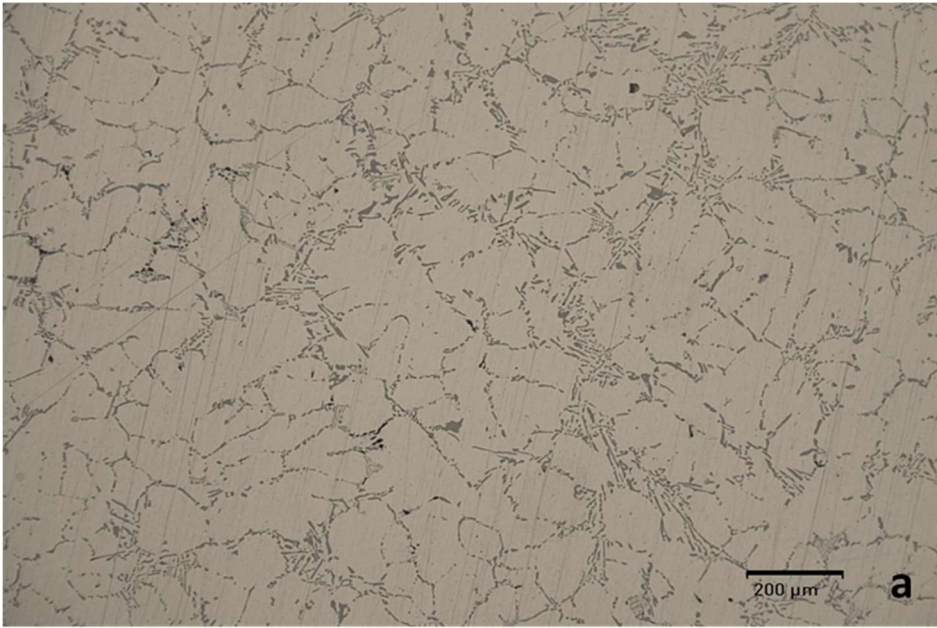


Figure 4.24 Optical microscope images of as-cast Alloy II. (a: 500x magnification; b:1000x magnification)

When the microstructural images are compared with Alloy I, Alloy III and Alloy IV, modified eutectics are seen. The results can also be supported by thermal analysis. Table 4.6 shows that eutectic nucleation start temperature is decreased for Alloy II to approximately 5 °C, and eutectic undercooling is increased slightly. Also, after heat treatment, second phases distributed more evenly. Figure 4.25 indicates the eutectic structure in different magnifications. When 500X and 1000X magnifications are examined, it is seen that fine fibrous eutectics are existing.



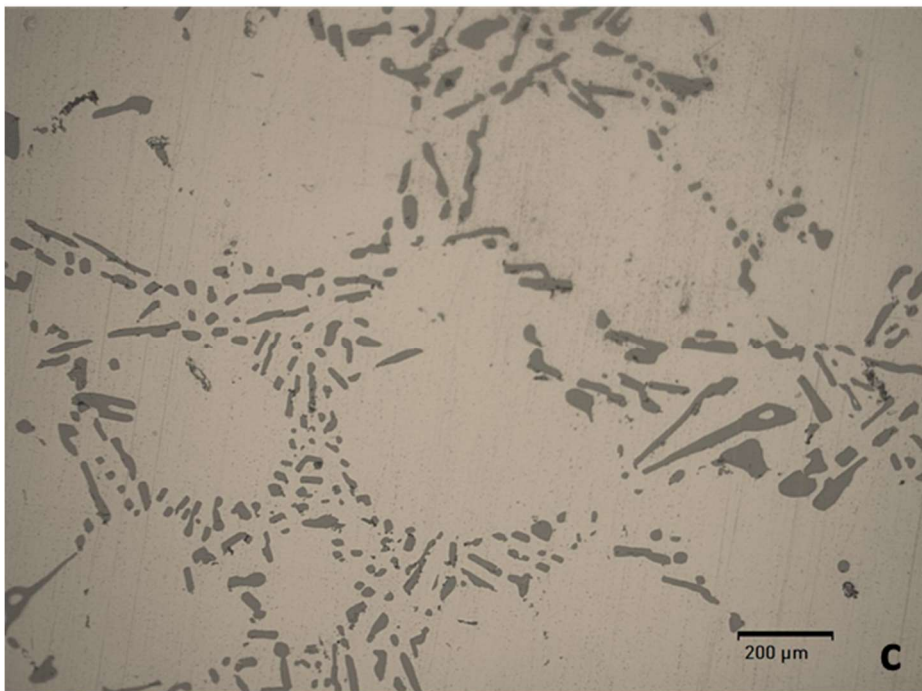
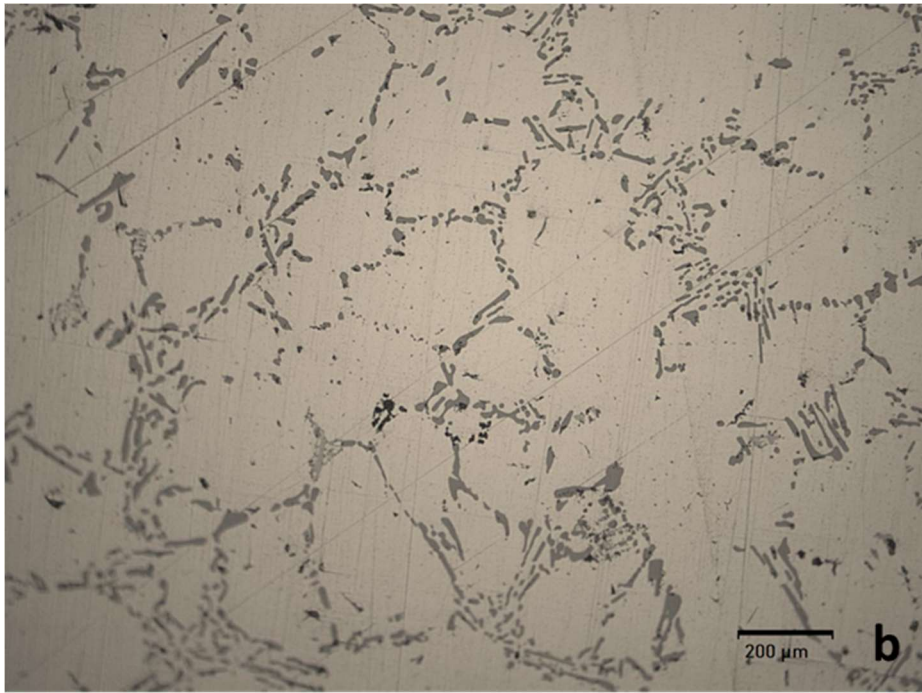
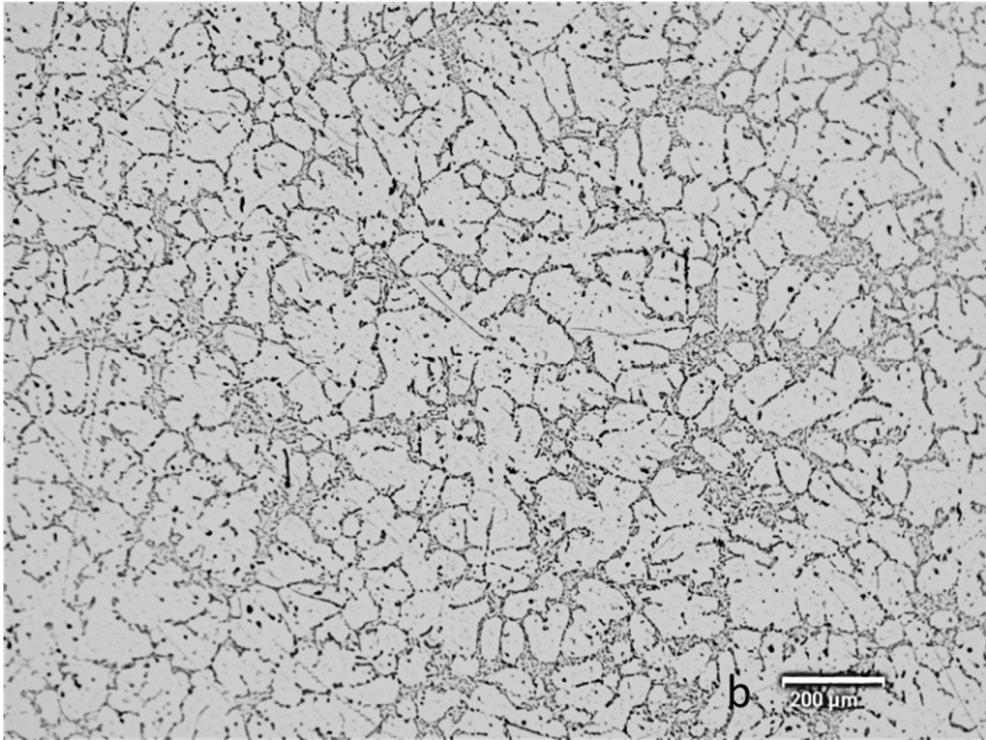


Figure 4.25 Optical microscope images of heat-treated Alloy II. (a:200X; b:500X; c:1000X magnifications)

Figure 4.26 compares the as-cast alloy types to clarify the difference. Alloy I and IV have mostly acicular and lamellar type of eutectic structures while Alloy II and III have lamellar and modified structures. Alloy II has the mostly modified structure. Fibrous silicon can be detected. However, eutectic phases are distributed randomly which are positioned at some localized areas. This can be caused from the casting condition. Nevertheless, as Figure 4.25 states even distribution of eutectics are clearly seen.

Also, cooling rate was investigated for Alloy II by using the mold different cross sections. The mold includes 4 different cross-sectional areas, 9 mm, 12 mm, 20 mm and 40 mm. As the thickness increases, that is cooling rate is decreased, eutectic structure changes from modified fibrous structure to transitional lamellar structure. Also, as the cooling rate increased number of iron-based eutectics increases. It can be seen in Figure 4.28.

Apart from the optical microscope examination, scanning electron examination was also performed to observe the eutectic phase and precipitates. As performed for Alloy III, back scattered detector provided to observe niobium precipitates in more detail. Since the density of niobium is very higher than aluminum, approximately 3 times of aluminum density, back scattered detector differentiates the niobium precipitates from the rest of the matrix.



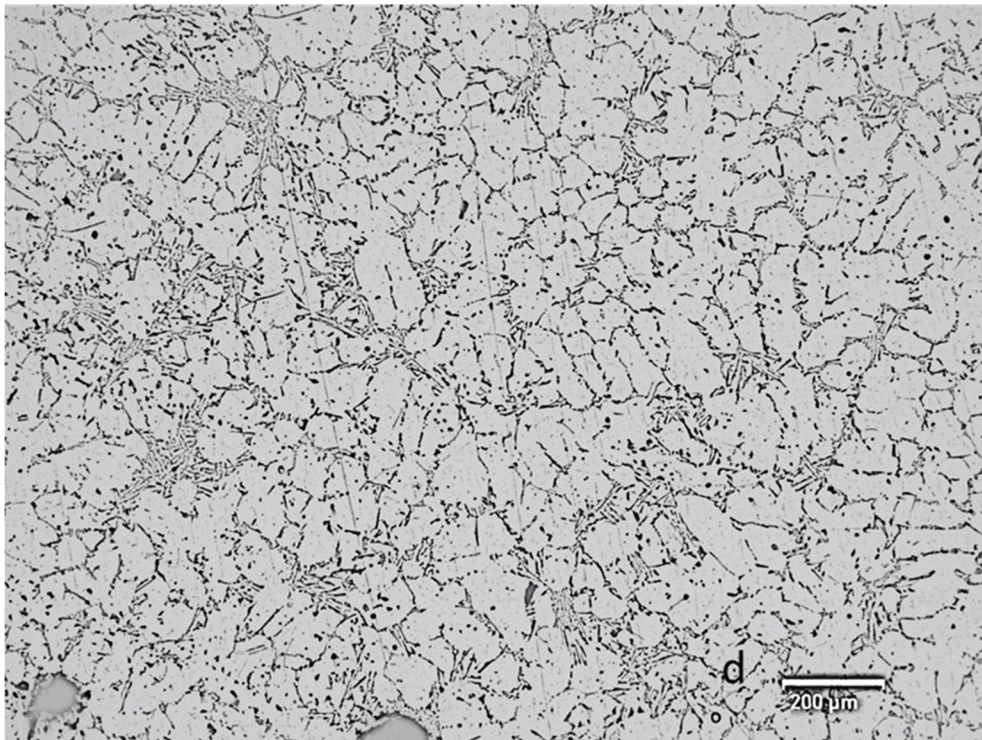
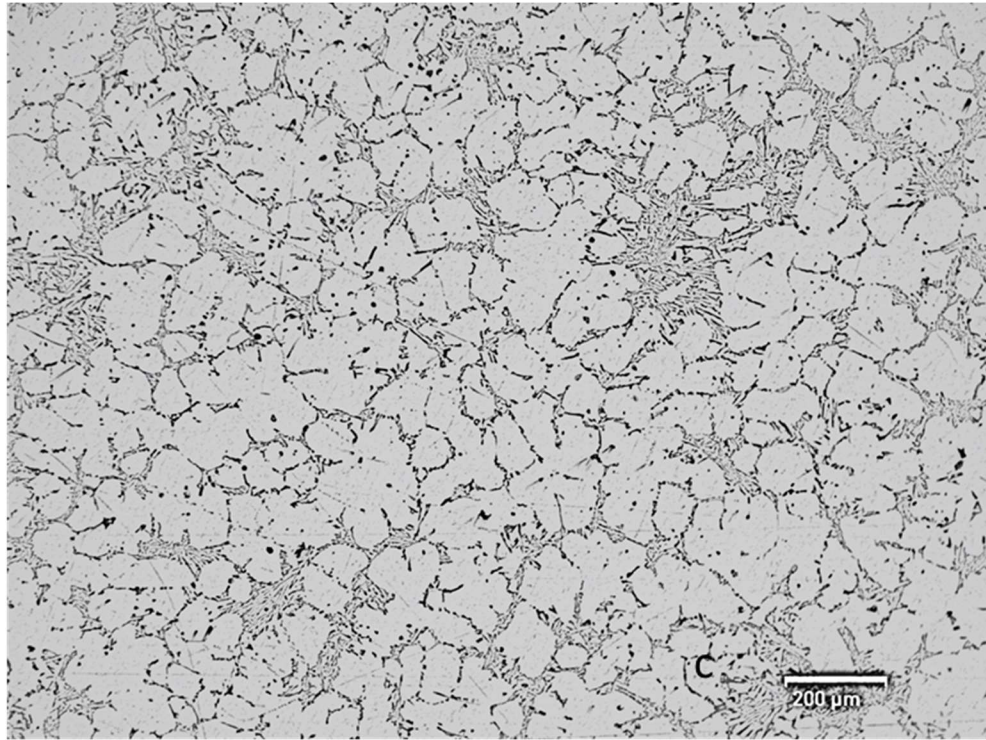
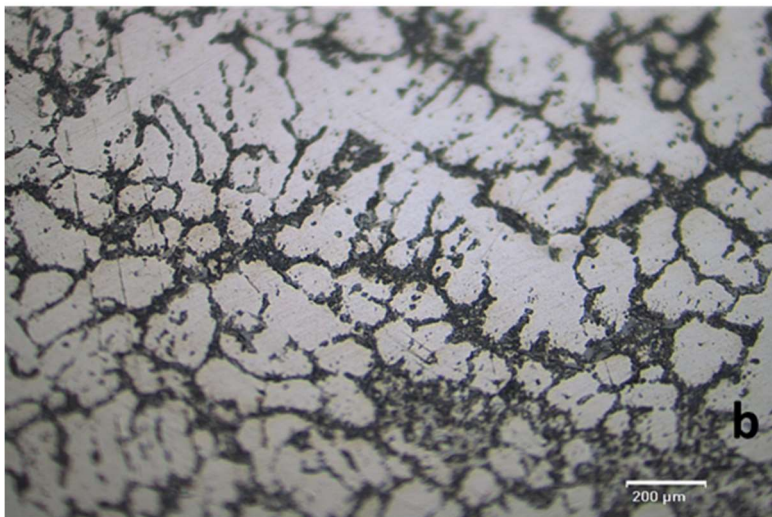
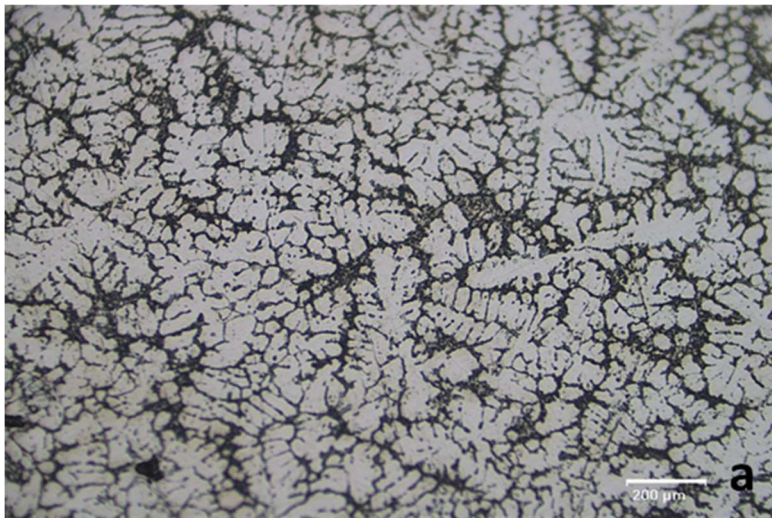
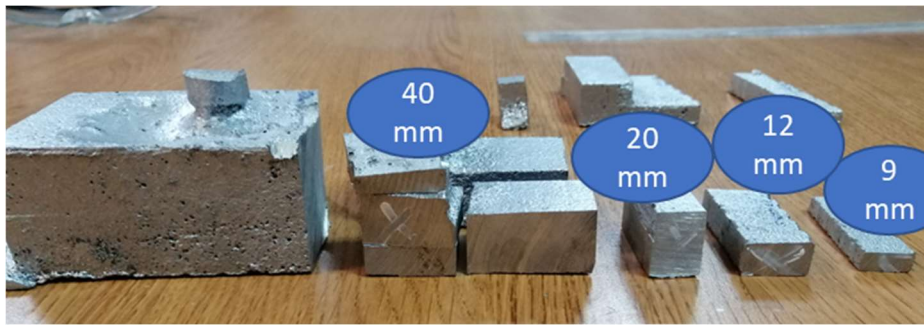
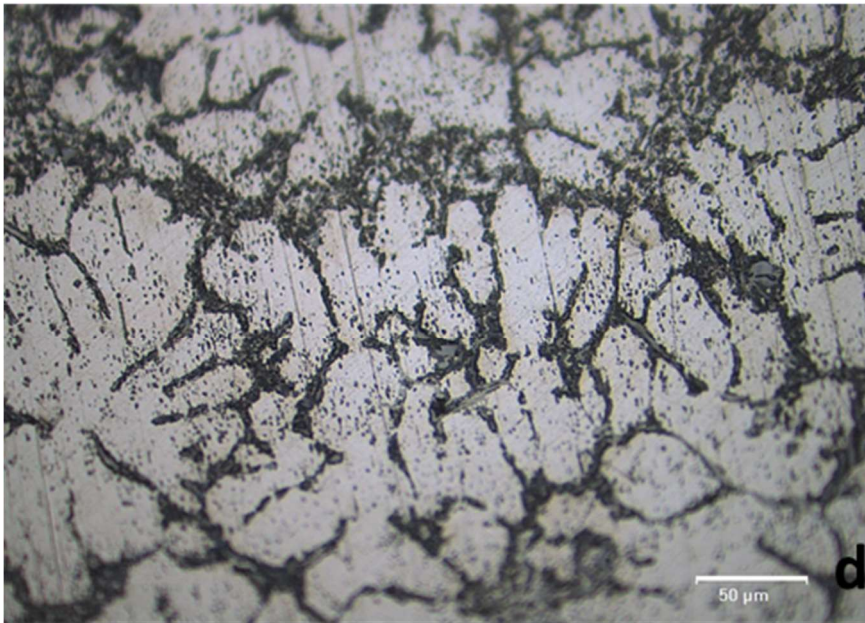
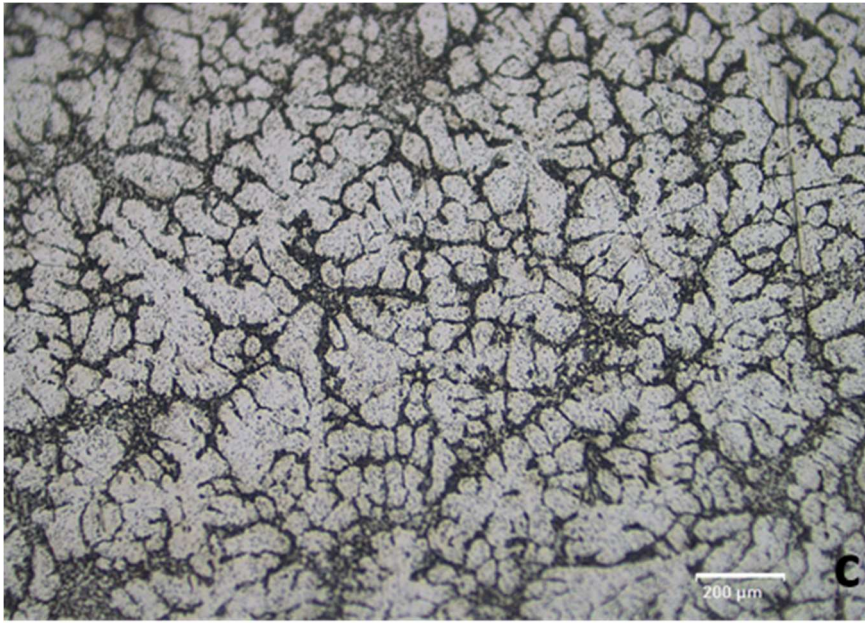
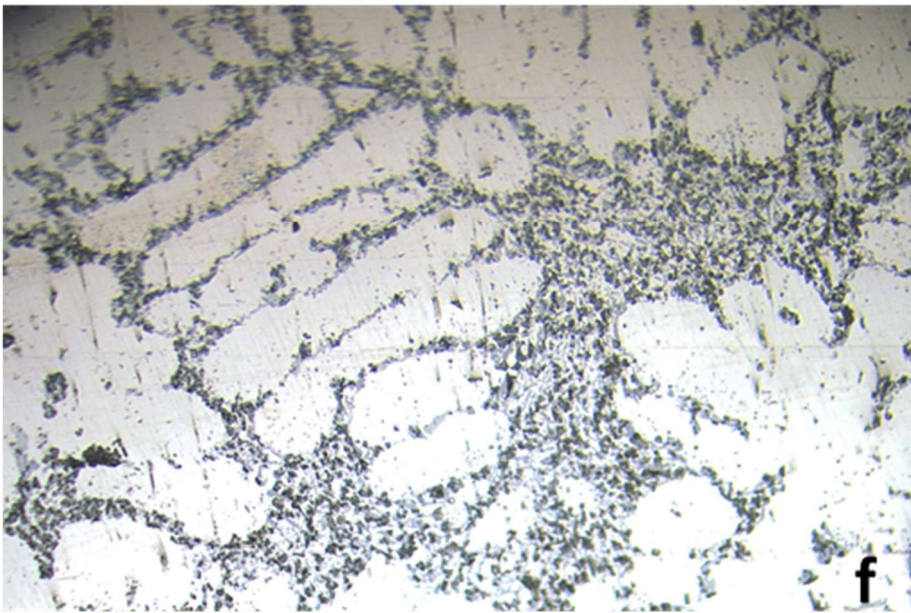
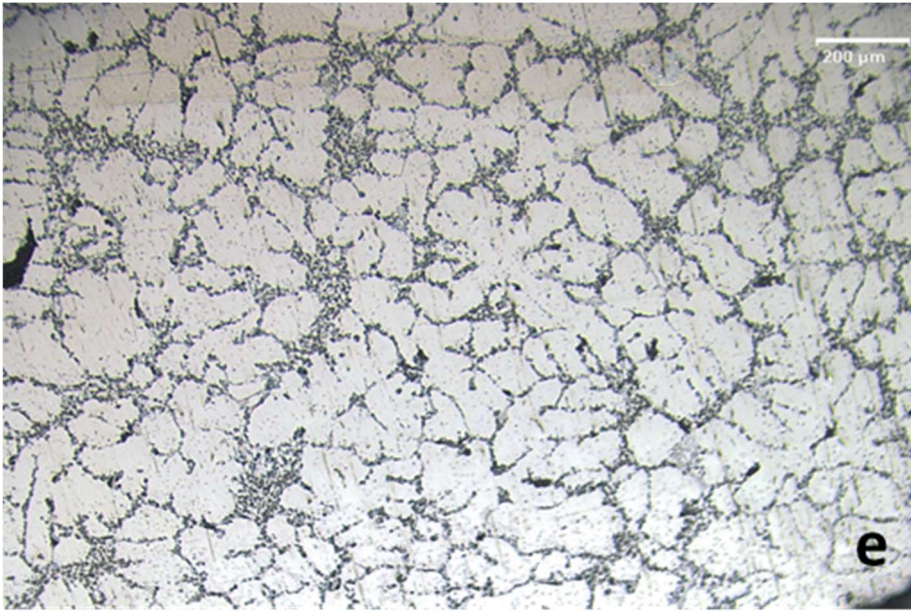


Figure 4.26 Optical microscope images of as-cast alloys at 200X magnification etched by Keller's reagent. (a: Alloy I; b: Alloy II; c: Alloy III; d: Alloy IV magnifications)







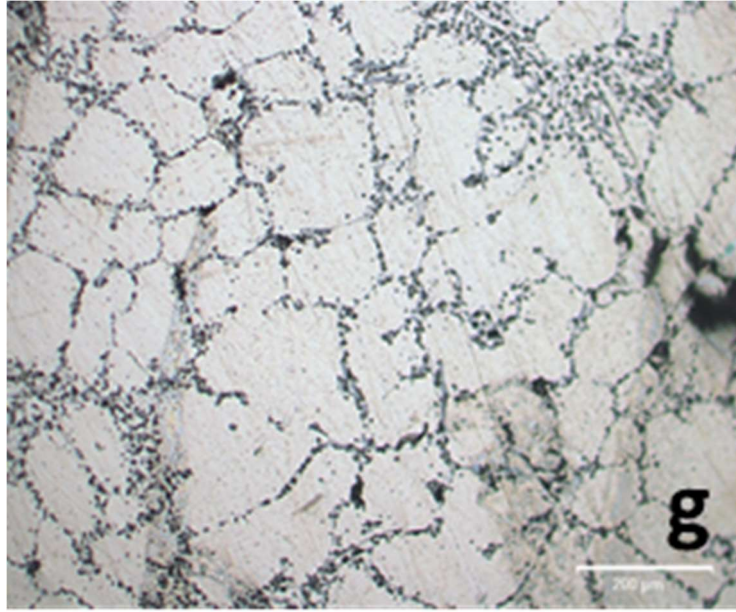


Figure 4.27 Optical microscope images of as-cast Alloy II for different cross-sections. (a:9 mm thickness – 200X magnification; b:9 mm thickness – 500X magnification; c:12 mm thickness – 200X magnification; d:12 mm thickness – 500X magnification; e:20 mm thickness – 200X magnification; f:20 mm thickness – 500X magnification; g:40 mm thickness – 200X magnification)

Figure 4.29 shows that thin, acicular form of niobium precipitates are formed. In the same figure, EDS analysis results are also shown. It includes mostly aluminum and niobium elements. However, its distribution is not homogeneous. It is localized at some points. When Figure 4.9 is reviewed, Al_3Nb phase is seen in the master alloy. However, alloy II did not exhibit any xrd peak for this phase. Since the localized points are very small amount, any peak cannot be detected via XRD measurement.

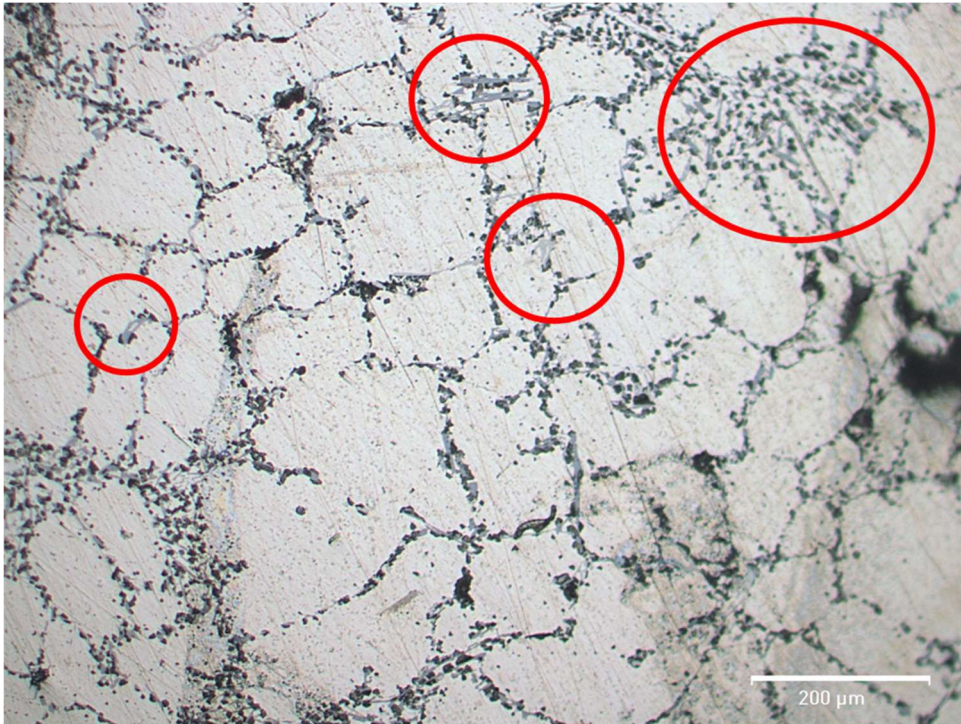


Figure 4.28 Optical microscope images of as-cast Alloy II having 40 mm cross section, 200X magnification

In addition, spectrometric analysis, ICP and XRF analyses reveal that Nb does not exhibit homogeneous distribution, which can be supported via electron microscope images. Figure 4.30 shows only one red circled area belonging to niobium – aluminum phase.

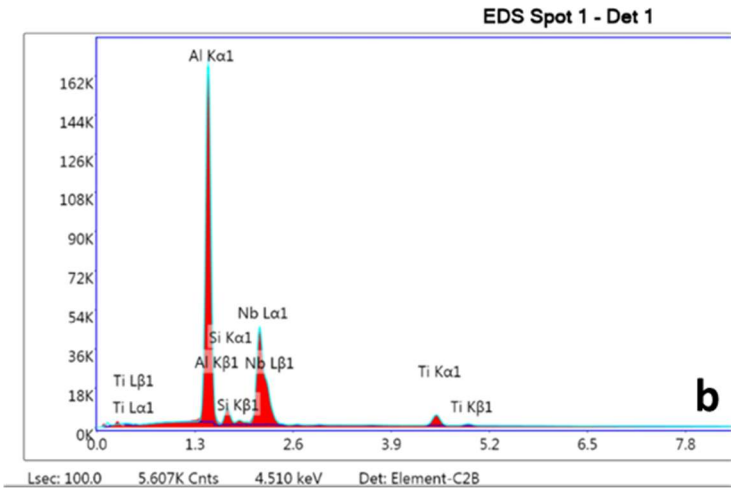
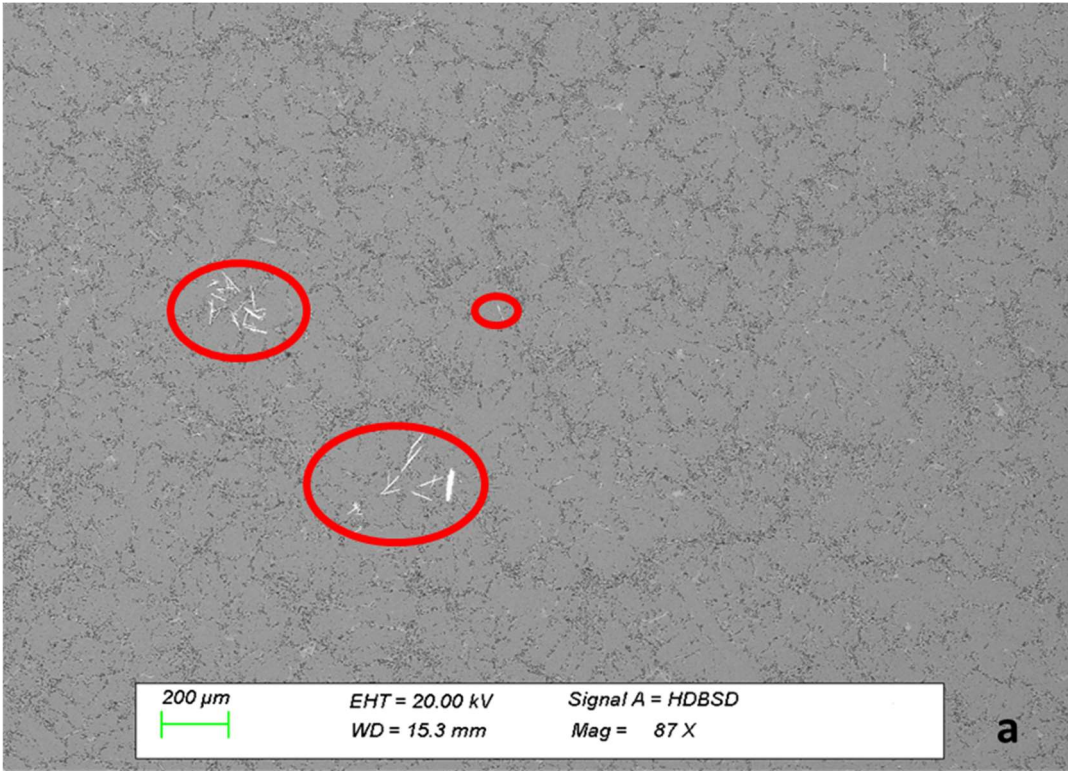


Figure 4.29 Scanning Electron Microscope images of as-cast Alloy II. (a:SEM images;b:EDS analysis of localized white precipitate)

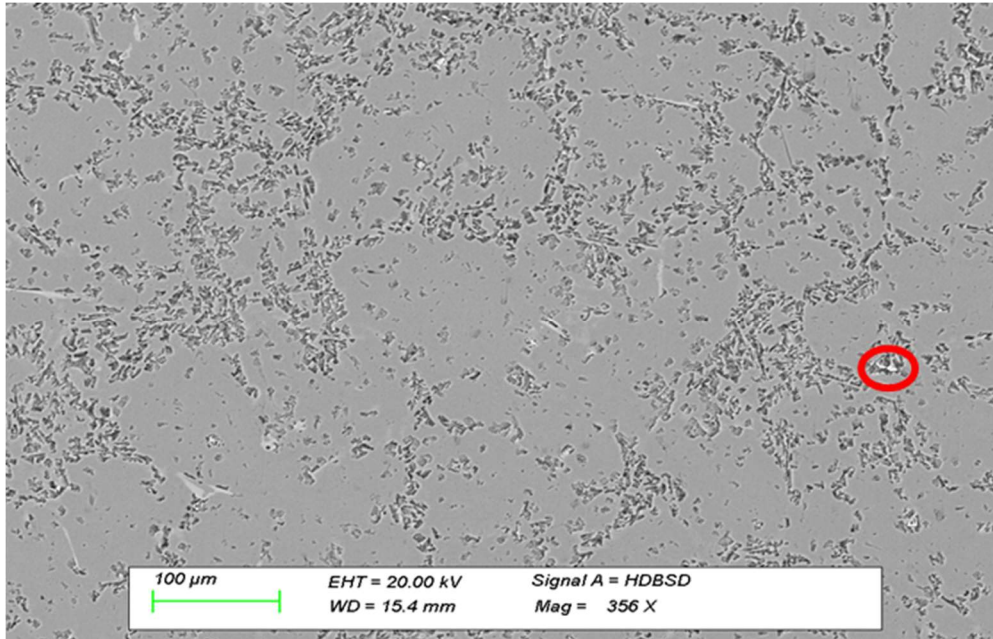
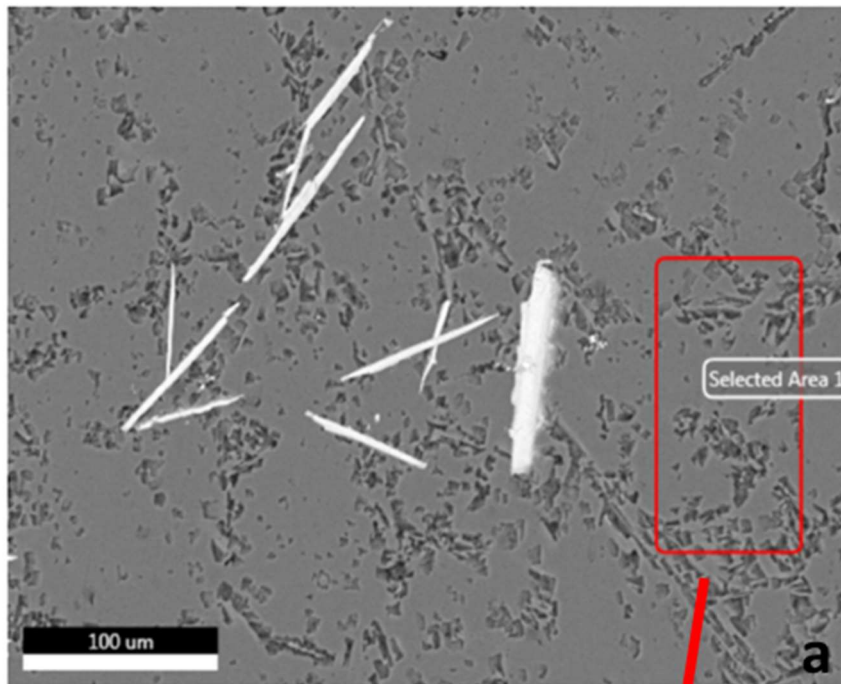


Figure 4.30 Scanning Electron Microscope images of as-cast Alloy II

Moreover Figure 4.31 shows that while acicular white precipitates indicate Nb and Al elements, selected areas in Figure 4.31 does not contain Nb element peaks.



Selected Area 1 - Det 1

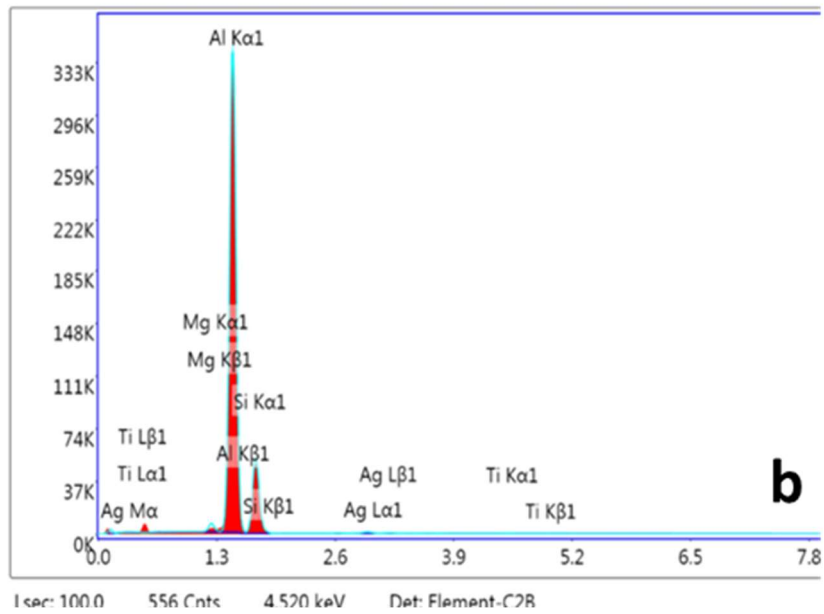
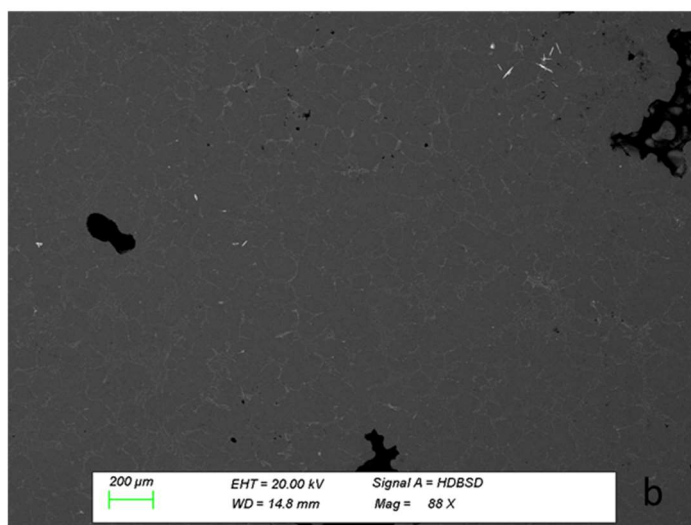
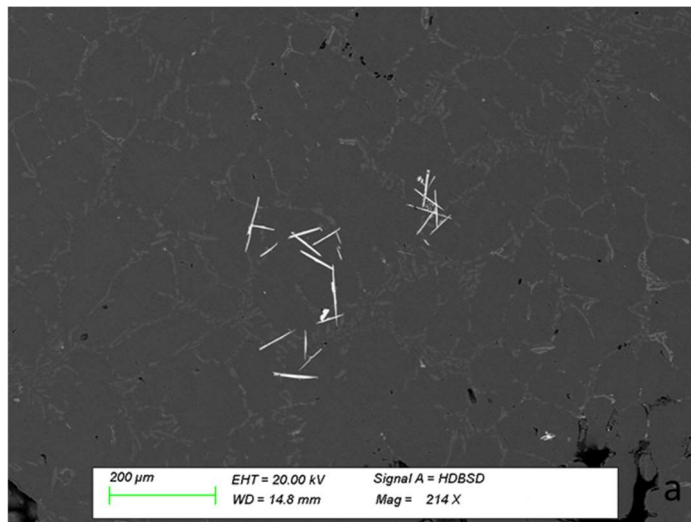


Figure 4.31 Scanning Electron Microscope images of as-cast Alloy II. (a SEM images; b: EDS analysis of selected area)

After heat treatment, dissolved niobium and aluminum precipitates increases, as seen in Figure 4.32. Figure 4.32 shows the niobium precipitates. It can be seen that it has both globular and acicular structure.



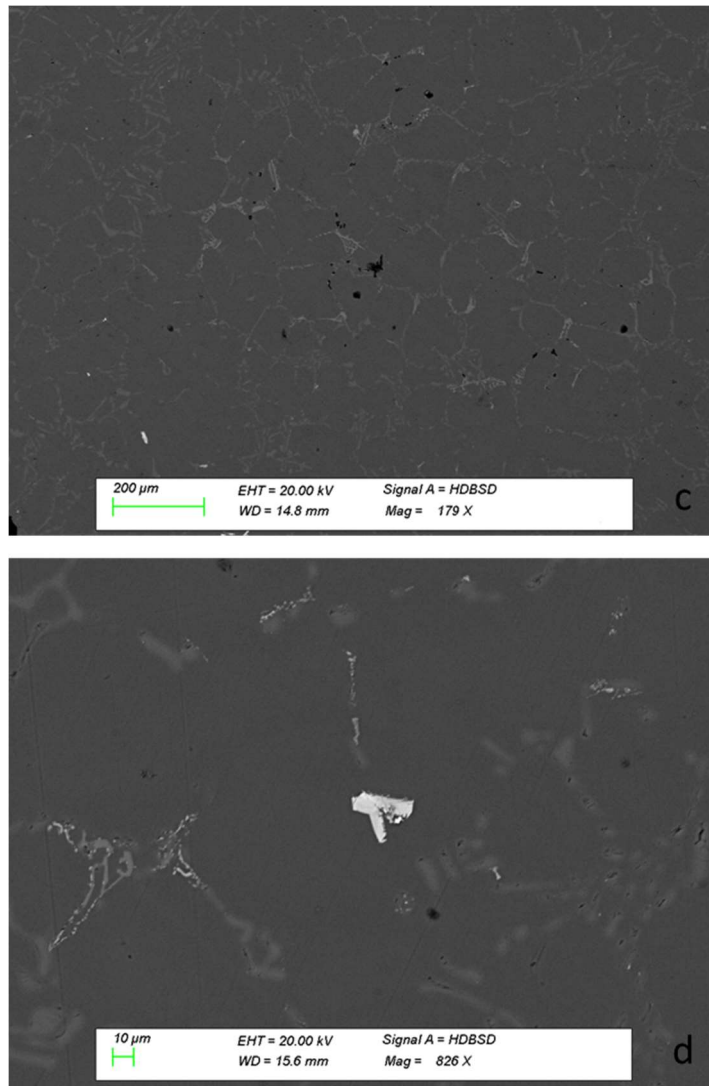


Figure 4.32 Scanning Electron Microscope images of heat-treated Alloy II in different magnifications. (a:214X magnifications; b: 88X magnification; c:179X magnification; d:826X magnification)

According to the optical and electron microscope examinations, it can be stated that eutectics which are formed at the grain boundaries are examined in detail. Alloy I and Alloy IV exhibit more acicular and lamellar eutectic structure. Alloy III has also fibrous eutectic structures together with transitional lamellar structure. When Alloy II is examined, most of the precipitated eutectics in as-cast condition is fibrous structure. Solutioning provides the eutectic modification. For all alloys, eutectic modification is seen after heat treatment. In addition, the results can be supported

with thermal analysis. Cooling curves indicate the Alloy II has the minimum eutectic nucleation temperature and maximum undercooling amount among 4 alloy type, they are summarized in Table 4.6.

Before continuing with grain size measurement, Figure 4.33 shows the SEM images of master alloy. It is clearly seen that white particles belongs to Al_3Nb precipitates as supported with XRD analysis.

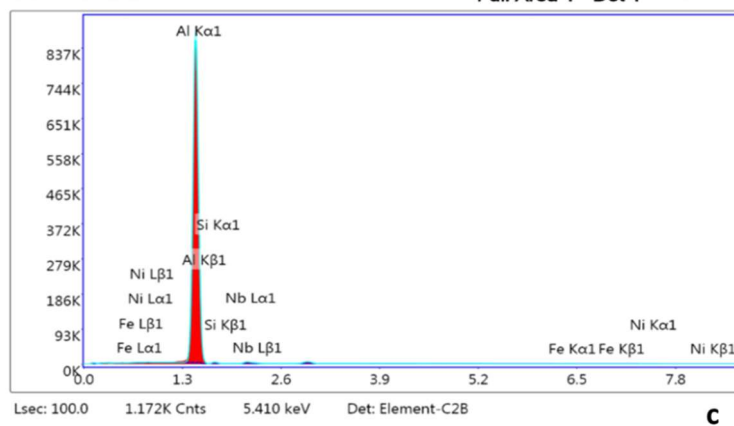
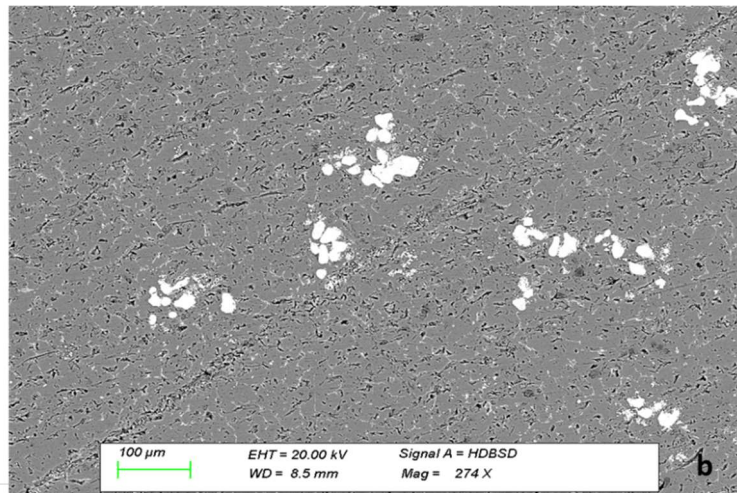
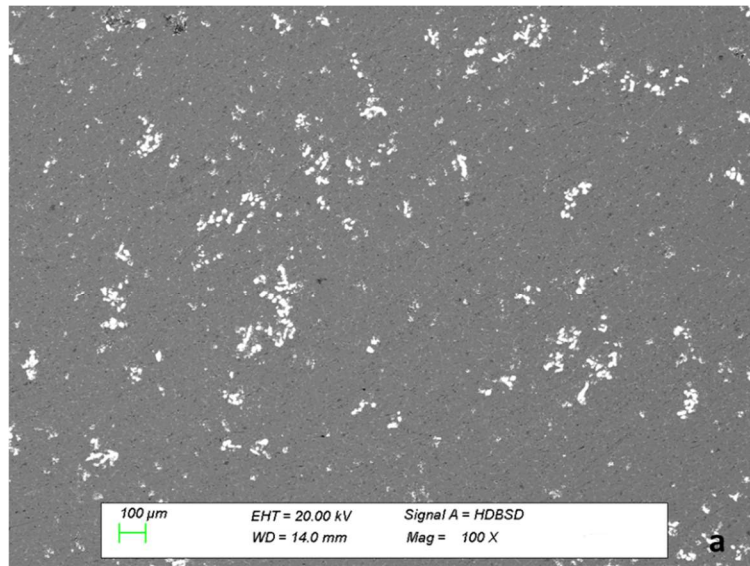


Figure 4.33 Scanning Electron Microscope images of master alloy. (a:100X magnification; b:374X magnification; c:EDS analysis results)

4.4.2 Grain Size Measurements

Optical microstructural examination indicates that dark gray like precipitates formed at the grain boundaries are the eutectic Al-Si precipitates. Grain size measurement was performed by considering the eutectic phases. Eutectic phase distributed areas are considered as grain boundaries, and they are measured as explained in section 3.8.2.

Both as-cast and as-heat treated specimens were prepared as explained in section 3.8.1 and grain size measurements were performed by using the device given in 3.8.2. Approximately 800 measurements were performed during grain size prediction. For each examination, at least 3 different locations were analyzed by taking at least 20 measurements for each location depending on the grain size.

Example of the grain size measurement is given in Figure 4.34.

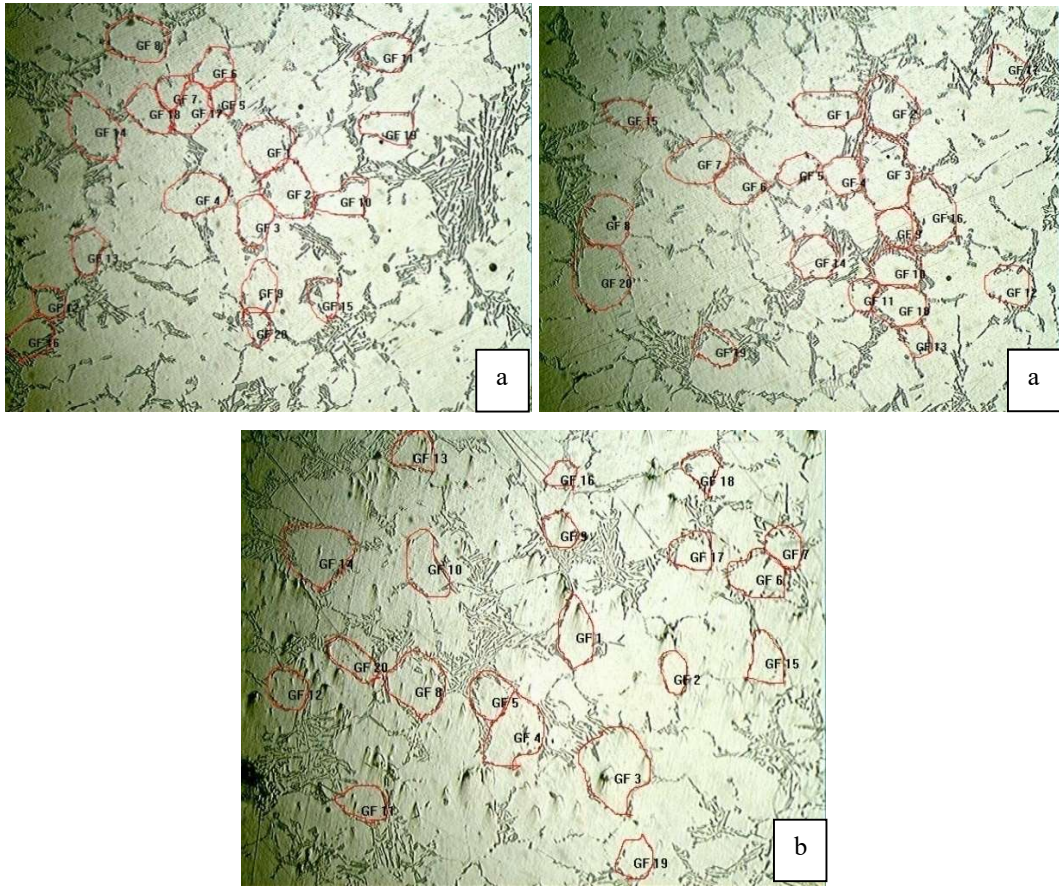


Figure 4.34 Example of grain size measurement, a: Alloy II, b: Alloy III

In addition, examination was performed from the two positions of the as-cast structure, including risering and gating, extracted from the mold shown in Figure 3.2. First one is prepared from the location shown in Figure 3.17 – c. The second one is taken from the riser shown in Figure 3.8. Grain size measurement results are given in Figure 4.35. When the results are compared, it is clearly seen that all grain refiners (Al8B, Al5TiB and Master alloy) decrease the grain size when they are compared with reference A357.0 alloy.

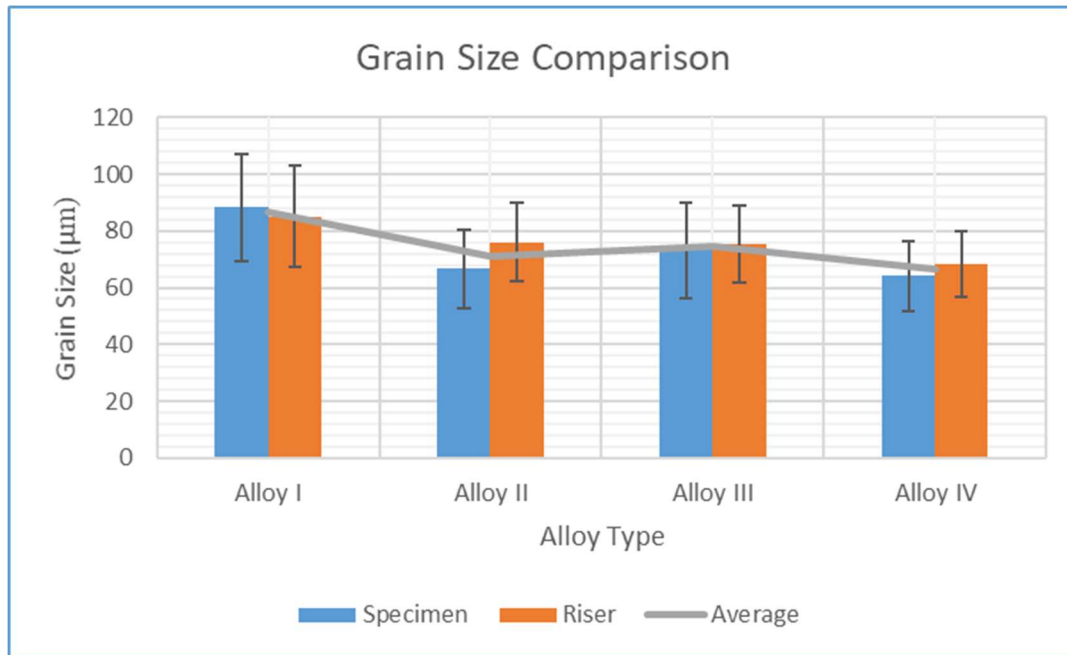


Figure 4.35 Comparison of grain size of Alloy I, II, III and IV

Since A357 alloy includes alloying elements, constitutional undercooling provides the reduction in grain size. Therefore, A357 alloy has already approximately 90 microns in grain. Moreover, the grain size is decreased to 60-micron levels when grain refiners are added. As it can be seen that standard deviation is very high for all alloys. It is probably resulted from the lower cooling rate. Microstructural images for each alloy are given in Appendix B.

In addition, grain size measurement was also performed for the specimens shown in Figure 4.27 in order to represent the relation between cooling curve rate and grain size. Their results are presented in Figure 4.36. It is seen that as the cooling rate increase grain size decreases as expected. The average grain size values for 9 mm thickness is early 60 microns while it is increased up to 90 microns when the cooling rate is decreased. Apart from the SOIF XJP-6A program, grain size measurements are also performed in Huvitz machine. Some examples of measurements are given in Appendix C.

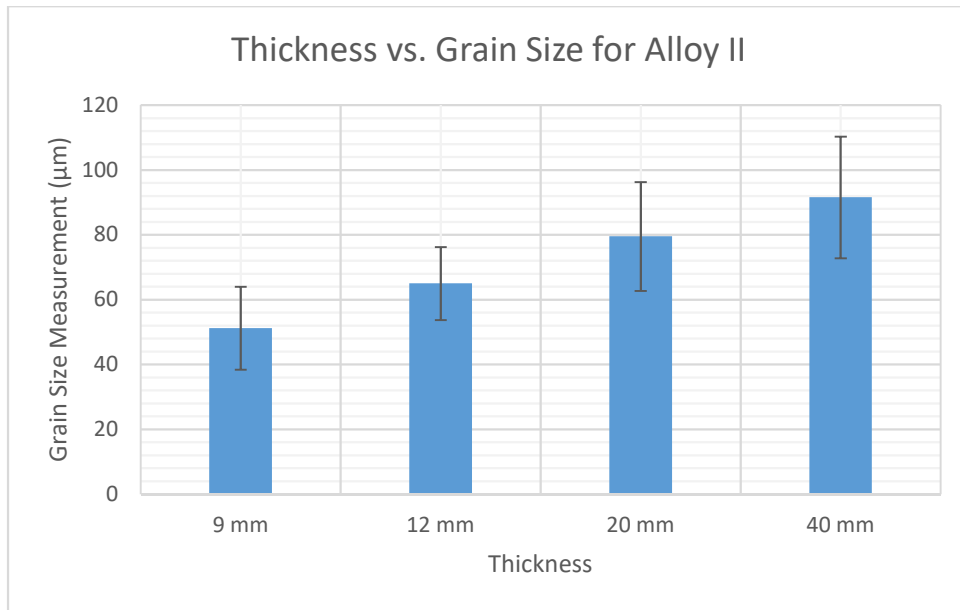


Figure 4.36 Comparison of grain sizes measured in different cross sections of Alloy II

4.5 Radiographic Examination Results

Radiographic examination results show that some of the high dense foreign materials are present in the structure. Porosity, shrinkage and other type of casting defects are not seen in the examination results. Figure 4.37 and Figure 4.38 show the examination results.

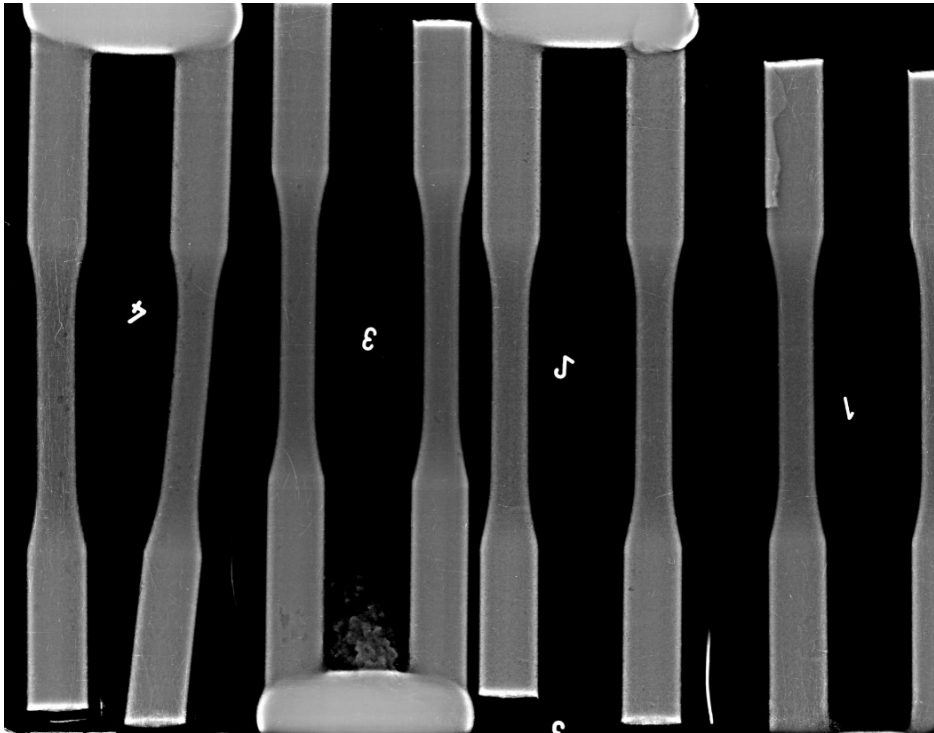


Figure 4.37 Radiographic examination results of Alloy I,II,III, and IV

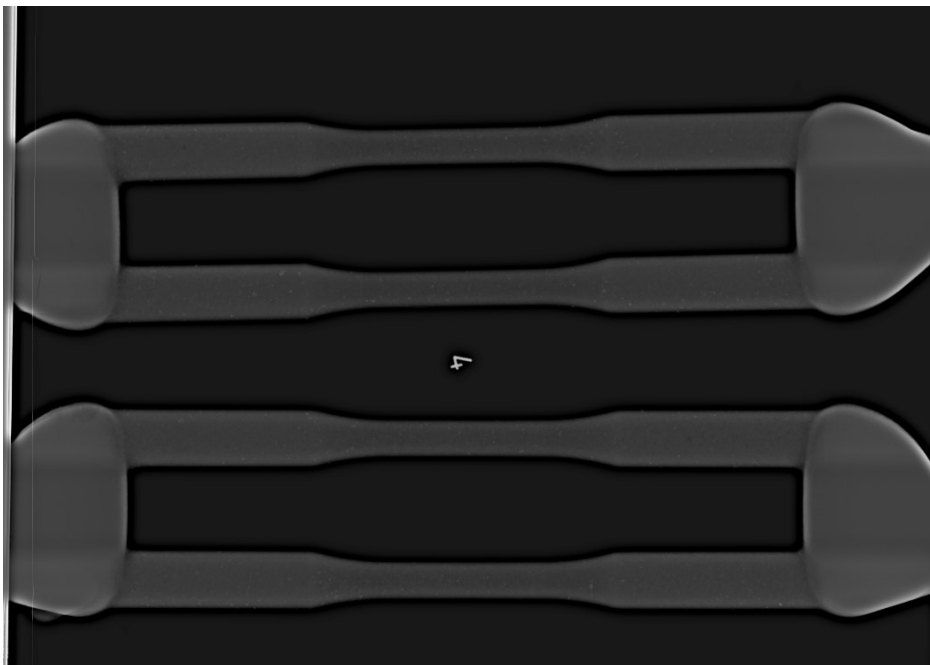


Figure 4.38 Radiographic examination results of Alloy II

4.6 Mechanical Test Results

Tensile test specimens cast into resin bonded sand mould which is shown in Figure 3.2 were tested as given in 3.10. Before tensile testing, x-ray inspection resulted that specimens do not show any defect which may alter the tensile test results. However, some shown white particles may be the indications of foreign materials.

Table 4.7 shows the average tensile test results together with their standard deviations. According to the results, it is clearly show that Alloy II exhibits larger standard deviation in percent elongation value having $\% 5.72 \pm 2.8$. The reason may be explained;

- Heterogenous grain size and eutectic structure distribution.
- Heterogeneous distribution of acicular type Al_3Nb particles revealed from scanning electron microscope results.

Maximum 8 % elongation value was seen for Alloy II. Especially, it is very high values when it is compared with % elongation given in MMPDS [29]. MMPDS defines the percent elongation for A357 alloy as 5 %, when it is defined in the critical surfaces of the part. This value can only be achieved with chilling effect. However, it is seen that Alloy II exhibit the same amount of % elongation under slow cooling.

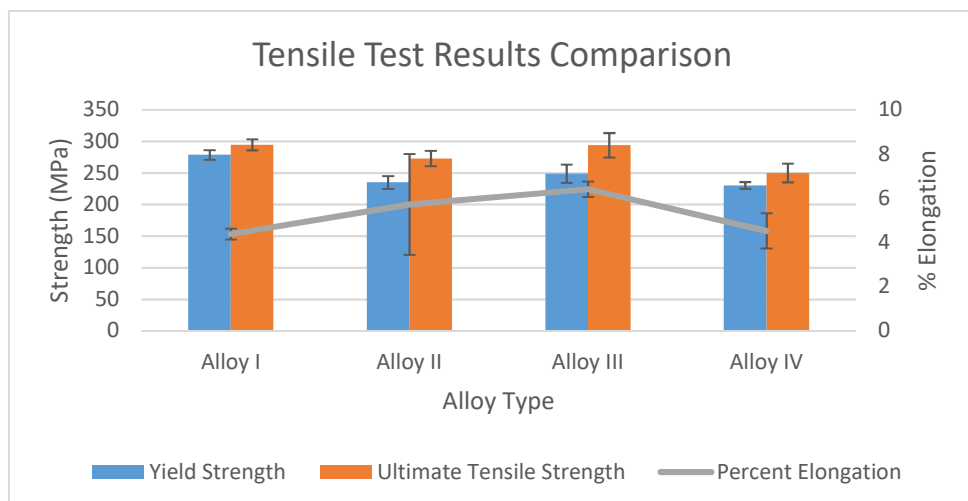


Figure 4.39 Tensile test results comparison for Alloy I, II, III and IV

When remaining alloys are compared, it is seen that the lowest percent elongation belongs to the Alloy I, un-refined A357 alloy. It is expected since microstructural examination indicates transitional lamellar structure together with lamellar structure in the heat-treated condition.

When yield strength values are examined, Table 4.7 reveals that Alloy I have the highest value. Yield strength depends on grain size, shown in Figure 2.6. Figure 4.40 shows the comparison in between yield strength and grain size for all experimentally cast alloys. When grain sizes are tabulated together with yield strength values, it is seen that largest grains belongs to Alloy I. That's why, no correlation can be made by considering hall patch equation. However, possible causes of this confliction can be explained as follows;

Alloy I was prepared with the only melting and casting of raw materials. Chemical ingredient inside the raw material play an important role for yield strength determination due to dislocation movement diminishing. That's why, intentionally added niobium, boron and titanium alloys, and difference in chemical composition of the raw materials may affect the yield strength detrimentally.

Another possible and most powerful idea behind this confliction is the number of testing. It can be seen in Table 4.7 that standard deviations are relatively large which may be caused due to the smaller number of testing activities.

Table 4.7 Tensile Test Results of Alloy I, II, III and IV

	Yield Strength (MPa)	Standard Deviation	Tensile Strength (MPa)	Standard Deviation	% Elongation	Standard Deviation
Alloy I	278	7.58	294	8.65	4.39	0.25
Alloy II	235	10.07	273	12.28	5.72	2.28
Alloy III	249	14.38	294	19.37	6.41	0.35
Alloy IV	230	5.34	250	14.75	4.53	0.80

When the standard deviations are considered, all four alloys may exhibit similar yield strength values if the number of experiments is increased and proper industrial scale alloying equipment is used. Since standard deviation on the average grain size values are already higher which is seen in Figure 4.40, yield strength values are also be expected to deviate.

Finally, when average tensile strength values are compared, Alloy I and Alloy III have similar results, 294 MPa. Then, Alloy II, which is intentionally developed by this thesis, has 273 MPa. Having smallest value is 250 MPa belonging to Alloy IV. Before continuing with discussion, tensile strength depends on;

- Defects inside the specimen,
- Improperly mixed charging materials,
- Acicular and lamellar fibrous like phases, i.e. Eutectic phase,
- Iron based eutectic phases.
- Grain size and secondary dendrite arm spacing

In the scope of this thesis, microstructural examinations were performed for eutectic modification observation. After yielding occurs during the testing, nodular, spheroidal structures provide to have higher elongation values. That's why, lower yield and tensile strength of Alloy IV can be caused due to lamellar eutectic structure.

Moreover, Alloy III has the largest tensile strength values when the standard deviation is taken into consideration. This can be stated due to;

- Smaller grain size,
- Transitional and fibrous eutectic structure,
- Homogeneously distributed TiB_2 and Al_3Ti .

Alloy I has similar yield strength values with Alloy III. Although Alloy III has smaller yield strength values, its % elongation is larger than Alloy I due to smaller grain size and more nodular eutectic structure.

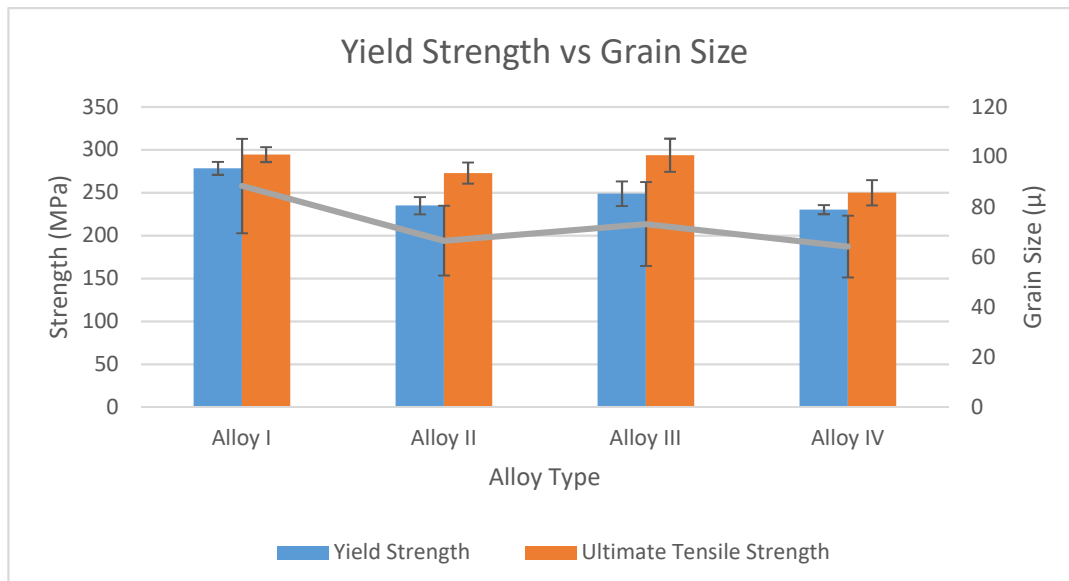


Figure 4.40 Comparison of yield strength and grain size for Alloy I, II, III and IV

When Alloy II is examined, it is seen that tensile strength of the specimens are very dependent to percent elongation. When percent elongation is increased, tensile strength values decreases. Figure 4.41 shows the comparison among the tensile test

specimens. As stated previously, percent elongation changes very rapidly. It is probably caused by the Al_3Nb phases formed in acicular morphology.

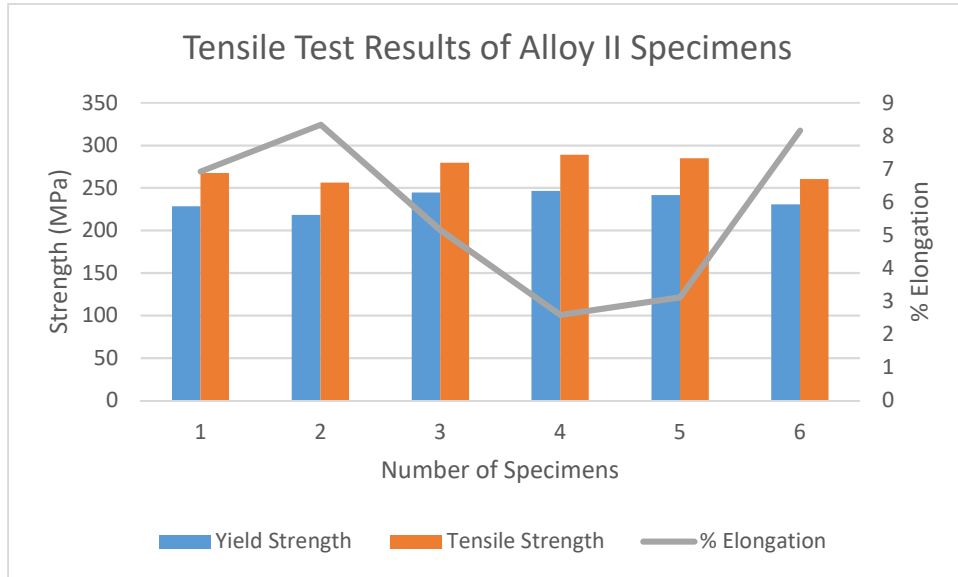


Figure 4.41 Comparison of tensile test values of Alloy II specimens

To summarize, all the major findings are listed below;

- $Al_{2.79}Nb_{0.3B}$ addition to the A357 alloy provides eutectic modification during even slow cooling rates.
- $Al_{2.79}Nb_{0.3B}$ addition to the A357 alloy results the decrement in grain size.
- Heterogeneous distribution of niobium due to its higher density caused differences in the examination results.
- $Al_{2.79}Nb_{0.3B}$ addition provides to increase percent elongation due to eutectic modification.

CHAPTER 5

CONCLUSION AND FUTURE WORKS

Development of Al-Nb-B master alloy was performed by charging Al₄Nb, Al₈B and pure aluminum alloy. According to the literature review, targeting composition was decided as Al_{2.79}Nb_{0.3}B.

Chemical analysis results revealed that niobium exhibits heterogeneity. Both ICP and XRF results reveal the difference in weight percentages. Average of the results were based for the alloying calculations. XRD results verified the reaction of Al₃Nb and NbB₂ in the master alloy.

Alloy I, II, III and IV were cast into resin bonded sand mould to simulate the slow cooling, which represent the complex parts designed and manufactured for the aerospace applications. Both thermal analysis and microstructural examinations of Al_{2.79}Nb_{0.3}B alloy yielded eutectic modification. Eutectic temperature was observed to be depressed while the undercooling amount was increased. Moreover, transitional lamellar and fibrous eutectic phases were the evidence of eutectic modification according to the microstructural examination. Grain size of A357 alloy was decreased by addition of Al_{2.79}Nb_{0.3}B alloy. Liquidus nucleation temperatures were also increased for Alloy II and III. Both Alloy II, III and IV decreased the grain size to the 65 μm levels in average

Radiographic examination resulted that there is no casting defect inside the specimens.

Finally, tensile test results clearly verified that A357 alloy refined with niobium based alloy (Alloy II) exhibits higher percent elongation. Although the grain size reduction was achieved by Al_{2.79}Nb_{0.3}B alloy developed in this thesis, its effect on

yield and tensile strength is not sufficiently higher than pure alloy due to some acicular shape intermetallic still exist in the structure even after T6 heat treatment.

In the scope of this thesis, future works could be stated as follows;

1. Evaluation of microstructure adding Al_{2.79}Nb_{0.3}B to the A357 alloy with different cooling rates
2. Development of more effective master alloys including different niobium and boron contents by considering XRD analysis.
3. Development of the lab scale alloying process to enhance homogeneity.
4. Replacing of the charge materials by pure niobium and KBF₄ salt for exothermic reaction.
5. Comparison of strontium added and niobium-based master alloy added A357 alloys in terms of eutectic modification.
6. Tensile test allowable activities by considering huge number of testing specimens with verified niobium-boron based master alloy.

REFERENCES

- [1] Campbell, F.C. (Ed.), 2012. Introduction and Uses of Lightweight Materials, in: *Lightweight Materials: Understanding the Basics*. ASM International, pp. 1–10.
- [2] Aluminum and Aluminum Alloys, in *Metals Handbook Desk Edition*, 2nd ed., J.R. Davis, Ed., ASM International, 1998, p 417–505.
- [3] Davis, F., & Eyre, T. (1994). The effect of silicon content and morphology on the wear of aluminium-silicon alloys under dry and lubricated sliding conditions. *Tribology International*, 27(3), 171-181. doi:10.1016/0301-679x(94)90042-6
- [4] Ibrahim, M., Elgallad, E., Valtierra, S., Doty, H., & Samuel, F. (2016). Metallurgical Parameters Controlling the Eutectic Silicon Characteristics in Be-Treated Al-Si-Mg Alloys. *Materials*, 9(2), 78. doi:10.3390/ma9020078
- [5] Asmael, Mohammed, 2009, Lost foam casting of LM6-Al-Si cast alloy. Universiti Teknologi Malaysia
- [6] Lloyd, Samuel J., 2016, Effects of a Niobium-Boron Grain Refiner on Undercooling and Microstructural Evolution of Aluminium Silicon Alloys. Brunel University.
- [7] Taylor, John, A., 2004, The effect of iron in Al-Si casting alloys, The University of Queensland.
- [8] Yalınız, Emrah. 2018, Development of high temperature creep resistant aluminium based sand cast magnesium alloys, Middle East Technical, University.
- [9] Kashyap, K. T., & Chandrashekar, T. (2001). Effects and mechanisms of grain refinement in aluminium alloys. *Bulletin of Materials Science*, 24(4), 345-353. doi:10.1007/bf02708630.

- [10] Poyraz, Cemre Metin. 2019, Effect of mechanical vibration on the microstructure and the mechanical properties of 7075 aluminum alloy produced by semi-solid melting method
- [11] How XRF WORKS. (n.d.). Retrieved February 07, 2021, from <https://www.bruker.com/content/bruker/int/en/products-and-solutions/elemental-analyzers/handheld-xrf-spectrometers/how-xrf-works.html>
- [12] XU, J., Li, Y., Hu, B., Jiang, Y., & Li, Q. (2019). Development of Al–Nb–B master alloy with high Nb/B ratio for grain refinement of hypoeutectic Al–Si cast alloys. *Journal of Material Science*. doi: 10.1007/s10853-019-03915-9
- [13] ASTM, “ASTM B557 – 15 Standard Test Methods for Tension Testing Wrought and Cast Aluminum- and,” *Astm Int.*, vol. i, pp. 1–16, 2015.
- [14] Xu, C., Wang, C. Y., Yang, H. J., Liu, Z. G., Yamagata, H., & Ma, C. L. (2016). Solidification Behavior and Mechanical Properties of Al-Si-Mg Alloy with Ti Addition. *Materials Science Forum*, 850, 594–602. doi:10.4028/www.scientific.net/msf.850.594
- [15] Bolzoni, L., & Hari Babu, N. (2016). Engineering the heterogeneous nuclei in Al-Si alloys for solidification control. *Applied Materials Today*. Doi:10.1016/j.apmt.2016.11.001
- [16] EASTON, M., & StJOHN, D. (2005). An Analysis of the Relationship between Grain Size, Solute Content, and the Potency and Number Density of Nucleant Particles. *METALLURGICAL AND MATERIALS TRANSACTIONS*.
- [17] Y Birol (2012) Performance of AlTi5B1, AlTi3B3 and AlB3 master alloys in refining grain structure of aluminium foundry alloys, *Materials Science and Technology*, 28:4,481-486, DOI: 10.1179/1743284711Y.0000000058
- [18] BOLZONI, L., & HARI BABU, N. (2019). Efficacy of Borides in Grain Refining Al-Si Alloys. *METALLURGICAL AND MATERIALS TRANSACTIONS A*, 50A, 746-756. Doi:10.1007/s11661-018-5017-1
- [19] Bolzoni, L., Nowak, M., & Hari Babu, N. (2015). On the effect of Nb-based compounds on the microstructure of Al₁₂Si alloy. *Materials Chemistry and Physics*. Doi:10.1016/j.matchemphys.2015.05.076

- [20] Bolzoni, L., Nowak, M., & Hari Babu, N. (2014). Grain refinement of Al–Si alloys by Nb–B inoculation. Part I: Concept development and effect on binary alloys. *Materials and Design*. Doi:10.1016/j.matdes.2014.08.066
- [21] Bolzoni, L., Nowak, M., & Hari Babu, N. (2014). Grain refinement of Al–Si alloys by Nb–B inoculation. Part II: Application to commercial alloys. *Materials and Design*. Doi:10.1016/j.matdes.2014.08.067
- [22] Bolzoni, L., & Hari Babu, N. (2015). Refinement of the grain size of the LM25 alloy (A356) by 96Al–2Nb–2B master alloy. *Journal of Materials Processing Technology*. doi:10.1016/j.jmatprotec.2015.03.011
- [23] Nowak, M. (2011). Development of Niobium-Boron grain refiner for aluminium silicon alloys. Uxbridge: Brunel University.
- [24] Sigworth, G. K. (2008). THE MODIFICATION OF Al-SI CASTING ALLOYS: IMPORTANT PRACTICAL AND THEORETICAL ASPECTS. *International Journal of Metalcasting*.
- [25] CHEN, R., SHI, Y., XU, Q., & LIU, B. (2013). Effect of cooling rate on solidification parameters and microstructure of Al–7Si–0.3Mg–0.15Fe alloy. *Transactions of Non Ferrous Metals Society of China*. doi:10.1016/S1003-6326(14)63236-2
- [26] Il'yashenko, M. (n.d.). Vr-17ms. Retrieved February 08, 2021, from <http://www.motorsich.com/eng/products/rodyktori/vr-17ms/>
- [27] AW169. (n.d.). Retrieved February 08, 2021, from <https://www.leonardocompany.com/en/products/aw-169>
- [28] Barrirero, J. (2019). Eutectic modification of Al-Si casting alloys (Unpublished master's thesis). LINKOPING UNIVERSITY.
- [29] SAE International, Metallic Materials Properties Development Standardization (MMPDS-08), Battelle Material Institute, 2013.

APPENDICES

A. Cooling Curves and First and Second Derivatives

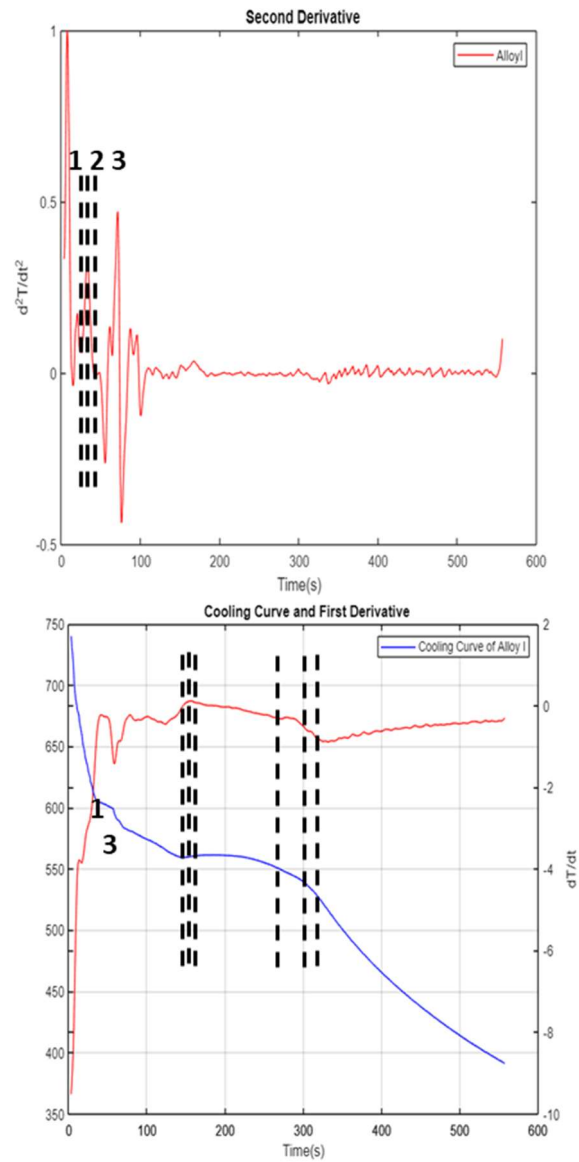


Fig.A. 1 Cooling Curve together with first and second derivatives of Alloy I

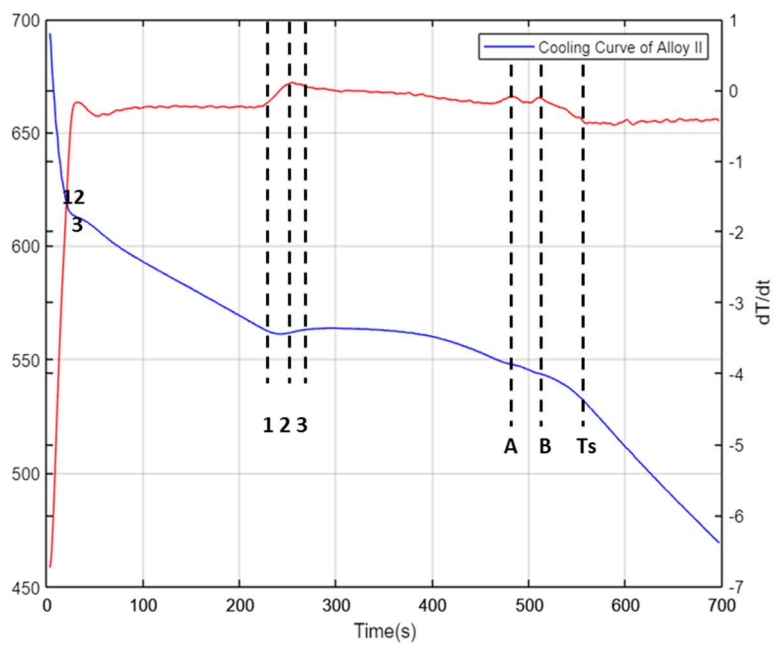
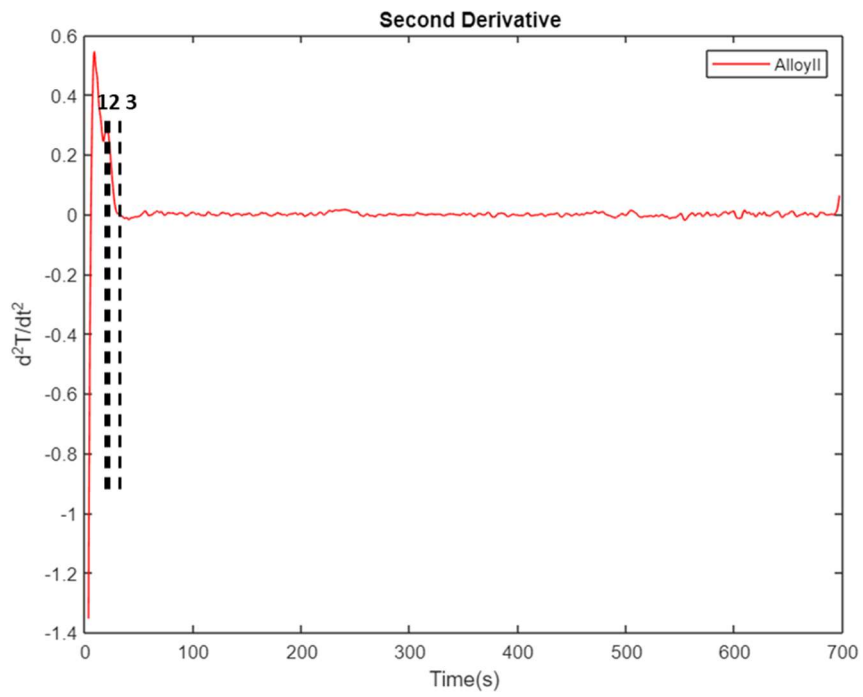


Fig.A. 2 Cooling Curve together with first and second derivatives of Alloy II

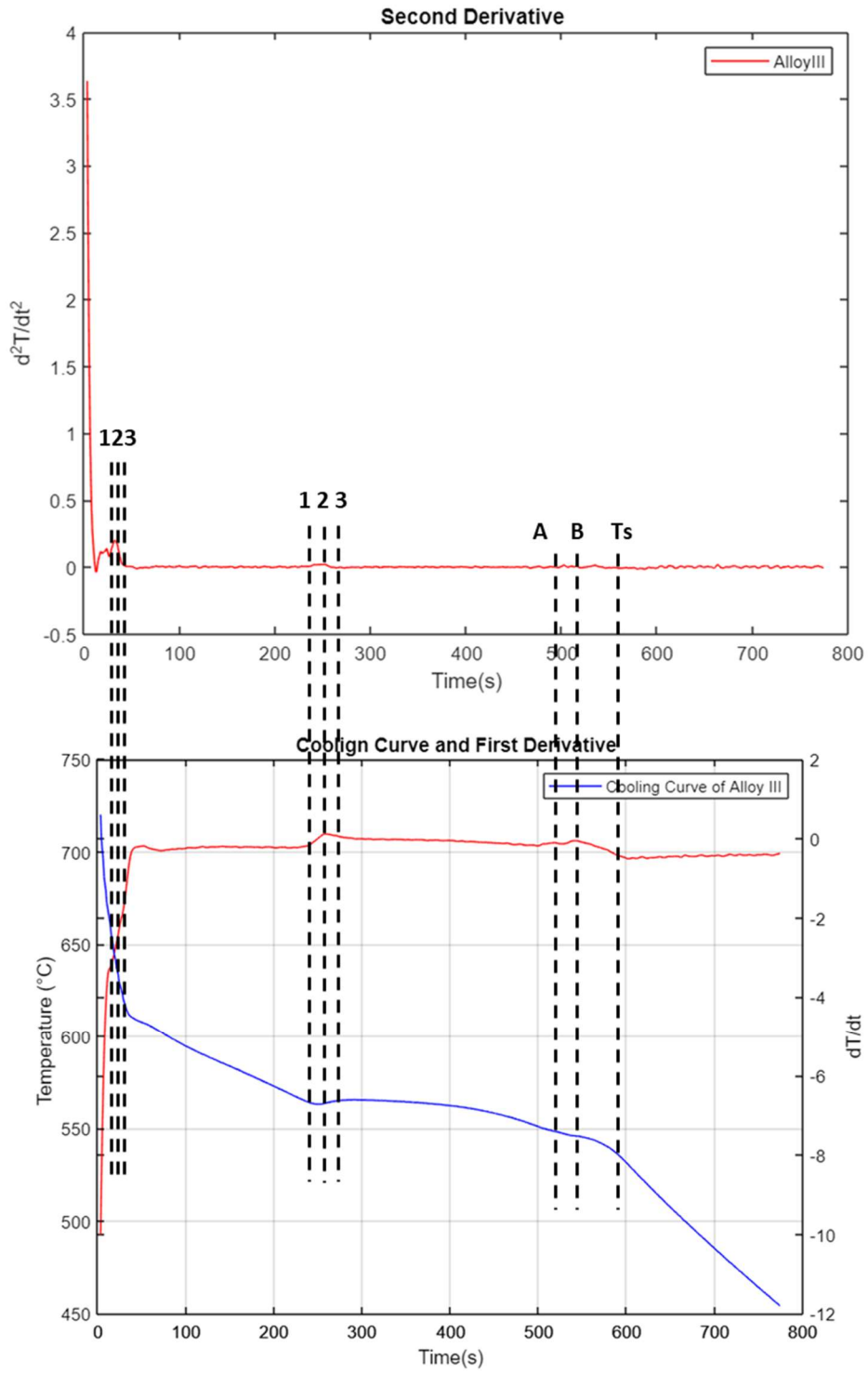


Fig.A. 3 Cooling Curve together with first and second derivatives of Alloy III

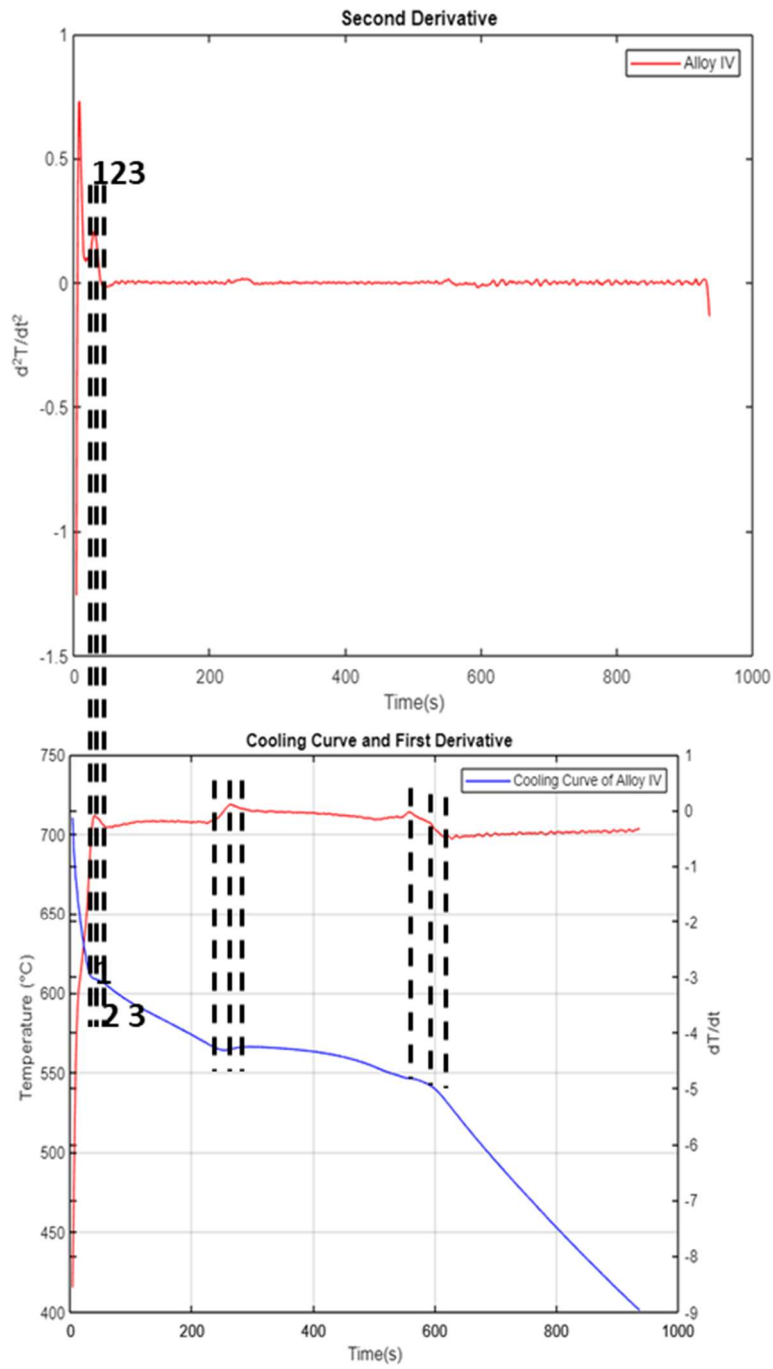


Fig.A. 4 Cooling Curve together with first and second derivatives of Alloy IV

B. Optical Microscope Images

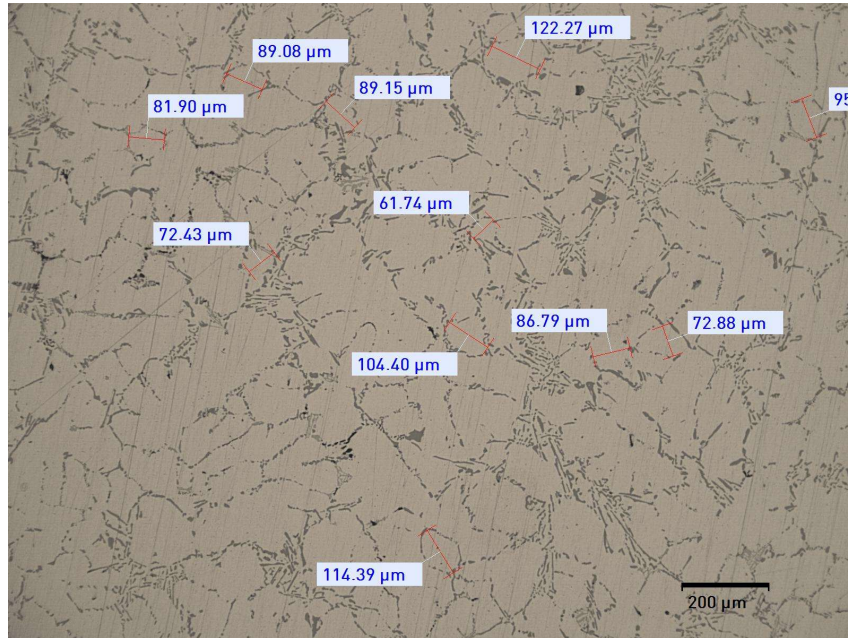


Fig. B. 1 200X magnification of heat-treated Alloy II.

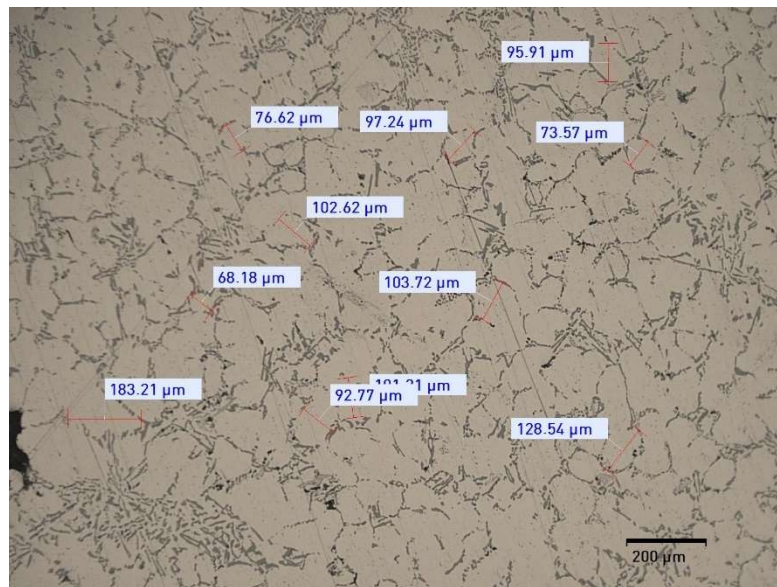


Fig. B. 2 200X magnification of heat-treated Alloy III.

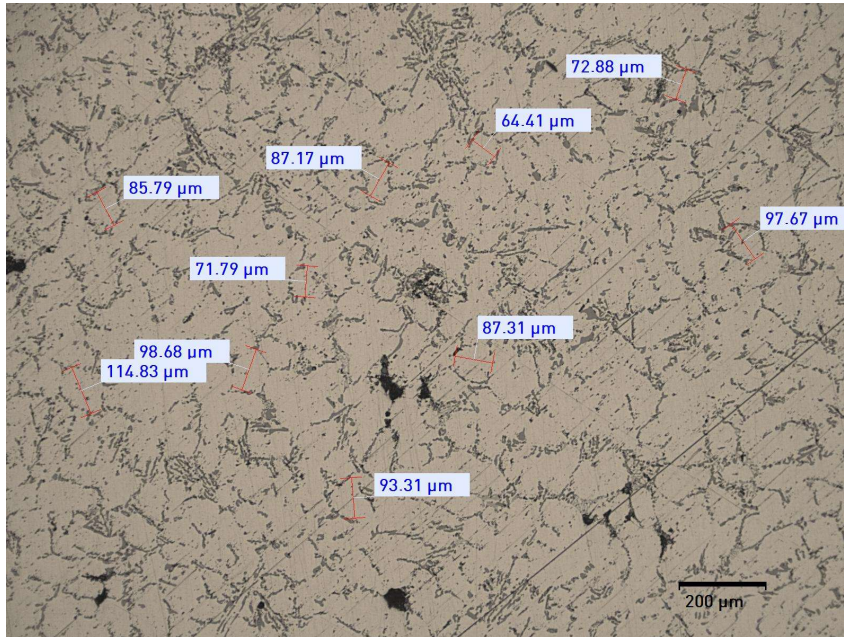


Fig. B. 3 200X magnification of heat-treated Alloy IV.

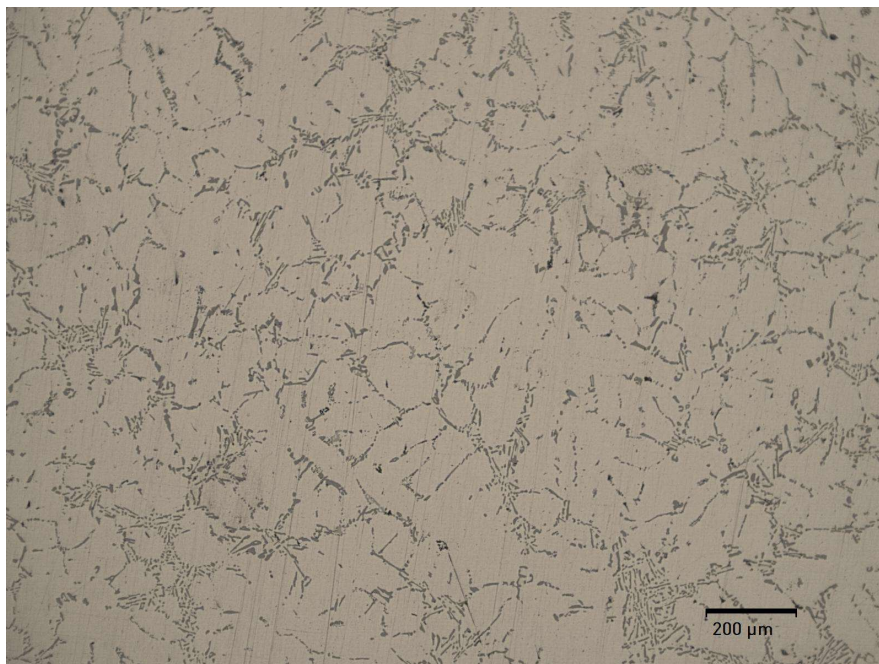


Fig. B. 4 200X magnification of heat – treated Alloy II

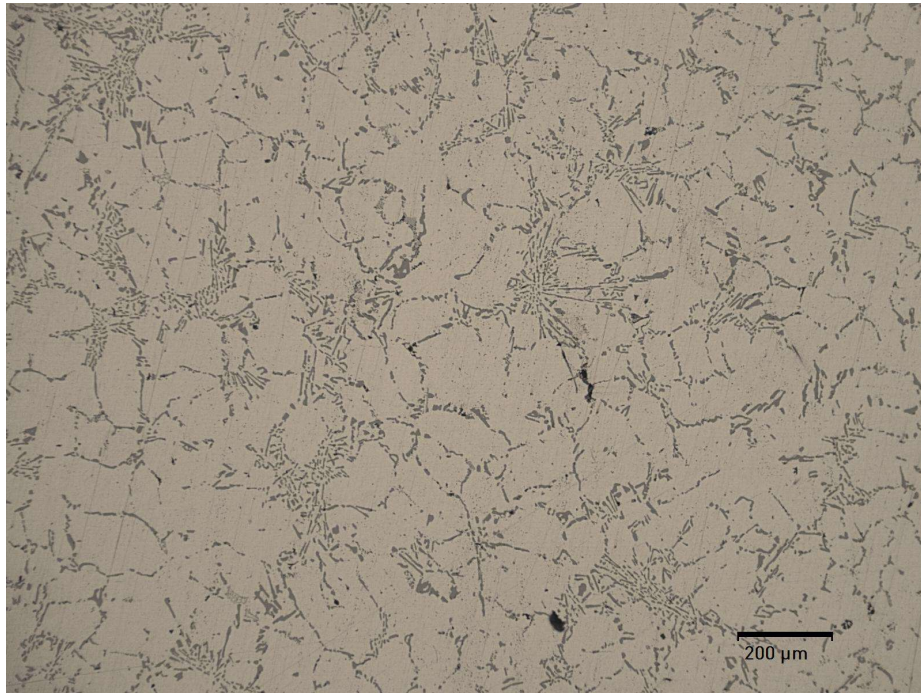


Fig. B. 5 200X magnification of heat – treated Alloy II

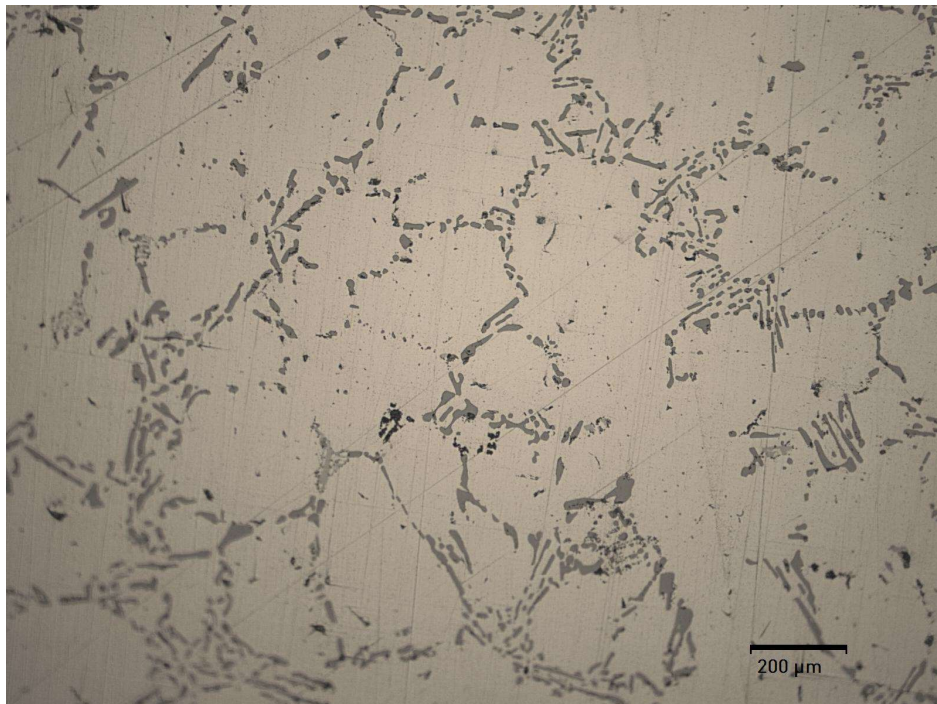


Fig. B. 6 500X magnification of heat – treated Alloy II

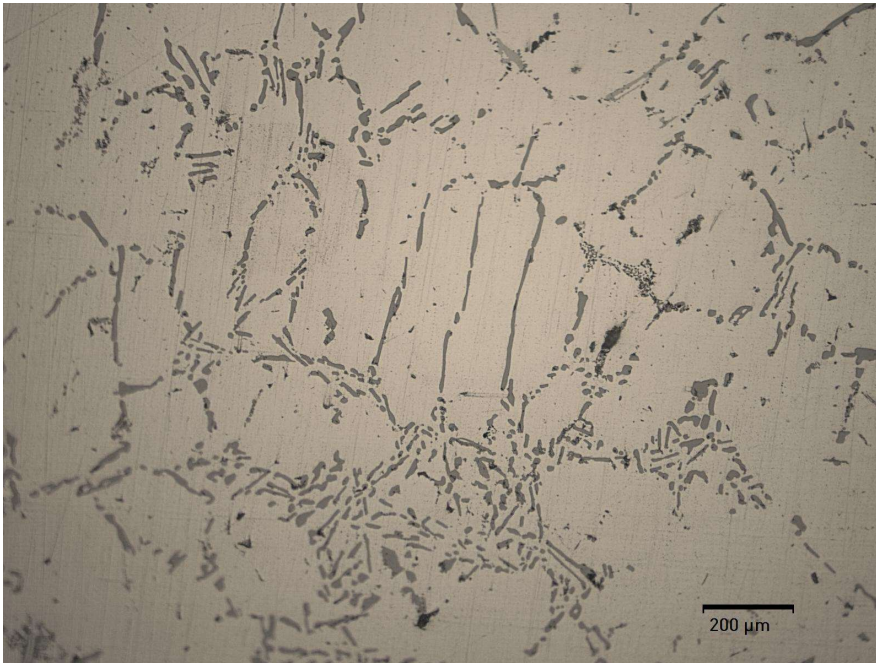


Fig. B. 7 500X magnification of heat – treated Alloy II

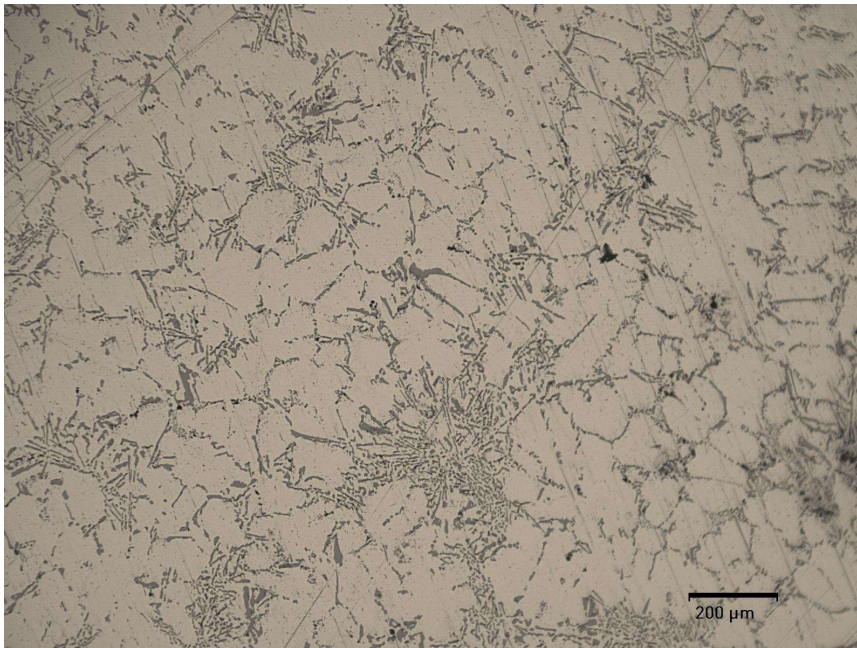


Fig. B. 8 200X magnification of heat – treated Alloy III

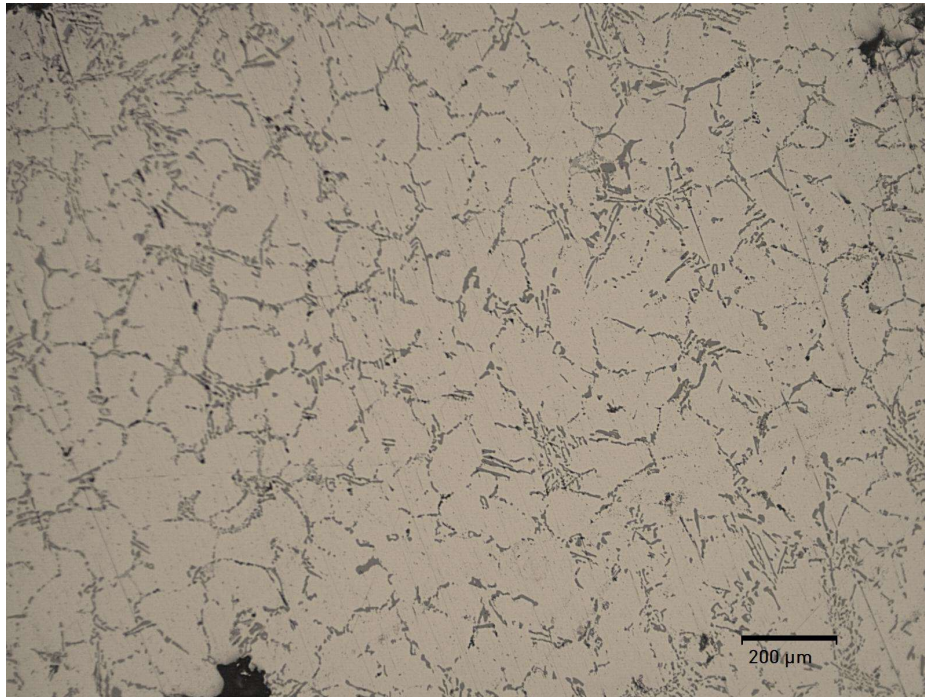


Fig. B. 9 200X magnification of heat – treated Alloy III

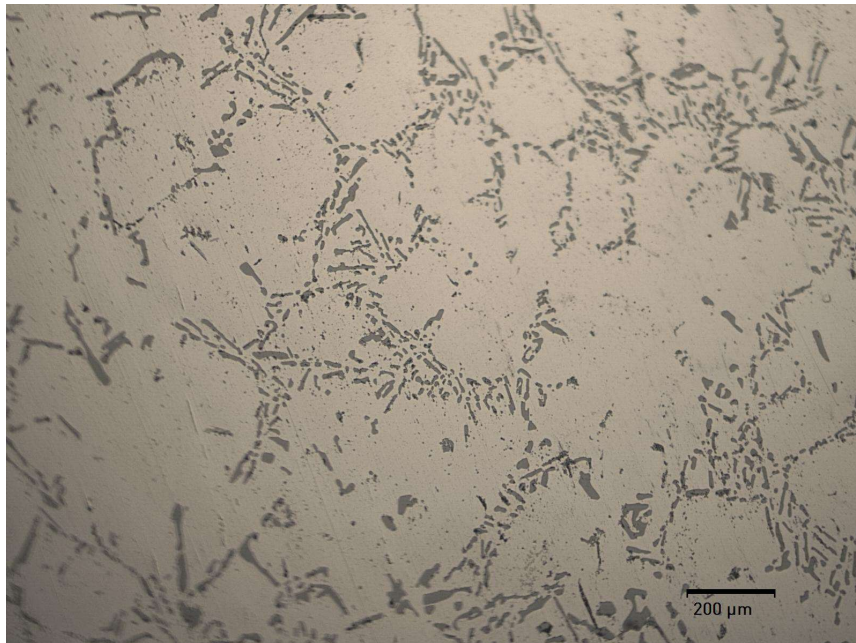


Fig. B. 10 500X magnification of heat – treated Alloy III

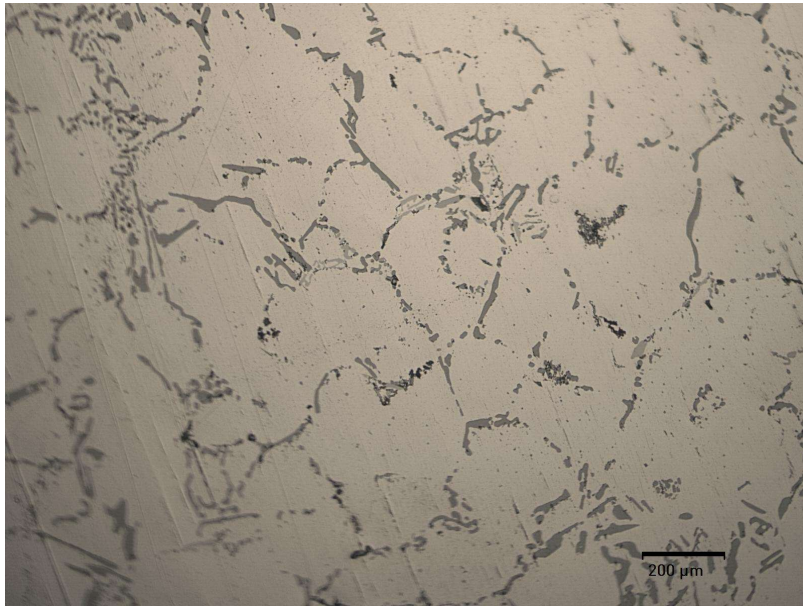


Fig. B. 11 500X magnification of heat – treated Alloy III

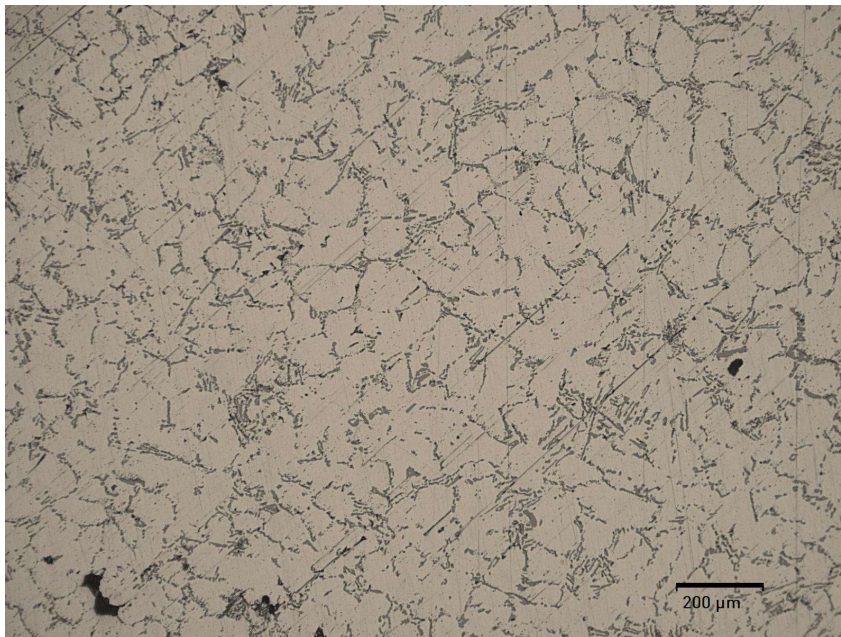


Fig. B. 12 200X magnification of heat – treated Alloy IV

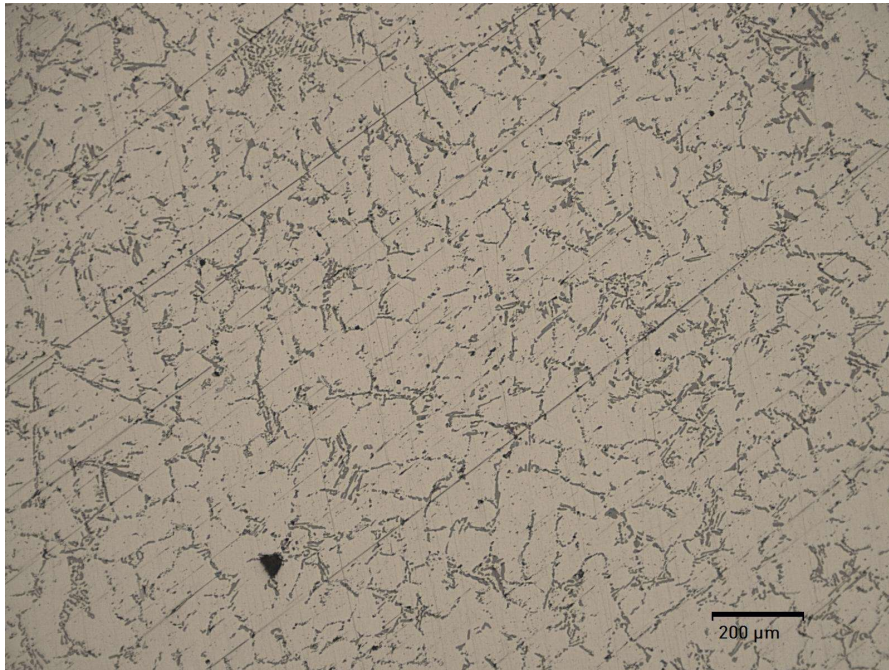


Fig. B. 13 200X magnification of heat – treated Alloy IV

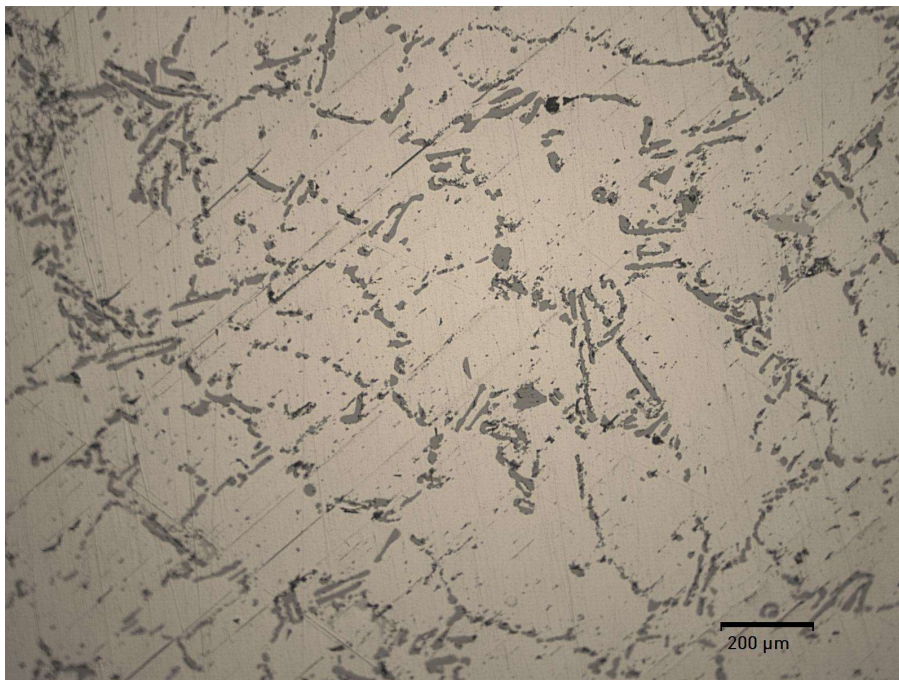


Fig. B. 14 500X magnification of heat – treated Alloy IV

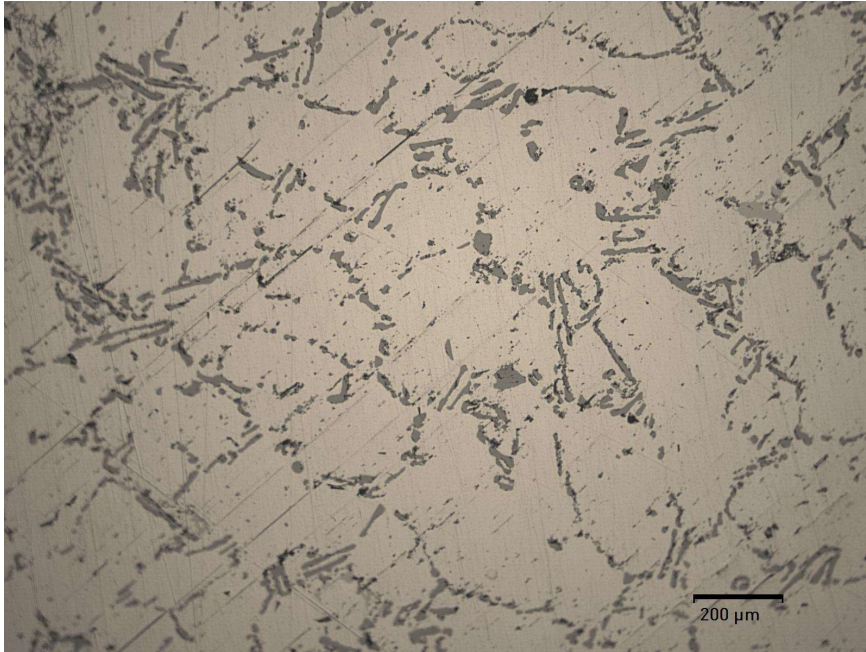


Fig. B. 15 500X magnification of heat – treated Alloy IV

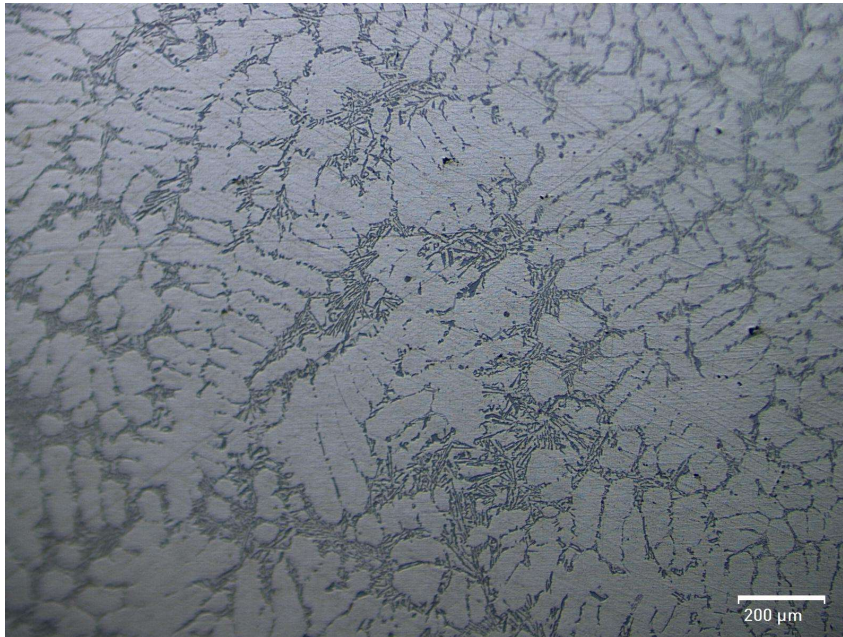


Fig. B. 16 200X magnification of heat – treated Alloy I

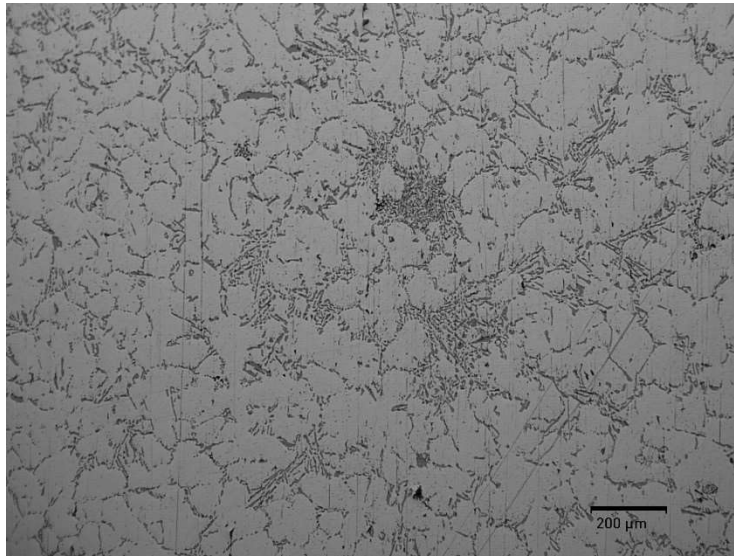


Fig. B. 17 200X magnification of heat – treated Alloy I

C. Grain Size Measurement Images

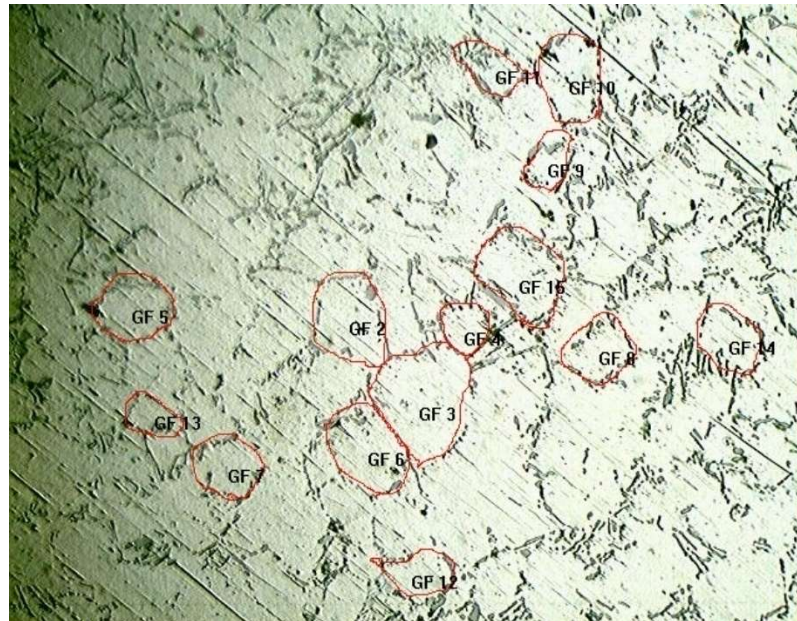


Fig. C. 1 Grain size measurement of heat-treated Alloy I

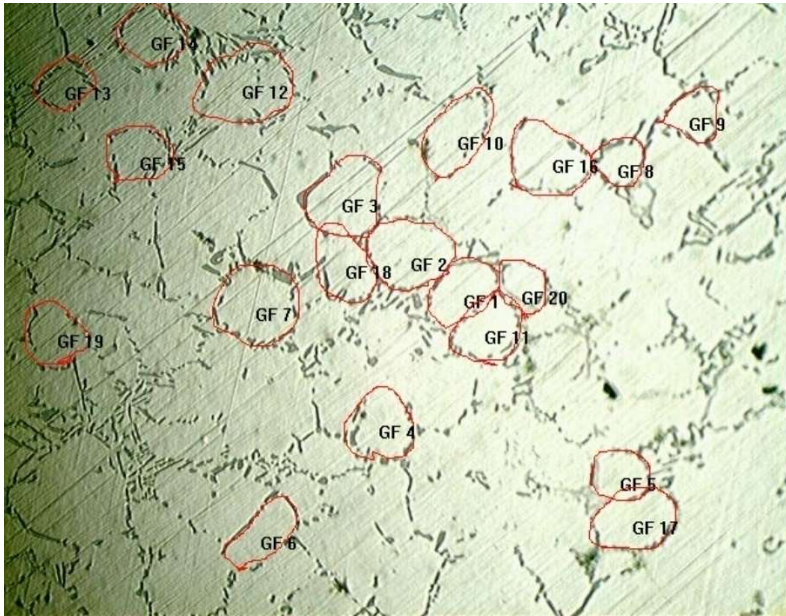


Fig. C. 2 Grain size measurement of heat-treated Alloy II

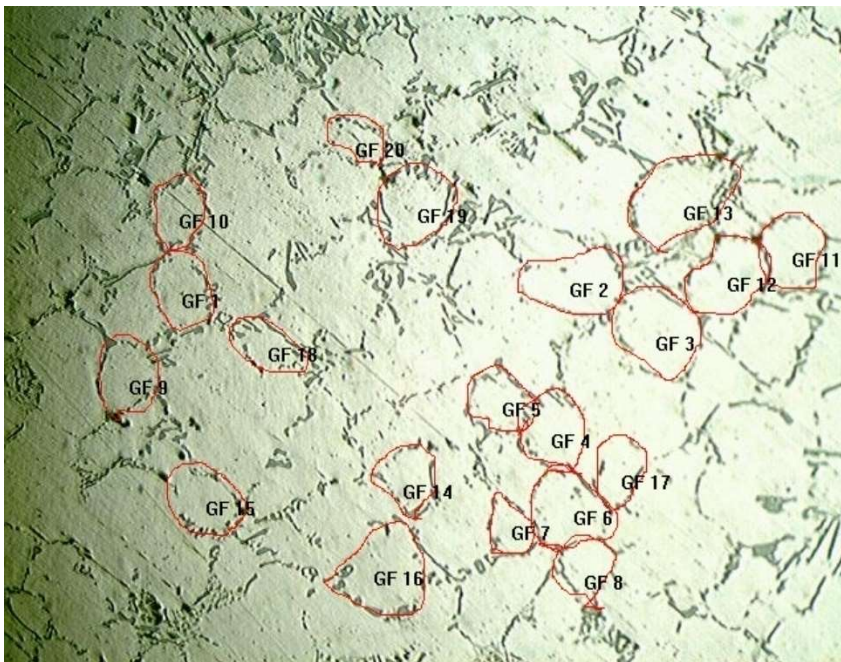


Fig. C. 3 Grain size measurement of heat-treated Alloy III

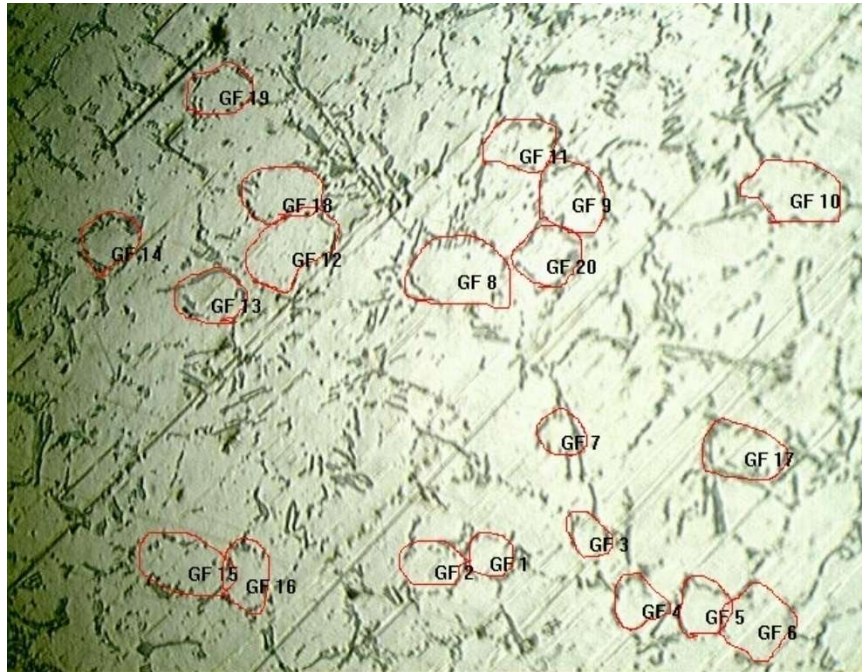


Fig. C. 4 Grain size measurement of heat-treated Alloy IV